Measurement of the muon spin precession frequency using the straw tracking detectors at the Fermilab Muon g-2 experiment

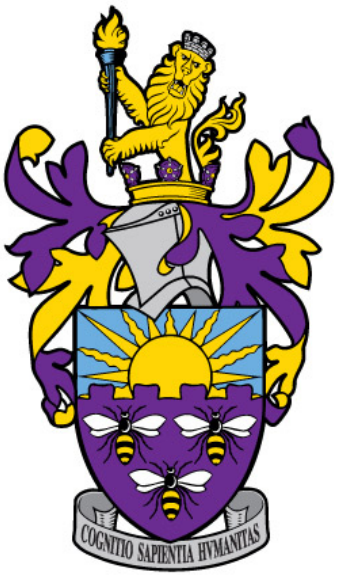

A thesis submitted to The University of Manchester for the degree of Doctor of Philosophy in the Faculty of Science and Engineering

George M Sweetmore

Department of Physics and Astronomy

2023

Contents

Abstract

The measurement of the anomalous magnetic dipole moment of the muon (a_μ) has long stood as an excellent precision test of the Standard Model (SM).

The Fermilab Muon g-2 experiment has recently finished data-taking and in July 2023 published its latest determination of a_μ with a world-leading precision of 0.2 ppm. In this publication, it surpassed the systematic uncertainty goal defined in the TDR. The analyses of a dataset approximately four times larger than this recent publication is now underway.

The principle measurement of the Muon g-2 experiment measures a_μ by taking the ratio of two frequencies; the anomalous precession frequency (ω_a) and the muon-weighted magnetic field of the experiment's storage ring measured from the precession frequency of protons in water using nuclear magnetic resonance (NMR) probes.

In all publications to date, ω_a has been determined using energy deposits in the 24 calorimeters. However, the Fermilab experiment has two straw tracker detectors measuring the time and momentum of charged particles which can in principle also be used to to measure ω_a and such a measurement can provide an invaluable cross-check of the calorimeter result with different, and reduced, systematic uncertainties.

This thesis presents the first (blinded) determination of ω_a using just charged tracks from the straw tracking detectors as opposed to calorimeter energy deposits. This analysis was undertaken using the Run-2/3 dataset which represents approximately 25% of the final dataset. A total uncertainty of 2.19 ppm on ω_a was obtained which is dominated by the statistical uncertainty of 2.16 ppm.

Additionally two new methodologies important to the analysis of the straw tracking data have been developed: one to better determine the track arrival time (t_0) and one to determine the level of pileup in the tracking detectors. The new t_0 algorithm which incorporates angular information improves the resolution on the determination of the t_0 by a factor of two and results in 19% more tracks being successfully reconstructed.

The data from the trackers is also used to determine the beam profile that weights the magnetic field in the determination of a_μ and in determining several of the systematic uncertainties in the calorimeter-based ω_a analysis. A detailed study of the impact of the internal alignment of the tracker, the t_0 and pileup on the determination of the beam position was undertaken and propagated through to an uncertainty in the ω_a determination. These uncertainties were used in the Fermilab Muon g-2 experiment's recent publication in Phys. Rev. Lett.

Declaration

No portion of the work referred to in this thesis has been submitted in support of an application for another degree or qualification of this or any other university or other institute of learning.

George M Sweetmore

Copyright

i The author of this thesis (including any appendices and/or schedules to this thesis) owns certain copyright or related rights in it (the "Copyright") and they have given the University of Manchester certain rights to use such Copyright, including for administrative purposes.

ii Copies of this thesis, either in full or in extracts and whether in hard or electronic copy, may be made only in accordance with the Copyright, Designs and Patents Act 1988 (as amended) and regulations issued under it or, where appropriate, in accordance with licensing agreements which the University has from time to time. This page must form part of any such copies made.

iii The ownership of certain Copyright, patents, designs, trademarks and other intellectual property (the Intellectual Property) and any reproductions of copyright works in the thesis, for example graphs and tables (Reproductions), which may be described in this thesis, may not be owned by the author and may be owned by third parties. Such Intellectual Property and Reproductions cannot and must not be made available for use without the prior written permission of the owner(s) of the relevant Intellectual Property and/or Reproductions.

iv Further information on the conditions under which disclosure, publication and commercialisation of this thesis, the Copyright and any Intellectual Property and/or Reproductions described in it may take place is available in the University IP Policy (see `http://documents.manchester.ac.uk/ DocuInfo.aspx?DocID=24420`), in any relevant Thesis restriction declarations deposited in the University Library, the University Librarys regulations (see `http://www.library.manchester.ac.uk/about/regulations/`) and in the Universitys policy on Presentation of Theses.

Acknowledgements

I would like to thank my supervisor, Mark Lancaster, for his immeasurable support throughout my PhD. I would like to thank Alex Keshavarzi, Joe Price and James Mott for their support and help throughout my time working on the Muon g-2 experiment.

I am grateful to the Muon g-2 collaboration as a whole and the tracker team, especially for how welcoming and supportive they have been during my experience.

I would like to thank my family and close friends for putting up with me during my PhD and supporting me every step of the way. Especially my parents, sister, niece and friends at home and in York and Leeds for keeping me sane.

Finally, I would like to thank my boxing coach, Samuel Fields, for instilling a new sense of confidence and sharpening my mind and health during my PhD.

Chapter 1

Introduction

The Standard Model (SM) is currently the prevailing theory of particle physics and has had a tremendous level of success in predicting and explaining many fundamental properties of particles, interactions, and phenomena to great precision. This model, however, fails to explain many phenomena that we know about the observable universe. For example, it does not predict or explain the nature of the baryon asymmetry of the universe, the existence of dark matter, the source of dark energy, and the neutrino mass. To explain these phenomena it is clear that revisions and extensions to the SM need to be made and therefore experiments need to be devised to probe possible new physics.

The anomalous contribution to the magnetic moment of leptons $a_l = (g-2)_l/2$ is currently the most precisely determined quantity within the phenomenological framework of the SM as well as experimentally and therefore stands as an excellent area to probe for beyond the Standard Model (BSM) physics.

The Brookhaven National Laboratory (BNL) experiment published its final results in 2006 [1]. This measurement of the anomalous magnetic moment of the muon had a $\sim 3.6\sigma$ discrepancy with respect to the SM prediction. As the experimental measurement includes contributions from all possible effects whether they be SM effects or from new BSM physics, this discrepancy was potentially an indication of new physics.

To investigate this, The Fermilab Muon g-2 Experiment, situated in Batavia, Illinois was built in 2013–2018 and announced its first results in 2021 and determined the value of a_μ to a precision of 0.46 ppm [2] using the Run-1 data and was in agreement with the results of the BNL measurement. Following this result in 2023 the Muon g-2 experiment announced the latest determination of a_μ using the Run-2 and Run-3 data achieving a remarkable precision

of 0.2 ppm.

A comparison of this result with the 2020 SM prediction [3] yields a discrepancy of $5.0\,\sigma$. However recent SM determinations from lattice QCD and dispersive e^+e^- data are significantly different from the 2020 SM prediction and an intensive campaign is underway to provide a new SM prediction.

The principle measurement of the Muon g-2 experiment utilises the experiment's calorimeter detectors. In this thesis a measurement of the spin precession frequency of the muon utilising the experiment's two straw-tracking detectors is presented. Although the straw-tracking measurement uses a much lower number of reconstructed muon decays than the calorimeter detectors, a measurement across the full Muon g-2 dataset can achieve a statistical precision comparable to the BNL and Run-1 Fermilab Muon g-2 measurements. But, importantly the measurement provides an invaluable cross-check of the calorimeter result with different, and reduced, systematic uncertainties.

Chapter 2 discusses the history of the experimental approach, the phenomenology of the determination of a_μ in the framework of the SM, and the latest theory results. Chapter 3 introduces the experimental technique of determining a_μ, Chapter 4 discusses the experiment principle and design of the Muon g-2 experiment, Chapter 4.7 focuses on the hardware design of the calorimeter, Chapter 5 describes the design principle and hardware of the straw tracker detectors. Chapter 6 details a new algorithm for determining the track arrival time, t_0. Chapter 7 demonstrates both an analytical and empirical approach to correcting for pileup in the straw tracker detectors which is when multiple tracks arrive close in time and cannot be distinguished from one another. Chapter 8 describes the first evaluation of the anomalous spin precession frequency using the straw tracking detectors. Chapter 9 describes the evaluation of the systematic uncertainties on the ω_a measurement. Finally, Chapter 10 provides conclusions with an outlook on the future of the ω_a measurement.

Chapter 2

Phenomenology

The Standard Model of particle physics is the benchmark for all of particle physics. It describes particles and their interactions and has successfully predicted and led to the discovery of particles and their fundamental properties. The Standard Model particles comprises primarily two distinct groups. Firstly, there are the fundamental (point-like) fermions. These particles are spin 1/2 particles and consist of leptons (electron, muon, tau, and their counterpart neutrinos) and also quarks (up, down, top, bottom, charm, and strange).

The interactions of these fermions are facilitated by gauge bosons for each respective force. The electromagnetic interaction is facilitated by photons (γ), the weak interaction by three gauge bosons (W^+, W^-, Z^0), and the strong interaction by the gluon (g). Point-like fermions have four fundamental properties: charge, mass, spin, and a magnetic dipole moment. This chapter will define the magnetic dipole moment within quantum mechanics and the framework of the Standard Model, we then discuss more specifically the contributions to the magnetic dipole moment of the muon within and beyond the Standard Model.

2.1 Magnetic dipole moments

The magnetic dipole moment ($\vec{\mu}$) of a fundamental fermion is related to its spin ($\vec{s}$)through

$$\vec{\mu} = g\frac{q}{2m}\vec{s}, \tag{2.1}$$

where g is the gyromagnetic ratio of the particle, q is the charge, and m is the mass of the particle.

Within the framework of relativistic quantum mechanics, Dirac came to the result that for a charged point-like fermion, $g = 2$ [4, 5]. This result was shown to hold at tree-level (contains no closed loop interactions). However in relativistic quantum field theories (RQFT), one must consider higher order loop contributions, commonly known as radiative corrections. In 1948, Schwinger, motivated by measured anomalies in the hyperfine structure of hydrogen, calculated the first order loop correction to the g-factor in the framework of quantum electrodynamics (QED) [6].

Due to the addition of these corrections, the magnetic dipole moment can be written in the form

$$\vec{\mu} = (2 + 2a_l)\frac{q}{2m}\vec{s}, \tag{2.2}$$

where the factor 2 represents the tree-level Dirac contribution ($g = 2$) and a_l represents the anomalous correction given by the equation

$$a_l = \frac{(g-2)}{2}. \tag{2.3}$$

Analogously, Dirac determined, via his relativistic theory, the possibility of an electric dipole moment (EDM) with the relation

$$\vec{d} = \eta\frac{q}{2m}\vec{s} \tag{2.4}$$

with η representing a dimensionless constant analogous to g. Including both these dipole moments results in the following Hamiltonian for a charged lepton in the presence of both an electric and magnetic field:

$$\mathcal{H} = \vec{\mu}\cdot\vec{B} - \vec{d}\cdot\vec{E} \tag{2.5}$$

with $\vec{B}$ and $\vec{E}$ representing the magnetic field and electric field strengths respectively. From this Hamiltonian and the respective transformation properties, it can be seen that the term $\vec{\mu}\cdot\vec{B}$ is even under all CPT symmetries and the term $\vec{d}\cdot\vec{E}$ is odd under P and T [7]. This property shows that the EDM is a CP-odd quantity and thus that the existence of a non-zero charged lepton EDM would imply a previously undiscovered source of CP violation. New sources of CPviolation are necessary to explain the apparent baryon asymmetry of the universe, which cannot be explained, in full, by the CP-violation of the quark sector described by the CKM matrix.

Schwinger calculated the first-order loop contributions to the magnetic dipole moment. This calculation was the first demonstration of the power of RQFTs and renormalization. The tree-

level vertex and one loop function of the electromagnetic interaction between the charged lepton and the photon is shown in Figure 2.1. This function takes the form

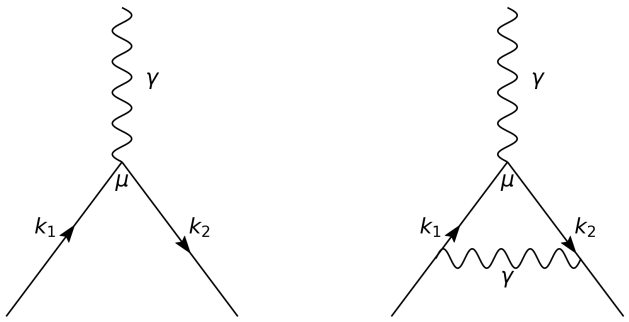

(a) (b)

Figure 2.1: Tree-level and One-loop Feynman diagrams for the electromagnetic interaction between a charged lepton and a photon

$$\Gamma^{\mu}_{\text{tree-level}}(k_1, k_2) = -ie\gamma^{\mu}, \tag{2.6}$$

where μ denotes a Lorentz index, k_i denotes the fermion momenta, e is the fundamental QED charge and γ^{μ} denotes the Dirac matrices. In QED, the anomalous magnetic moment contribution to g comes from the sum of contributions of all one-particle irreducible diagrams to all orders. The general form of the QED vertex can be written as

$$\Gamma^{\mu}\left(k_1, k_2\right) = -ie\left[\gamma^{\mu} F_1\left(q^2\right) + \frac{i\sigma^{\mu\nu} q_{\nu}}{2m} F_2\left(q^2\right)\right], \tag{2.7}$$

where $\sigma^{\mu\nu} = \frac{i}{2}\left[\gamma^{\mu}, \gamma^{\nu}\right]$, and $F_1(q^2)$ and $F_2(q^2)$ are form factors. Here $F_1(q^2)$ describes the radiative corrections to a fermion's electric charge, we find that in the limit $k_2 - k_1 = q \to 0$ that the factors $F_1(0) = 1$ and $F_2(0)$ describes the anomalous magnetic moment. The first-order loop correction to $F_2(0)$ as shown in [8] is

$$\begin{aligned} F_2\left(0\right) &= \frac{\alpha}{2\pi} \int_0^1 dx\, dy\, dz\, \delta(x + y + z - 1) \frac{2m^2 z(1-z)}{m^2(1-z)^2} \\ &= \frac{\alpha}{\pi} \int_0^1 dz \int_0^{1-z} dy \frac{z}{1-z} = \frac{\alpha}{2\pi}, \end{aligned} \tag{2.8}$$

which allows us to arrive at the one-loop correction to the g-factor

$$a_l \equiv \frac{g-2}{2} = \frac{\alpha}{2\pi} \approx 0.0011614. \tag{2.9}$$

This value was consistent with the observed 50 ppm hyperfine splitting in hydrogen measured by Kusch and Foley [9] and vindicated QED. The gyromagnetic ratio of the muon, g_μ, was then measured in a series of experiments using stopped muons at Columbia's Nevis Laboratory [10], with values again consistent with Schwinger's evaluation.

From 1962 to 1979, CERN utilized the muon's spin vector kinematics in the presence of a magnetic field to measure the anomaly directly [11, 12, 13]. This exploited the fact that the frequency with which the muon's spin vector precesses in a magnetic field is proportional to $g-2$, setting the groundwork for future experiments. CERN-3 achieved a precision of 7.3 ppm and was consistent with the Standard Model.

Using the same method with several improvements to the technique, e.g. muon injection rather than pion injection, a more intense beam, and a more stable uniform magnetic field, the Brookhaven National Laboratory [1] g-2 experiment improved the precision of the measurement by a factor of 13.5. The final BNL result was

$$a_\mu^{\mathrm{BNL}} = 116592089(63) \times 10^{-11}. \tag{2.10}$$

This result was measured at a precision of 0.55 ppm and disagreed by 3σ with the Standard Model value at the time. In 2021, the Fermilab Muon g-2 experiment announced its first measurement of a_μ to a precision of 0.46 ppm [2] using the Run-1 data, in agreement with the results of the BNL measurement. Following this result in 2023, the Muon g-2 experiment announced the latest evaluation of a_μ using the Run-2 and Run-3 data to achieve a precision of 0.2 ppm. The value for this result was

$$a_\mu^{\mathrm{FNAL}} = 116592055(24) \times 10^{-11}. \tag{2.11}$$

With this latest result combined with the value from the Run-1 dataset and the BNL result, the new world average for the experimental determination of a_μ is

$$a_\mu^{\mathrm{exp}} = 116592059(22) \times 10^{-11}, \tag{2.12}$$

with a precision of 0.19 ppm. The experimental values from the BNL and Fermilab Muon g-2 experiments can be seen in Figure 2.2.

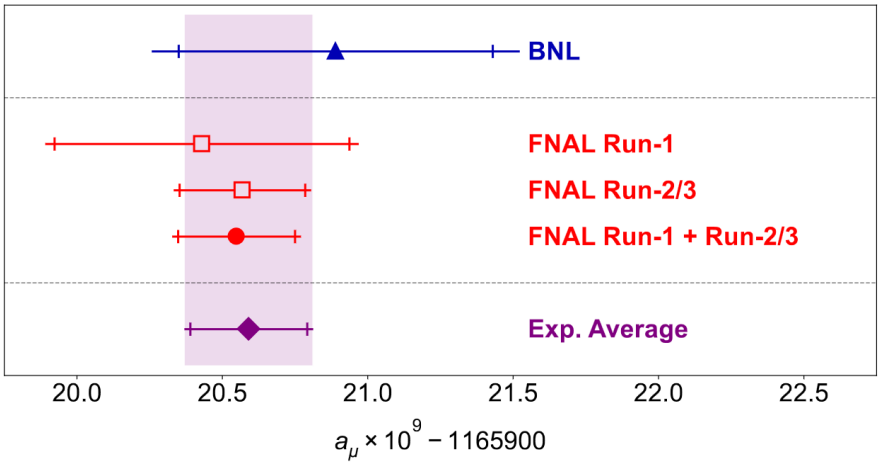

Figure 2.2: Experimental values of a_μ from the BNL experiment and Fermilab Muon g-2 experiment, and the experimental average [14].

2.2 Contributions to a_μ within the Standard Model

In the Standard Model, there are three contributions to the magnetic dipole moment of leptons. The first pertains to EM interactions via leptons and photons. The second from interactions via the electroweak (EW) bosons ($W^\pm, Z^0, H$). The third from interactions via hadrons, which interact via the strong force. This allows us to recompose a_μ^{SM} as

$$a_\mu^{SM} = a_\mu^{\text{QED}} + a_\mu^{\text{EW}} + a_\mu^{\text{Hadron}} \,. \tag{2.13}$$

2.3 QED and electroweak contribution

The electromagnetic contribution, a_μ^{QED}, is the dominant contribution to a_μ^{SM} with over 99% of the value coming from this sector. These contributions stem from virtual leptons and photons and have been calculated to a five-loop level via numerical and analytical methods [15]. The sum of these contributions can be expressed as a perturbation expansion of the form

$$\begin{aligned} a_\mu^{\text{QED}} &= \sum_{n=1}^{\infty} C_n \left(\frac{\alpha}{\pi}\right)^n \\ &= (11658471.8971 \pm 0.0007) \times 10^{-10}, \end{aligned} \tag{2.14}$$

with C_n representing the coefficient to be calculated, α is the fine structure constant, and n is the loop level. Although this is the dominant contribution, it leads to the smallest systematic uncertainties in evaluating a_μ^{SM}. The EW contributions, a_μ^{QED}, arise from Feynman diagrams containing one of the electroweak bosons (W, Z^0, and Higgs). Due to this, the process is heavily

suppressed by the mass scaling of $(m_l^2/M^2_{W^\pm,Z^0,H})$ making this a sub-leading contribution. The current result for the EW contribution is [16]

$$a_\mu^{\rm EW} = 153.6(1.0) \times 10^{-11}. \tag{2.15}$$

2.4 Hadronic contributions

2.4.1 Hadronic vacuum polarisation

The leading hadronic correction to a_μ^{SM} comes from, at first order, the one-loop correction to the photon propagator via the hadronic vacuum polarisation (HVP). Due to the strong coupling constant being large in the low energy region leading to quark confinement, this contribution cannot be calculated perturbatively. By utilizing the optical theorem of the scattering matrix and experimental e^+e^- data, Bouchet and Michel [17] determined that the leading order HVP could be calculated via dispersion integrals of the form

$$a_\mu^{HVP,LO} = \frac{1}{4\pi^3}\int_{4m_\pi^2}^{\infty} dsK(s)\sigma^{(0)}(s) = \frac{\alpha^2}{3\pi^2}\int_{4m_\pi^2}^{\infty} dsK(s)R(s). \tag{2.16}$$

Here, $K(s)$ is a calculable kernel function, and $R(s)$ is:

$$R(s) = \frac{\sigma\left(e^+e^- \rightarrow \text{ hadrons }\right)}{\sigma\left(e^+e^- \rightarrow \mu^+\mu^-\right)}. \tag{2.17}$$

The numerator represents the "bare" cross-section where vacuum polarisation effects are neglected, and the denominator is the point like muon-pair cross-section. Differences in the measured $e^+e^- \rightarrow 2\pi$ cross section between the KLOE [18] and BaBar [19] experiments are responsible for over 70% of the total systematic uncertainty on the HVP estimate. This is accounted for in the collective theory uncertainty; however, this will need to be minimized with further data-driven analysis. A full breakdown of the dispersive results is available in Ref. [3].

The HVP contribution can also be determined using Lattice QCD, but until 2021 these calculations had large uncertainties. In 2021, a determination with a significantly reduced uncertainty was released by the BMW group [20]. This result has a discrepancy with respect to the dispersive relation of 2.1 standard deviations(σ) [21]. This tension between the two approaches is being scrutinised and further Lattice QCD determinations of a_μ are being undertaken by other groups. The value for the HVP contribution, pending a consensus update from the theoretical

community, is:

$$a_\mu^{\text{had, HVP}} = 6845(40) \times 10^{-11}. \tag{2.18}$$

2.4.2 Hadronic light-by-light scattering

The second contribution to the hadronic correction is the hadronic light-by-light (HLBL) scattering contribution. This contribution derives from interactions such as the one shown in Figure 2.3. This interaction contains a four-point function instead of the simpler two-point function of the HVP, and therefore, the calculations for this contribution have significant model dependencies. The current accepted, model-dependent, determination is the so-called "Glasgow consensus" [22] and has a value of:

$$a_\mu^{\text{HLbL}} = (10.5 \pm 2.6) \times 10^{-10}. \tag{2.19}$$

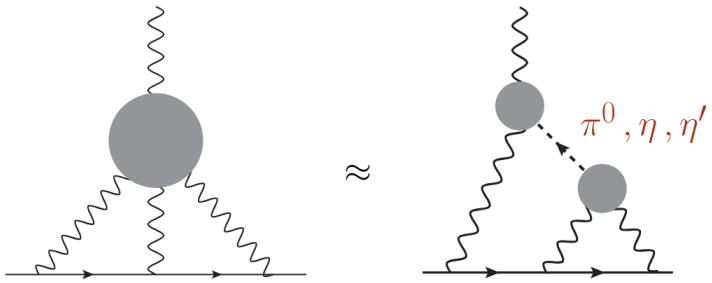

Figure 2.3: Feynman diagram (left) representing the three-photon HLBL contribution to a_μ. They can be approximated by a pseudo-scalar pole contribution (right) [23].

2.5 Beyond the Standard Model

Currently, the magnetic dipole moment of the electron is the most precisely measured quantity in the Standard Model [24], so it begs the question, why are we focused on the muon? Beyond the Standard Model (BSM), contributions to the anomalous magnetic dipole moment from a BSM particle with mass M scale as (m_l^2/M^2) where $M \gg m_l$, and m_l is the mass of the charged lepton. From this, we can express the ratio from the contribution to the electron and muon anomaly as

$$\frac{a_\mu}{a_e} \approx \frac{(m_\mu/M)^2}{(m_e/M)^2} = \left(\frac{m_\mu}{m_e}\right)^2. \tag{2.20}$$

As the muon mass is ≈ 207 greater than the electron mass, then the BSM contribution to the muon anomaly is a factor of $\approx 4 \times 10^4$ larger, which outweighs the better precision from the electron measurement. This mass-squared relationship comes implicitly from the requirement that the anomaly is gauge invariant, which forces the corresponding operator to be of at least dimension six [25].

The tau lepton has a mass of $\approx 1780\,\mathrm{MeV}$ resulting in a factor of $\approx$79 times larger BSM contribution compared with the muon. However, the tau lepton has a lifetime of $\approx$290 fs, and predominantly decays hadronically, making the measurement of a_τ very challenging. Presently there is only a limit [26, 27] on its value of:

$$0.052 < a < 0.013 \tag{2.21}$$

at the 95% CL.

Interactions contributing to a_μ have to be chirality flipping, flavour conserving, CP conserving and loop induced. This puts stringent constraints on the BSM interactions that can contribute to a_μ which is generally parameterised as:

$$\Delta a_\mu^{BSM} = C_{\mathrm{BSM}} \left(\frac{m_\mu}{M_{\mathrm{BSM}}} \right)^2 , \tag{2.22}$$

where C_{BSM} is a model-dependent coefficient. BSM interactions also contribute to the muon mass. To avoid significant changes to the muon mass the BSM mass needs to be $M_{\mathrm{BSM}}) \lesssim 2.1\,\mathrm{TeV}$ for $C_{\mathrm{BSM}} \sim \mathcal{O}(1)$. Null-results from LHC searches for BSM phenomena also further restrict the possible BSM contributions. BSM extensions able to provide an increased value of a_μ are not excluded by LHC data include dark photon models, two-Higgs doublet models (2HDM), SUSY models, leptoquarks, and new light vector boson Z' models. These different models cover a large range of coupling and mass parameter space, e.g., the light Z' boson can have masses below 1 GeV, whereas scalar leptoquark masses are constrained to be above 1 TeV. A summary of these models is presented in [28].

Chapter 3

Experimental measurement

In order to measure the anomalous magnetic dipole moment of the muon, we must first understand how a charged particle with a dipole moment behaves in a magnetic field. The torque, that acts on a dipole in a magnetic field can be described by the expression

$$\vec{\tau} = \vec{\mu} \times \vec{B} + \vec{d} \times \vec{E}, \tag{3.1}$$

where $\vec{\mu}$ is the magnetic dipole moment, $\vec{B}$ is the magnetic field, $\vec{d}$ is a potential non-zero electric dipole moment and $\vec{E}$ is the electric field. This torque causes the spin of the particle to turn with a spin-precession frequency ω_S, which can be expressed as [29]

$$\vec{\omega_S} = -g\frac{q}{2m}\vec{B} - (1-\gamma)\frac{q}{\gamma m}\vec{B}, \tag{3.2}$$

where g is the gyromagnetic ratio factor, m is the particle mass, q is the particle charge, and γ is the relativisitic Lorentz factor. If the momentum is perpendicular to the magnetic field, the particle's momentum will also orbit at the cyclotron frequency described by

$$\vec{\omega_c} = -\frac{q}{\gamma m}\vec{B}. \tag{3.3}$$

The difference between $\vec{\omega_S}$ and $\vec{\omega_c}$ is defined as the anomalous precession frequency ω_a, and is proportional to the anomalous magnetic dipole moment. This is expressed as

$$\vec{\omega_a} = \vec{\omega_s} - \vec{\omega_c} = -\frac{g-2}{2}\frac{q}{m}\vec{B} = -a\frac{q}{m}\vec{B}. \tag{3.4}$$

The muon beam has a small transverse momentum component coupled with inhomogeneities in the magnetic field causes the muon beam to diverge vertically. Vertical focusing is required to maintain the beam within the storage ring aperture for a sufficient time to measure ω_a. Electrostatic quadrupoles provide this vertical focusing, which introduces an electric field term in the expression for ω_a:

$$\vec{\omega}_a = -\frac{q}{m}\left[a\vec{B} - \left(a - \frac{1}{\gamma^2 - 1}\right)(\vec{\beta} \times \vec{E})\right], \tag{3.5}$$

However, if muons whose momentum satisfies the conditions:

$$\left(a - \frac{1}{\gamma^2 - 1}\right) = 0 \tag{3.6}$$

are selected, this second term vanishes. For the muon, the so-called "magic-momentum" that causes this term to vanish is defined by:

$$\gamma_0 = \sqrt{\frac{1}{a_\mu} + 1} = 29.3. \tag{3.7}$$

This boost factor corresponds to a momentum $p_0 = 3.094\,\mathrm{GeV}$. This momentum sets the constraints of the experiment, and in a perfect scenario, all muons would move with this momentum. However, this is not the case, and the effect of deviations away from the magic-momentum need to be accommodated in the measurement of ω_a.

To achieve the measurement of a_μ, it is also essential to measure the magnetic field to a high precision. This is done through a measurement of the Larmor frequency of a free proton, ω_p, which is defined as

$$\omega_p = -g_p \frac{e}{2m_p} B, \tag{3.8}$$

where g_p is the gyromagnetic ratio of the proton, and m_p is the proton mass. The magnetic field is thus defined by the relationship:

$$\vec{B} = \frac{\hbar\omega_p}{2\mu_p}, \tag{3.9}$$

where μ_p is the magnetic dipole moment of the proton. The electric charge can also be expressed in terms of electron quantities, i.e.,

$$e = \frac{4m_e\mu_e}{\hbar g_e}, \tag{3.10}$$

where m_e is the electron mass, μ_e is the magnetic dipole moment of the electron, and g_e is the

gyromagnetic ratio of the electron. With these expressions, we can now express a_μ in terms of measurable quantities as

$$a_\mu = \frac{\omega_a}{\tilde{\omega}_p} \frac{g_e}{2} \frac{\mu_p}{\mu_e} \frac{m_\mu}{m_e}. \tag{3.11}$$

The quantity $\tilde{\omega}_p$ is the field measurement convoluted and averaged with the position of the muon distribution in the storage ring $M_\mu(x, y, \phi)$.

$$\tilde{\omega_p} \equiv \langle \omega_p(x, y, \phi) \times M_\mu(x, y, \phi) \rangle \tag{3.12}$$

with ϕ, the azimuthal position in the storage ring. The ratio $\omega_a/\tilde{\omega}_p$, is determined by the Muon g-2 experiment, and the target systematic uncertainty of this measurement is 140 ppb. The other quantities in Equation 3.11 are known to a much higher precision from other experiments. The gyromagnetic ratio factor of the electron, g_e, is known from one-electron quantum cyclotron experiments to a precision of 0.13 ppt [30]. The ratio between the proton and electron magnetic dipole moments, μ_p/μ_e, is known from hydrogen spectroscopy to a precision of 3.0 ppb [31]. Finally, the ratio between the muon and electron mass is determined by bound state QED [31] and the hyperfine splitting in muonium [32]. This is known to a precision of 22 ppb.

The determination of a_μ thus rests on separately measuring ω_a and ω_p in the experiment.

3.1 Determining ω_a and ω_p

The ratio ω_a /ω_p ($quiv\mathcal{R}'_\mu$) can be expressed in terms of the quantities the experiment measures as:

$$\mathcal{R}'_\mu = \frac{\omega_a}{\omega_p} = \frac{f_{\text{clock}}\, \omega_a^{\text{meas}}\, (1 + C_e + C_p + C_{pa} + C_{ml})}{f_{\text{calib}}\, \left\langle \tilde{\omega}'_p(x, y, \phi) \times M(x, y, \phi) \right\rangle (1 + B_k + B_q)}, \tag{3.13}$$

where,

- ω_a^{meas} is the measured spin-difference precession frequency determined from the positron time distribution
- $\tilde{\omega}'_p(x, y, \phi)$ is the precession frequency of a proton calibrated to an equivalent precession frequency of a proton shielded in a sphere of water at a calibration reference temperature of 34.7°C, measured as a function of the azimuthal position and the muon spatial distribution as measured by the tracking detectors, $M(x, y, \phi)$.
- The two B_x terms are time-dependent transient effects that affect the magnetic field.

- The C_x terms are corrections arising from the spatial and temporal motion of the beam.
- f_{clock} is a relative unblinding conversion factor from the clock used to measure ω_a
- f_{calib} is an unblinding conversion factor from NMR probes used to measure the magnetic field.

Each of these terms will be defined and discussed in more detail in the following sections.

3.2 The ω_a measurement

In order to measure ω_a , the decay kinematics of the muon must be considered. The main decay mode of the positive muon is to a positron, an electron neutrino, and a muon anti-neutrino. Due to the parity-violating nature of the weak interaction, the positron will preferentially be emitted with right-handed chirality and with spin vector in the direction of its momentum. Due to the conservation of angular momentum, positrons emitted with maximal energy in the muon rest frame will travel in the opposite direction to the neutrinos, both traveling in the same direction. The spin of the positron is parallel to the spin of the muon at the time of decay. However, positrons emitted with minimal energy, where the neutrino and anti-neutrino travel in opposite directions, will have spin anti-parallel to that of the muon at the time of decay. Thus by measuring the energy of the emitted positrons, the direction of the muon spin can be obtained.

Muons within the storage ring will orbit at the cyclotron frequency and will precess with the anomalous precession frequency, ω_a. For a polarized muon beam, the probability of a positron having an energy fraction $y = E/E_{max}$ emitted at an angle θ with respect to the muon spin is:

$$dP(y,\theta) \propto N(y)[1 + A(y)\cos(\theta)]dy\, d\Omega \tag{3.14}$$

where $N(y)$, is the number-distribution of the decay positrons, $A(y)$ referred to as the "asymmetry" is an energy-dependent factor encoding the correlation between the muon spin and positron direction. As the high-energy positrons are emitted parallel to the muon-spin at the time of decay, θ is also defined by $\theta = \omega_a t + \phi$, where ϕ is the phase of the muon ensemble at the point of injection. In the rest-frame of the muon, $N(y)$ and $A(y)$ are defined as

$$N(y) = 2y^2(3 - 2y), \tag{3.15}$$

$$A(y) = \frac{2y-1}{3-2y}. \tag{3.16}$$

Their form is changed by the Lorentz boost to the laboratory frame, and assuming a unity polarisation, they become:

$$N_0(E) \propto (y-1)\left(4y^2-5y-5\right) \tag{3.17}$$

$$A(E) = \frac{-8y^2+y+1}{4y^2-5y-5}. \tag{3.18}$$

Finally the number of positrons above a certain energy threshold, E_{th}, is given by the following expression

$$N\left(t, E_{th}\right) = N_0\left(E_{th}\right) \cdot e^{-t/\gamma\tau_\mu} \cdot \left[1 + A\left(E_{th}\right)\cos\left(\omega_a t + \phi\left(E_{th}\right)\right)\right]. \tag{3.19}$$

The straw tracking detectors measure momentum and not energy and an analogous function based on a momentum threshold, p_{th}, is defined for positrons measured in the straw tracking detectors:

$$N\left(t, p_{th}\right) = N_0\left(p_{th}\right) \cdot e^{-t/\gamma\tau_\mu} \cdot \left[1 + A\left(p_{th}\right)\cos\left(\omega_a t + \phi\left(p_{th}\right)\right)\right]. \tag{3.20}$$

Introducing $y_{th} = p_{th}/p_{max}$, then we have the following expressions for $N_0\left(p_{th}\right)$ and $A\left(p_{th}\right)$:

$$N_0\left(p_{th}\right) \propto \left(y_{th}-1\right)^2\left(-y_{th}^2+y_{th}+3\right), \tag{3.21}$$

$$A\left(p_{th}\right) = \frac{y_{th}\left(2y_{th}+1\right)}{-y_{th}^2+y_{th}+3}. \tag{3.22}$$

With these expressions, we can thus determine ω_a by a fit to the number of positrons above this momentum threshold.

A scan must be performed to find the optimal threshold for the measurement. The statistical uncertainty on the ω_a measurement is defined by [33]

$$\frac{\sigma_{\omega_a}}{\omega_a} = \frac{\sqrt{2}}{\sqrt{N_{\text{total}}}\,A\gamma\tau\omega_a} \tag{3.23}$$

The statistical precision of ω_a is minimised when the quantity NA^2 is at its maximum. Figure 3.1 shows that 1.8 GeV is the optimal momentum threshold.

3.3 The ω_p measurement

To achieve the experimental goals of the experiment, it is imperative to measure the magnetic field around the storage ring to a high precision. The experiment aims to measure the magnetic

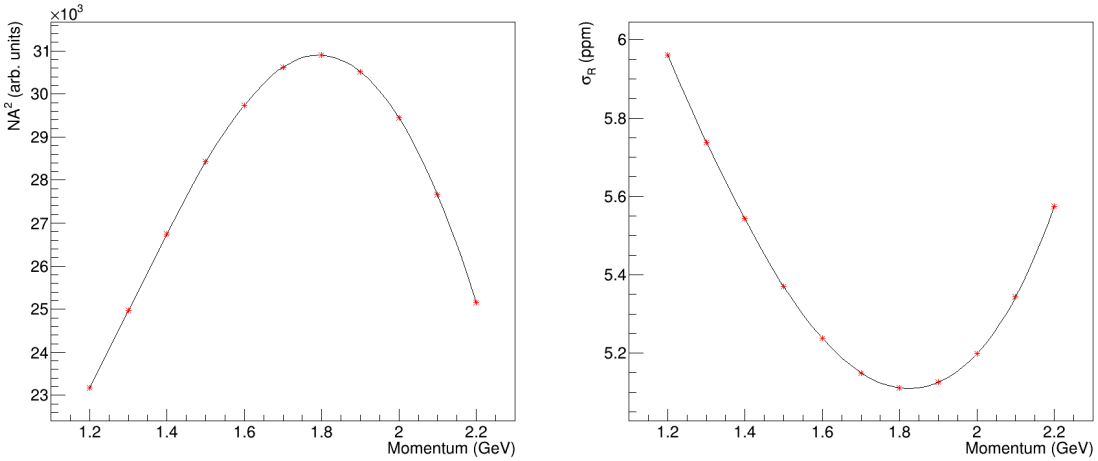

(a) (b)

Figure 3.1: (a) NA^2 and (b) σ_R as a function of the momentum threshold.

field to an uncertainty of 70 ppb and to ensure the magnetic field is a uniform 1.45 T around the azimuth of the ring. The cross-section of the $g-2$ magnet, including the measurement system, can be seen in Figure 3.2. The magnet consists of 36 upper and lower pole pieces to control

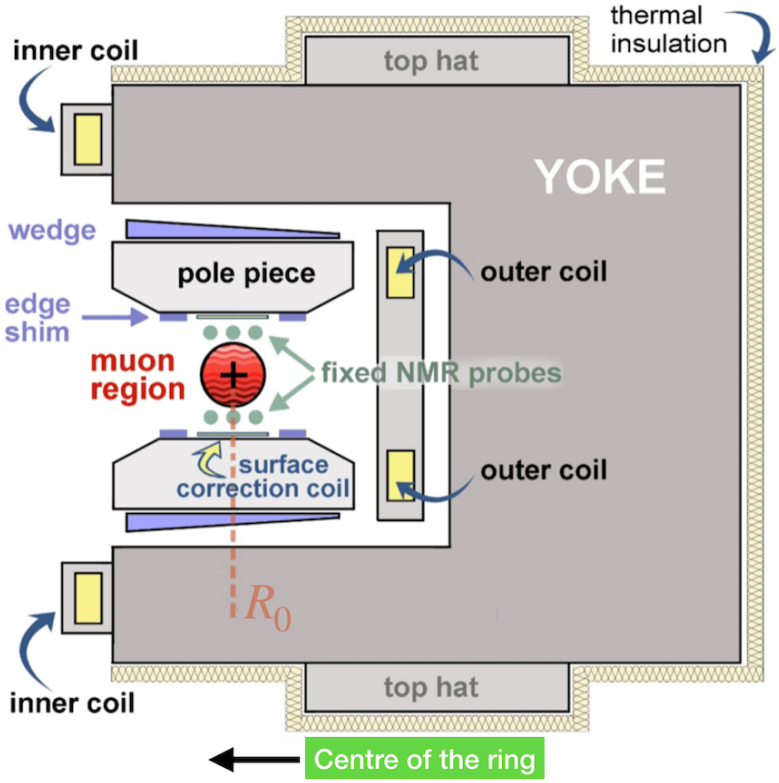

Figure 3.2: Schematic cross-section representation of the $g-2$ magnet system [34].

the magnet's field strength, with their pitch controlling the linear field gradients, and 24 yoke pieces. To ensure the magnetic field is uniform around the ring, a two-fold approach, known as "shimming", is used. The first part of the shimming allows the control of field gradients

in the transverse direction to the beam motion, as well as allowing fine-tuning control of the field as a function of the azimuth. This introduced additional iron pieces to the pole pieces, between the pole pieces and the yoke pieces, as well as above and below the yoke pieces. The second part of the shimming utilizes a system of 100 individually powered, concentric coils on the surfaces of the pole pieces. These surface correction coils (SCC) distribute specific currents across the magnets, with the currents updated periodically to track drifts in the magnetic field. This allowed the field variations over the storage ring aperture to be minimised to less than 1 ppm when averaged over the entire azimuth.

With both of these respective parts, the experiment achieved an RMS field homogeneity over the azimuth of 14 ppm [34]. The effect on the uniformity of the magnetic field provided by the shimming system can be seen in Figure 3.3. Another important facet of measuring the magnetic

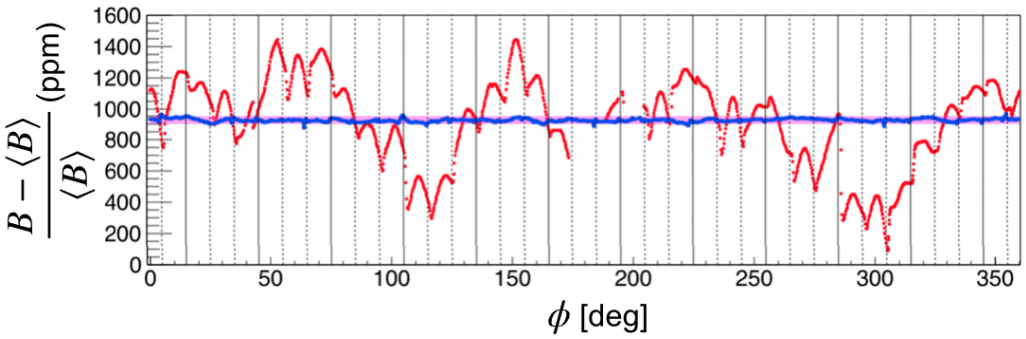

Figure 3.3: Normalised distribution of the difference between the magnetic field at a point around the ring B and the average field ($\langle B \rangle$) as a function of the azimuth around the storage ring (ϕ). The red and blue lines show the field before and after the shimming, respectively, and the purple line represents the experimental goal of 25 ppm [35]

.

field is the use of nuclear magnetic resonance (NMR) probes. NMR involves the injection of a sample of protons into the magnetic field, usually in the form of petroleum jelly or water, where they are subject to a $\pi/2$ pulse. The protons will begin to spin at the Larmor frequency (~ 61.79 MHz), from which they will begin to return to equilibrium with the external magnetic field after interacting with the inhomogeneities and local field gradients. This allows the field to be measured around the ring. Approximately once every three days, a trolley system consisting of 17 NMR probes completes a full revolution around the azimuth of the storage ring. At each point in the ring, the probes measure the free inductance decay (FID) of the protons, as shown in Figure 3.4. As the trolley cannot perform measurements when muons are stored in the ring, a second system of 378 fixed NMR probes is placed around the ring to monitor the field between trolley runs, allowing the measurement of the field to be interpolated.

This two-fold system allows the magnetic field to be mapped spatially over time for the full

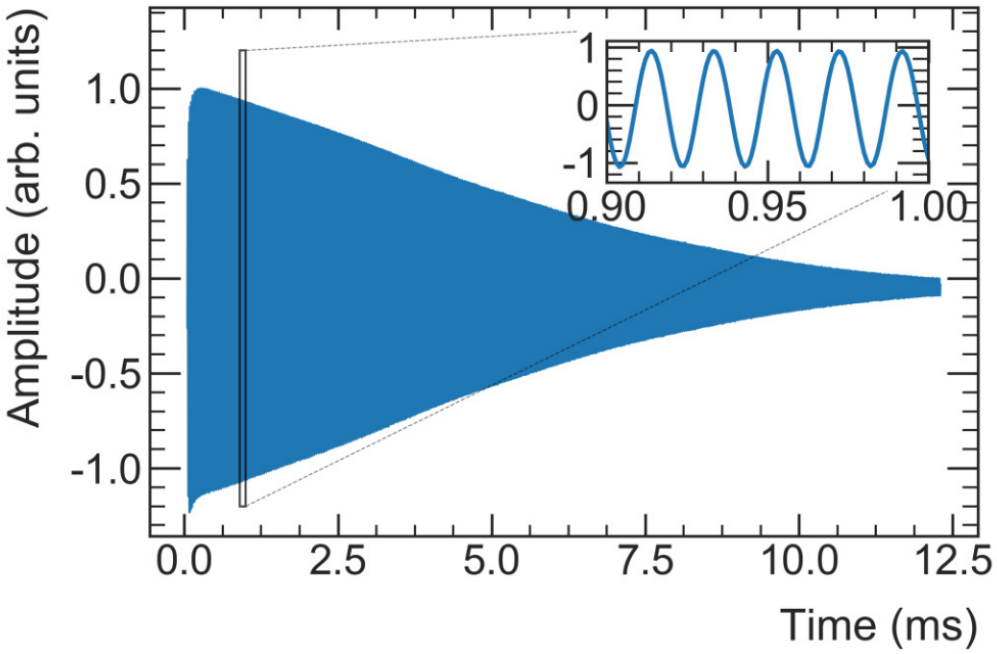

Figure 3.4: Example of a trolley probe measured free-inductance decay (FID). The inset region highlights the periodic oscillation used to measure the frequency [34].

azimuth of the ring. A map of the azimuthally averaged field can be seen in Figure 3.5. The

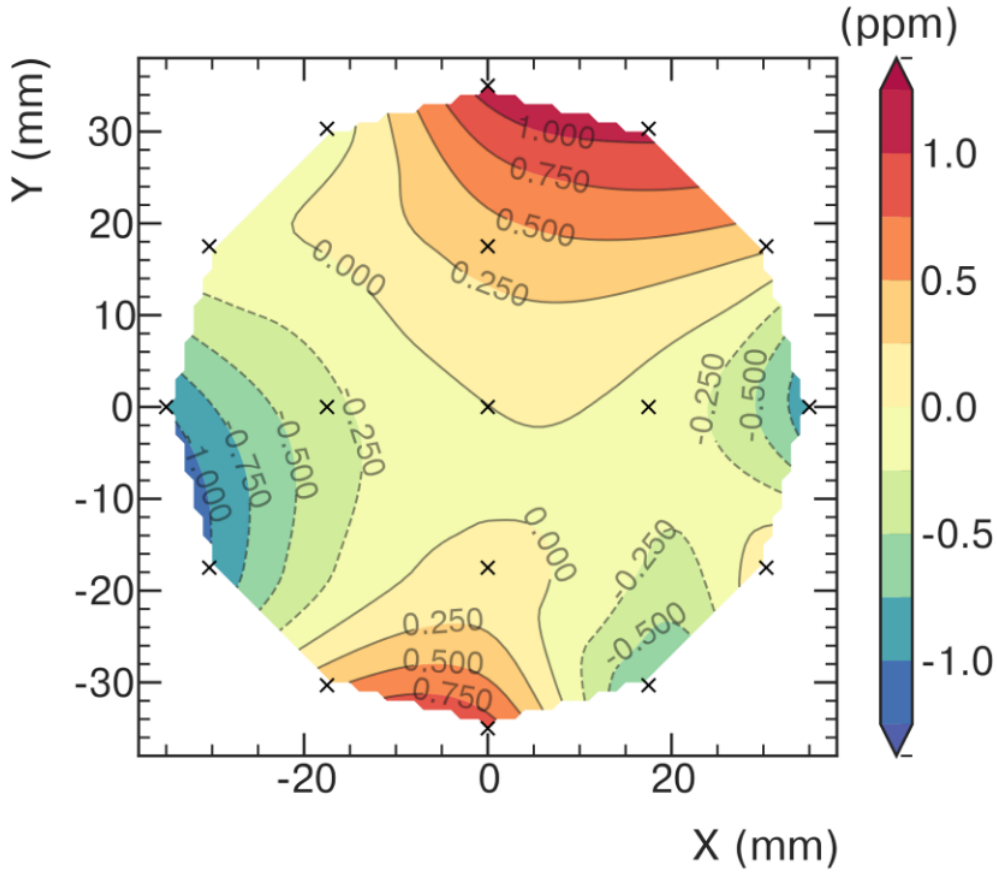

Figure 3.5: An example of an azimuthally averaged field map showing the deviations in ppm compared with the central probe. The 17 trolley NMR probes are highlighted by 'X' [34].

frequency of the FID signal, however, will be different to the free proton precession frequency of interest due to the materials of the probe and also the molecular properties of the proton sample. The measured frequency can be expressed in the form

$$\omega_{p,\text{ probe}} = \omega_{p,\text{ free}} \left(1 - \sigma\left(\mathrm{H_2O}, \mathrm{T}\right) + \delta_b + \delta_p + \delta_s\right) \tag{3.24}$$

where $(\mathrm{H_2O}, \mathrm{T})$ is a diamagnetic shielding effect of a proton in a sphere of water at a calibration reference temperature of $34.7°C$, δ_b is an applied correction due to the bulk susceptibility of the water sample, δ_p is an applied correction due to the paramagnetic impurities in the water sample and δ_s is an applied correction to account for the magnetic effects of the probe itself [7].

3.4 Corrections to ω_a

3.4.1 Electric field correction

The electrostatic quadrupoles provide a vertically focusing electric field which also makes a contribution to a_μ. However as demonstrated in Equation (3.7) by selecting a Lorentz boost factor of 29.3, most of the effect of this electric-field contribution to a_μ can be cancelled. As the stored muon momentum distribution has a variance, some of the muons that traverse the storage ring are not at the magic-momentum, see Section 3 and this necessitates the introduction of an electric field correction factor C_e. With the assumption that the muons traverse the storage ring at a defined equilibrium radius, x_e, the electric field correction can be defined as [36]

$$C_e \approx 2n(1-n)\beta_0^2 \frac{\langle x_e^2 \rangle}{R_0^2}, \tag{3.25}$$

where n, is the field index of the quadrupole field responsible for the vertical weak focusing of the beam which depends on the voltage of the electrostatic quadrupoles. The term $\beta_0^2 = p_0^2/\left[m^2c^2 + p_0^2\right]$ depends on the magic-momentum, p_0. The term R_0 is the magic radius and finally, $\langle x_e^2 \rangle$, is the mean of the square of the radial beam position that depends on both the width of the beam and the mean average of the beam position i.e. $\langle x_e^2 \rangle = \sigma_{x_e}^2 + \langle x_e \rangle^2$.

To determine the value of C_e, a "fast-rotation" analysis is performed. Due to the muons at injection having a time-spread of 120 ns, the ring will not be wholly filled since the cyclotron period is 149.2 ns. Each muon has a momentum-dependent cyclotron period that dictates the radius at which it will orbit. High-momentum muons will have a larger radius, and low-momentum muons will have a smaller radius. Due to this effect, low-momentum muons in the head of the bunch will catch up to the high-momentum muons in the tail of the bunch, thus reducing the gap between each subsequent passing of the bunch. This gap will continue to reduce, and after $\approx 30\,\mu$s, the beam will have reduced to a more stable, near-uniform intensity. This intensity variation is referred to as the "fast-rotation".

Analysis of the "fast-rotation" requires a fast-Fourier transform (FFT) of the instilled betatron oscillation (stable oscillation about the equilibrium orbit) caused by this effect, allowing for an extraction of the radial distribution of the beam.

In Run-1 the determination of C_e had a significant systematic uncertainty due to the kicker pulse instilling a time dependence in the beam's momentum [37]. For Runs 2 and 3, a detector was

developed to measure this time-momentum correlation. The minimally intrusive scintillating fiber detector (MiniSciFi) was designed to measure the spatial distribution of the beam in narrow slices of time without perturbing the beam significantly. A full overview of the design and principle of this detector can be found in [38]. In Runs-2/3, C_e was determined to be 451 ± 32 ppb [14].

3.4.2 Pitch correction

The stored muons have a small vertical component of momentum. This means that $\vec{\beta} \cdot \vec{B} \neq 0$ and, therefore, a "pitch" correction, C_p, is necessary. This pitch correction is measured by the straw tracking detectors and is of the form

$$C_p \approx \frac{n}{4} \frac{\langle A^2 \rangle}{R_0^2}, \tag{3.26}$$

where A is the amplitude of the vertical oscillation. As this correction is measured by the straw-tracking detectors, the dominant uncertainty in the measurement comes from both the alignment of these detectors and the track reconstruction. In Run-1, this correction was measured as +180 ppb with an uncertainty of less than 15 ppb [37]. In Runs-2/3, C_p was determined to be 170 ± 10 ppb [14].

3.4.3 Muon loss correction

As muons traverse the storage ring outside of the central beam orbit, there is a possibility that they will collide with the collimators that define the optimal beam aperture. When the muons collide with these collimators, they subsequently lose energy and deter from their stable orbit, causing them to spiral outside of the storage region before they are able to decay into positrons. As muons are minimally ionizing particles (MIPS), they will be registered as high momentum tracks close to the 3.094 GeV in the tracking detectors, whilst in the calorimeters, they will deposit a small amount of energy.

Some of these lost muons can be identified by matching high momentum tracks in the straw-tracker detectors to low energy clusters in the downstream calorimeter. As there are only two straw-tracking detectors in the storage ring, a more optimal way of determining the rate of these muons for the full azimuth of the storage ring can be determined from coincidences where the low energy signal is measured in multiple calorimeters. As the distance between the

calorimeters is known, the time between the muon energy deposits in adjacent calorimeters is $\sim 6.2\,\text{ns}$ as shown in Figure 3.6. If the lost muons have the same phase as those in the average

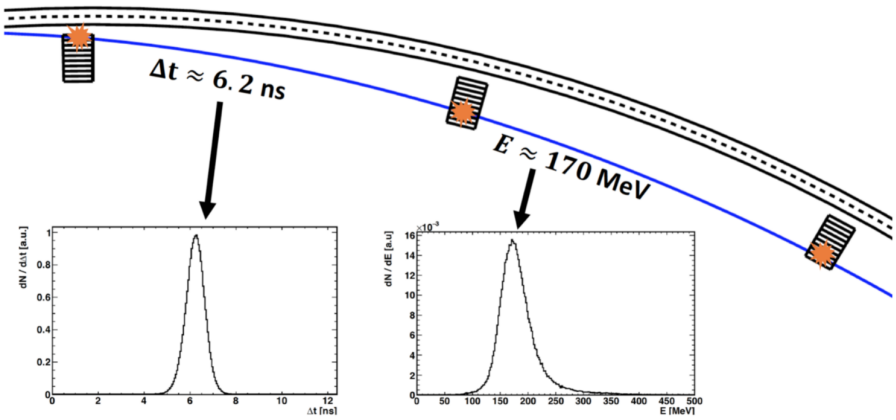

Figure 3.6: A pictorial representation of the characteristic signals of the 'lost' muons. The left shows the time difference (δ_t), between the energy deposits in two adjacent calorimeters, and the right shows the signature energy spectrum of the minimally ionising muons in the calorimeter [37].

stored muon population, this effect will be seen as merely a loss in the number of total stored particles and will not have any effect on the average phase. However, if these lost muons have a phase that is different from the average stored muon population, then a time-dependent, coherent effect will be present. This is the case if the momentum of the lost muons has a time dependence i.e.

$$\frac{d\langle p\rangle}{dt} \neq 0, \tag{3.27}$$

and also, if the phase and momentum are correlated i.e.

$$\frac{d\langle \phi\rangle}{d\langle p\rangle} \neq 0. \tag{3.28}$$

The correlation between phase and momentum has been measured and is shown in Figure 3.7. This correlation means that the phase is also time-dependent. This effect will lead to a bias in ω_a that will scale with the correlation between the phase and momentum, the absolute rate of the lost muons, and the momentum dependence of the muon losses as

$$\frac{d\langle \phi\rangle}{d\langle p\rangle} \cdot \frac{d\langle p\rangle}{dt} = \frac{d\langle \phi\rangle}{dt} = \Delta\omega_a \neq 0. \tag{3.29}$$

In Run-1, two resistors in one of the electrostatic quadrupoles were broken, leading to a large drift in the vertical position of the beam, and consequently, there was a larger rate of muon losses, leading to a significant contribution from this effect. In Runs 2 and 3, which this thesis

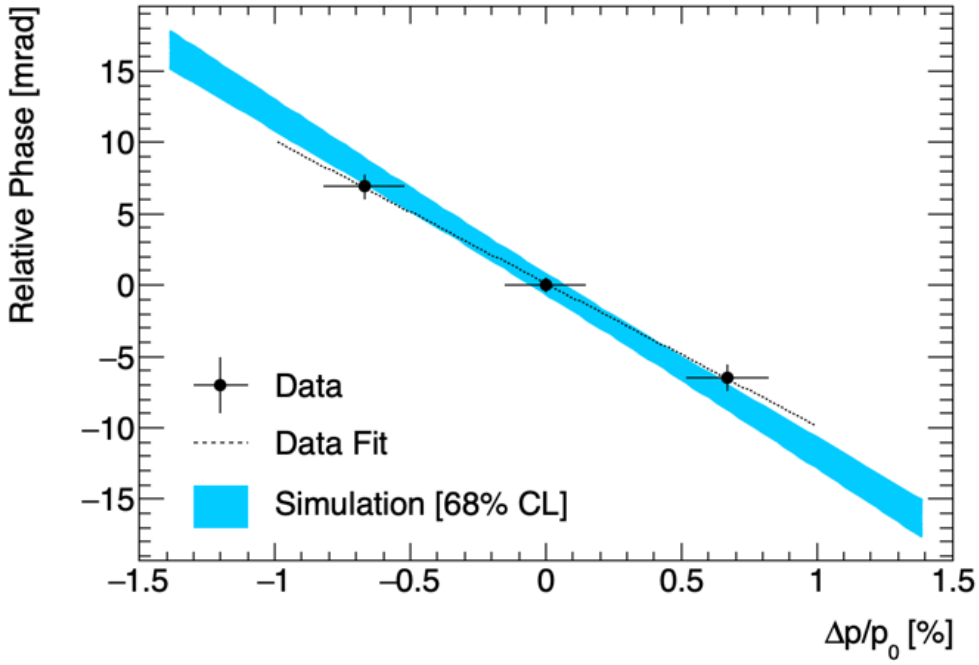

Figure 3.7: The phase-momentum correlation of the injected muon beam determined by a data-driven approach and simulation. Due to this correlation momentum-dependent effects such as muon losses can bias ω_a [39].

details, the correction factor C_{ml} and its associated uncertainty is determined to be negligible. A detailed explanation of this can be found in Ref. [37]. In Runs-2/3, C_{ml} was determined to be 0 ± 3 ppb [14].

3.4.4 Phase acceptance correction

Since the calorimeters having a non-uniform acceptance, there is a dependence on the position in the azimuth of the storage ring where the muon decayed to the probability of the subsequent decay positron being measured. Thus, this position dependence is correlated with the phase of the beam. The beam is subject to variations in the field, temperature variations, etc and it needs to be corrected with the term, C_{pa}. This effect can be seen in Figure 3.8 and Figure 3.9.

In Run-1, there is a large non-uniformity in the beam position due to broken resistors in the electrostatic quadrupoles, leading to a large systematic uncertainty. The result for C_{pa} in Run-1 is 158 ppb with an uncertainty of 75 ppb [36]. For Runs 2 and 3, these resistors were replaced, and the value and uncertainty are reduced by approximately a factor of 3 [37]. In Runs-2/3, C_{pa} is determined to be -27 ± 13 ppb.

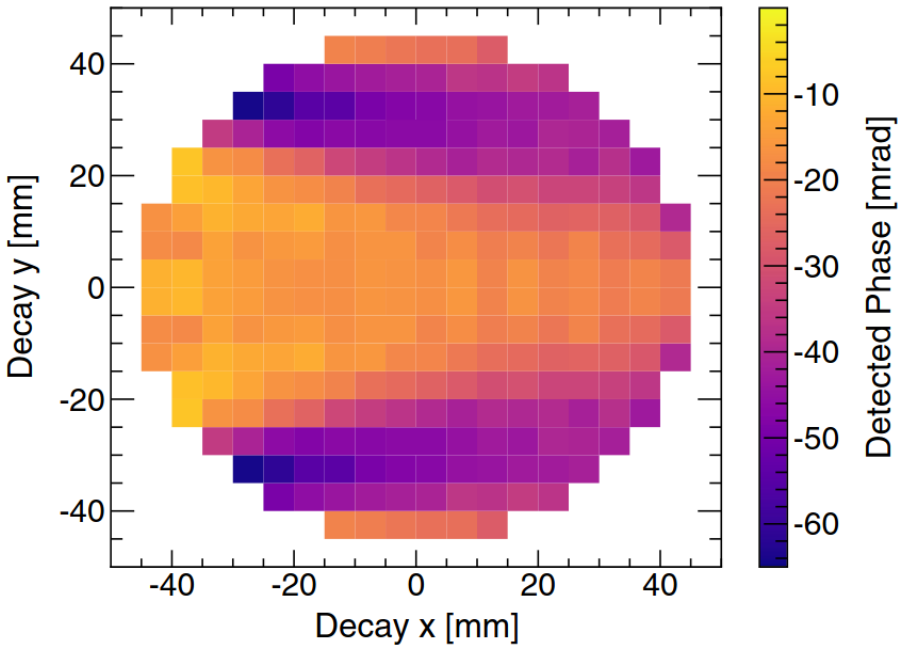

Figure 3.8: The detected phase of the beam as a function of the beam position averaged over the azimuth of the storage ring [36].

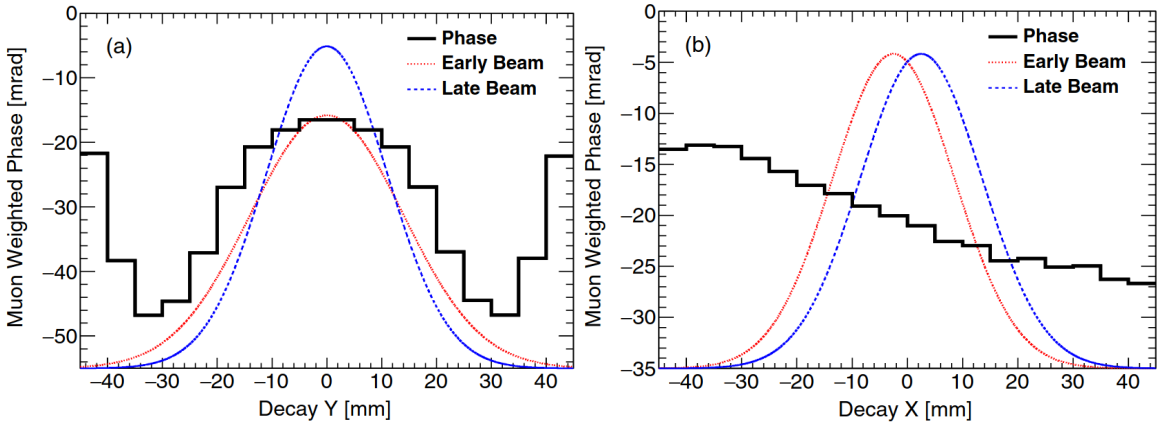

(a) (b)

Figure 3.9: (a) The phase as a function of the vertical position (black). The red (early time) and blue (late time) lines show how the vertical width changes over time and demonstrates how a changing width leads to a different detected phase. (b) The phase as a function of the radial position black) shows how the width effect is largely cancelled. Now the detected phase is dependent on the mean radial position [36].

3.4.5 Differential decay correction

As the lifetime of the muon is dependent on its momentum, this leads to an effect that couples to the phase-momentum relationship as mentioned in Section 3.4.3. Lower momentum muons will decay faster than higher momentum muons, skewing the phase-momentum distribution shown in Figure 3.7 to the left, leading to a shift in phase. This effect was not corrected for in Run-1. A correction factor for this momentum-dependent differential decay effect, C_{dd}, will be included in the analysis for Runs 2 and 3. In Runs-2/3, C_{dd} is determined to be -15 ± 17 ppb [14].

3.4.6 Blinding

The Muon g-2 experiment is a "blinded" experiment to ensure no biases are introduced in the analysis. This "blinding" is performed at both the hardware and the software level. To ensure no biases are introduced in the procedure, ω_a is taken as a parameter R, which is a ppm shift to a reference value according to the expression

$$\omega_a = 2\pi\omega_{ref} \cdot \left(1 + (R \pm \Delta R_{\mathrm{SW}} \pm \Delta R_{\mathrm{HW}}) \times 10^{-6}\right) \tag{3.30}$$

where ω_{ref} is the reference value of 0.2291 MHz and is the same as that used by the E821 BNL experiment [40]. The returned value of R is blinded in both software and hardware as ΔR_{SW} and ΔR_{HW} respectively.

At the hardware level, there is a factor f_{clock} applied to the master clock for the experiment. The 40 MHz clock is de-tuned by Fermilab employees external to the experiment to a frequency between 39.997 MHz and 39.999 MHz. The value of this de-tuned frequency is only revealed when the collaboration has decreed the analysis is complete and ready to be unblinded. At the software level, each analysis is blinded independently as

$$\omega_{ref}\left(1 + (R \pm \delta_R) \times 10^{-6}\right), \tag{3.31}$$

where the offset, δ_R, is selected from a random number generator based on a seed set by a "blinding string" independent to each analysis.

3.5 Corrections to ω_p

3.5.1 Kicker transient correction

When a pulse is generated by the kickers, subsequent eddy currents are induced in the surrounding material. These eddy currents perturb the field, leading to a transient effect, B_k. To measure this transient effect two fibre Faraday magnetometers were inserted between the kicker plates. The data extracted from the magnetometers is then fitted with a single decaying exponential from 30–700 μs after the initial kick, which matches the start time used for the ω_a analysis of the calorimeter data. This can be seen in Figure 3.10. The sources of systematic

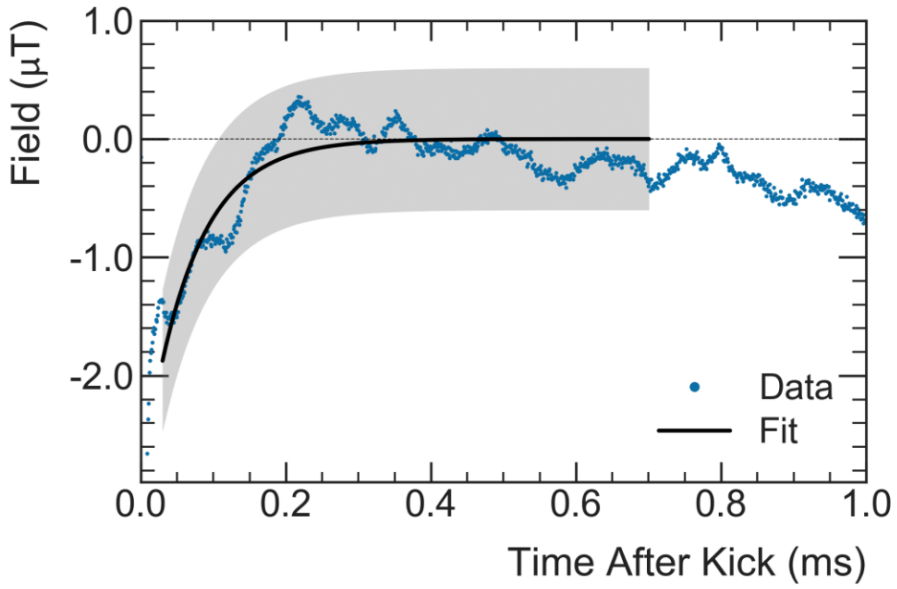

Figure 3.10: The vibration background subtracted signal measured by the fiber magnetometer. The exponential fit to the data is shown in black, and the gray shaded band represents the associated $\pm 0.6\,\mu$T uncertainty on the background subtraction [34].

uncertainty on this measurement come from a $\pm 0.6\,\mu$T uncertainty on the vibration background subtraction, the fit function, and the calibration of the magnetometers themselves [34]. For Run-1 B_k was determined to be -27 ppb [34].

3.5.2 Electro-static quadrupole transient correction

Similar to the Kicker transient effect, a transient effect is also induced from the mechanical vibrations of the charged plates of the electrostatic quadrupoles when they are pulsed. The NMR trolley probes used to measure the magnetic field are used to measure the delay time between the NMR signal and the time of the initial pulse, which is corrected for with the term

B_q. This measurement can be seen in Figure 3.11 where the grey regions correspond to the time intervals at which the electrostatic quadrupole was pulsed, and the muons that are used in the ω_a analysis. In Run-1, this effect had a large systematic uncertainty as it was only measured

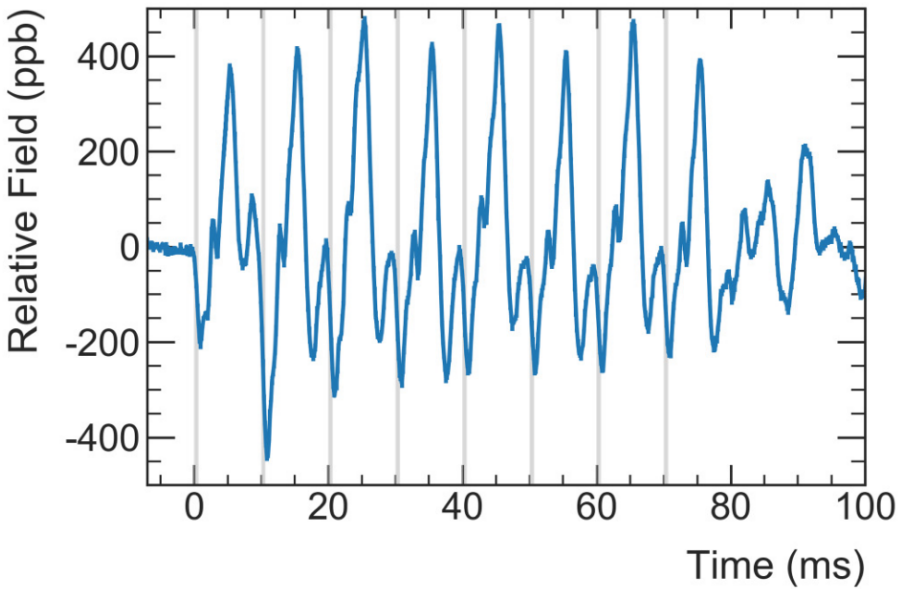

Figure 3.11: The structure of the electrostatic quadrupole transient determined by a scan over the delay time between the time of the pulse trigger and the NMR measurement. The bands shown in grey represent the time intervals where the muons are stored and are used for the precession frequency measurement [34].

in one of the twelve electrostatic quadrupole regions. For Run-1 B_q was determined to be -17 ppb with a systematic uncertainty of 92 ppb. This systematic uncertainty is expected to be significantly reduced for Runs 2 and 3 due to a dedicated field mapping of the entire azimuth of the storage ring.

3.5.3 Field calibration factor

As shown in (3.24), three effects need to be corrected to extract the frequency of the FID and measure the magnetic field. In order to minimise these effects a calibration procedure is performed. This procedure uses a "plunging" probe specifically designed to reduce these effects. The design of the plunging probe can be seen in Figure 3.12. This probe is rapidly swapped into each of the locations of the trolley probes and is then cross-calibrated both with the spherical water sample and with a ^{3}He magnetometer probe [34]. A detailed breakdown of this calibration procedure can be found in Ref. [34]. Similarly to the ω_a measurement, the calibration measurement is also blinded with a factor f_{calib}.

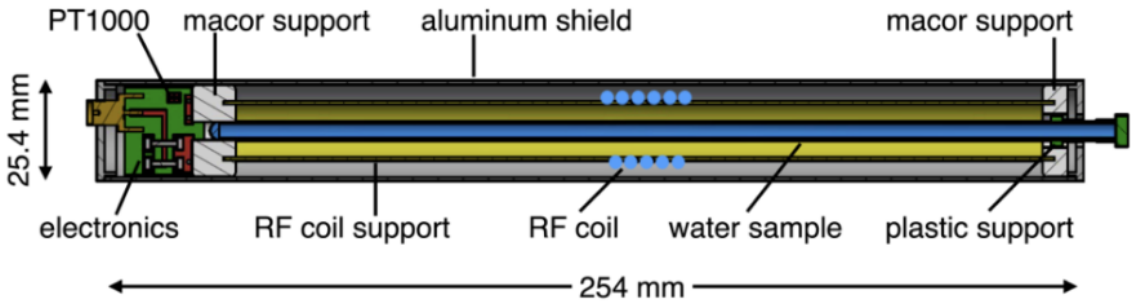

Figure 3.12: Schematic of the plunging probe used to calibrate the magnetic field measurement [34].

Chapter 4

Experimental overview

The production of the muons can be broken down into several stages. The first stage involves H- ions that are accelerated in a linear accelerator and stripped down to protons. The protons are then injected into a 75 m radius "booster" ring where they are accelerated up to 8 GeV and separated into batches consisting of 4×10^{12} protons with four batches created by the accelerator every supercycle, which lasts 1.4 s.

These batches are then injected into a "recycler" ring, where they are separated again into four bunches consisting of 1×10^{12} protons to reduce the instantaneous rates observed by the experiment's detectors. These bunches are then injected into a hall where they are directed onto a nickel-iron production target, which is optimized for the production of a high number of pions with a small momentum spread. The momentum spread is approximately $|\Delta p/p| < 2\%$ [41]. The pions are then focused with a lithium lens cylinder that has a radius of 1 cm and is 15 cm in length. A pulsed magnet is then used to select particles centred at an energy of 3.11 ± 0.15 GeV. The pions then decay to muons via:

$$\pi^+ \to \mu^+ \nu_\mu.$$

The high and low-energy muons will be forward and backward-polarised, respectively. The muons and any remaining pions are then injected into a "delivery" ring where the beam is allowed to circulate four times. During the first three rotations, almost all of the remaining pions will decay to muons, and any remaining slower proton contamination will be separated from the muon beam, where it is subsequently removed by a kicker. Forward emitted polarised muons with a momentum of 3.094 GeV are then selected, and the remaining muon beam is sent to the Muon g-2 building where it is focused by four quadrupole magnets before being injected into the Muon g-2 storage ring shown in Figure 4.1.

The requirement for the muons beam to be polarised (the muons spins all point in approximately the same direction) arises due to the fact that without this polarisation, the phase of each oscillation would interfere with each other rather than adding coherently effectively washing out the spin-precession signal when integrated over the beam ensemble. During each accelerator supercycle, the Muon g-2 experiment receives sixteen bunches in two groups of eight, where each bunch in the individual group is separated by a gap of 10 ms. This is known as a muon fill. The time structure of this can be seen in Figure 4.2.

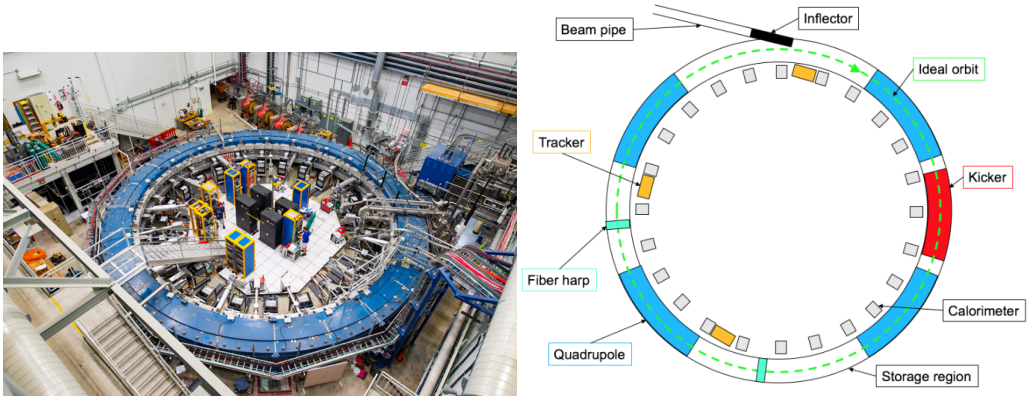

(a) (b)

Figure 4.1: The Muon g-2 experiment where (a) shows the constructed apparatus and (b) is a schematic representation of the storage ring showing the locations of the inflector, electrostatic quadrupoles, kicker magnets, tracking stations and fiber harps. The ideal central orbit is also shown.

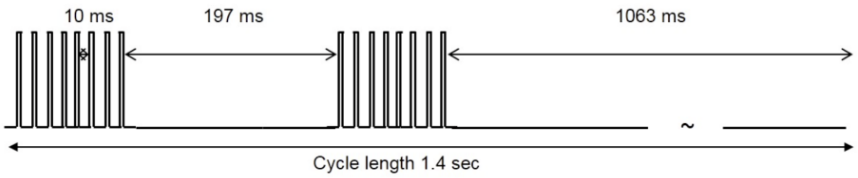

Figure 4.2: The time structure of a muon fill that is delivered to the Muon g-2 storage-ring per accelerator supercycle [7].

4.1 Injection of the muon beam

Due to the high precision demands of the Muon $g-2$ experiment, the storage ring is required to be a single continuous magnet designed to eliminate any edge effects that are present in lumped magnets. This constraint means that the muons must be injected into the storage ring yoke. To minimise the loss of muons that are deflected into the magnet itself on injection, a

superconducting inflector magnet shown in Figure 4.3 is used to eliminate the magnetic field in the injection tunnel.

This inflector is 1.7 m in length with an aperture that is 18 mm in width and 56 mm in height. The design of the inflector is an aluminium mandrel that is wrapped in superconducting coils in a truncated double cosine theta design [7]. The inflector is stored in a superconducting shield to contain the fringe field from the inflector so that the storage ring's magnetic field is unaffected. Windings at either end of the inflector, as shown in Figure 4.3, do cause a non-negligible loss of muons before injection.

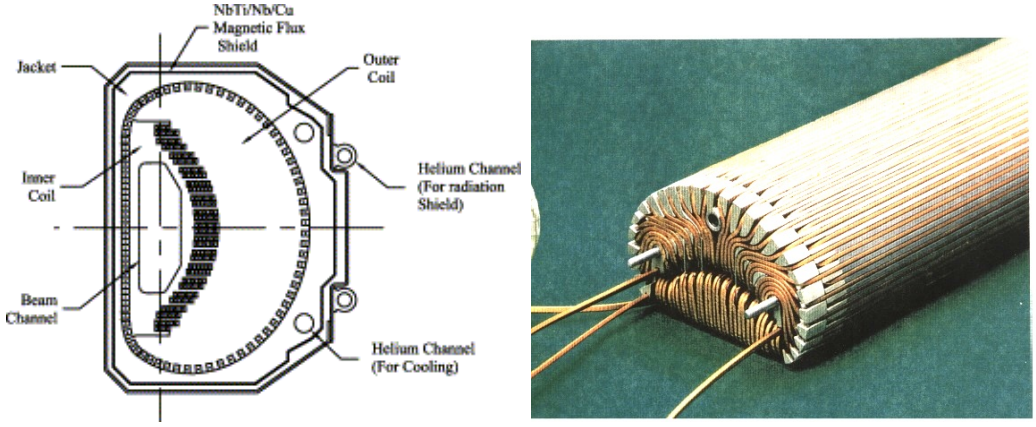

(a) (b)

Figure 4.3: The superconducting inflector magnet where (a) shows the cross-sectional schematic and (b) shows the windings at the end that cause muon losses.

The inflector cannot enter the storage ring as it would cause muon losses on collision on subsequent rotations of the storage ring and thus muons emerging from the inflector are not at the centre of the storage-region. To mitigate this, a so-called kicker magnet is employed to move the beam from the injection point orbit to a stable central orbit.

4.2 Kicker

For the kicker to move the orbit of the beam without causing any impact on the precision magnetic field of the storage magnet, it cannot contain any magnetic elements. Therefore, the kicker consists of two aluminium plates that are 1.27 cm in length with a separation of 10 cm. To not significantly perturb the magnetic field seen by the stored muons during the ω_a measurement period, the kicker has to switch off and lose all residual eddy currents within the 149.2 ns cyclotron period which also means that the muons aren't affected on subsequent rotations of the ring.

The deflection of the beam is designed to be approximately 10 mrad. This is achieved by using a vertical pulsed field of around 300 Gauss (which corresponds to kicker plate voltages of ≈ 160 kV), with a pulse length of ≈ 120 ns. The kicker consists of three separate kicker magnets located 90° from the inflector.

4.3 Muon beam dynamics

To precisely determine ω_a, the spatial and temporal distribution of the beam, referred to as the beam dynamics, needs to be fully understood. Due to the restoring forces provided by the B and E field from the electrostatic quadrupoles, the muons will undergo betatron motion both vertically and horizontally as they travel around the storage ring. The equations describing the vertical (y) and horizontal (x) motion are:

$$y = A_y(s)\cos\left(\nu_y \frac{s}{R_0} + \phi_y\right), \tag{4.1}$$

$$x = x_e + A_x(s)\cos\left(\nu_x \frac{s}{R_0} + \phi_x\right), \tag{4.2}$$

respectively. Here x_e is the equilibrium orbit radially relative to R_0, $A_y(s)$ and $A_x(s)$ are the amplitudes of the betatron motion and contain the discreteness from the quadrupoles where s is the trajectory arc length. The terms ν_x and ν_y are the ratios of the betatron frequencies, f^{BO}, compared with the cyclotron frequency, f_c. These are defined as

$$\nu_y = f_y^{\mathrm{BO}}/f_c = \sqrt{n}, \tag{4.3}$$

$$\nu_x = f_x^{\mathrm{BO}}/f_c = \sqrt{1-n}, \tag{4.4}$$

where n is the field index, which defines the strength of the electrostatic focusing in relation to B_0, which is the magnetic field strength of 1.45 T. This field-index is defined by the relation

$$n = \frac{\kappa R_0}{\beta B_0}, \tag{4.5}$$

where κ is the electric field gradient, R_0 is the stable orbit radius and β is the beam velocity. Lastly, the terms ϕ_y and ϕ_x contain the angular acceptance of the storage ring and are defined by the relations

$$\phi_{y_{\max}} = \frac{y_{\max}\sqrt{n}}{R_0}, \tag{4.6}$$

$$\phi_{x_{\max}} = \frac{x_{\max}\sqrt{1-n}}{R_0}, \tag{4.7}$$

where $x_{\max} = y_{\max} = 45\,\text{mm}$. The ν_i factors are chosen to ensure that the muons do not experience any resonances caused by perturbations around the ring as they pass through field gradients, as these resonances could cause the beam to expand significantly radially and/or vertically and cause a large loss of muons from the storage-ring. The condition to minimize these resonances is defined by the condition

$$a\nu_x + b\nu_y = c \tag{4.8}$$

where a, b, and c are integers. These terms are also constrained by the relation

$$\nu_x^2 + \nu_y^2 = 1. \tag{4.9}$$

Figure 4.4 shows the intersections of the resonances for certain values of n.

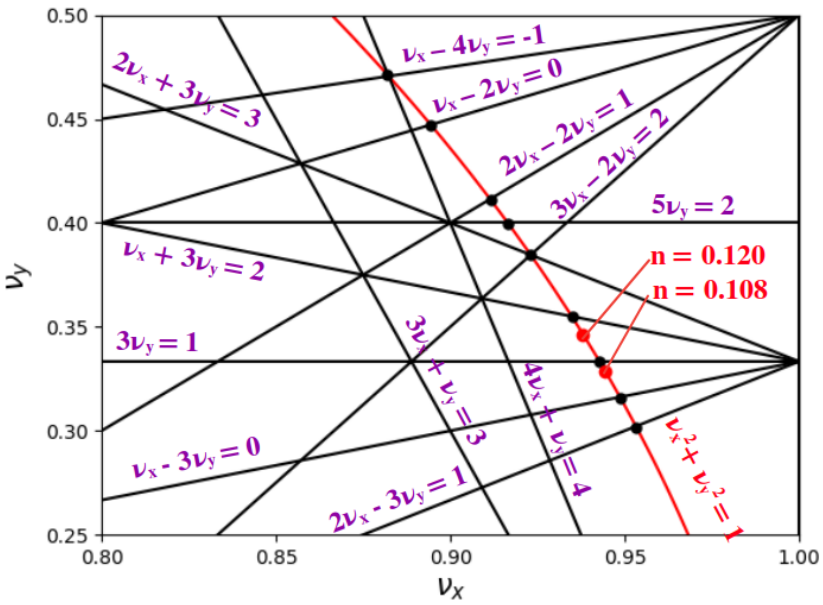

Figure 4.4: A schematic representation of the tune plane. The circle in red represents the constraint of $\nu_x^2 + \nu_y^2 = 1$, and the intersections with the black lines represent potential resonances [42].

The radial position of the beam dictates the fraction of events that result in a positron being detected. Due to the restoring forces of the magnetic field a simple harmonic motion effect is imposed on the beam, causing it to oscillate in and out radially. This betatron oscillation is dependent on the strength and phase of the kicker pulse as well as the spatial effects imposed by

the injection [42]. The detectors then measure the beam as a series of discrete pieces over time that depend on the azimuthal acceptances of the detector. This series of discrete pieces leads to each detector effectively sampling the beam at the cyclotron frequency ($f_c = 6.71\,\text{MHz}$); anything above the Nyquist frequency ($f_c/2$) will experience an aliasing effect (appearance of a false lower frequency signal). The radial betatron motion is defined by

$$f_x^{\text{BO}} = \sqrt{1-n} f_c, \tag{4.10}$$

and has a frequency of 6.31 MHz and, therefore, undergoes this aliasing and is seen by the detectors as a slow-moving oscillation. The measurable signal of this oscillation is referred to as the coherent betatron oscillation (CBO), which is defined by

$$f_{\text{CBO}} = f_c - f_x^{\text{BO}} = f_c(1 - \sqrt{1-n}). \tag{4.11}$$

A schematic representation of this phenomenon can be seen in Figure 4.5.

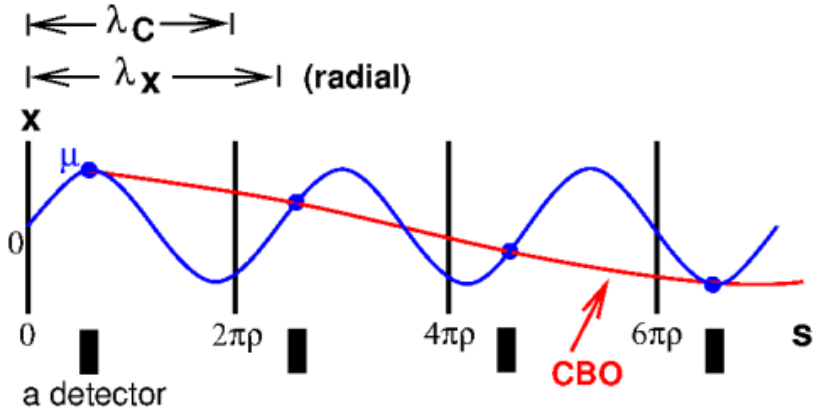

Figure 4.5: A schematic representation of the coherent betatron oscillation phenomenon. The black vertical lines are placed at the cyclotron wavelength; the blue line represents the radial betatron oscillation for three successive wavelengths. As the wavelength of the radial oscillation is larger than the cyclotron wavelength, the bunched beam can be seen to move closer to the detector (shown as a black box) and then further away. This CBO frequency is highlighted by the red line [7].

As well as a radial oscillation, the beam will also undergo an aliasing effect in the vertical dimension, referred to as the "vertical waist" (VW), which oscillates at twice the vertical betatron frequency. The reason the VW oscillates at twice the vertical betatron frequency is due to its dependence on the squared deviation of the muon beam. The VW is defined by

$$f_{\text{VW}} = f_c - 2f_y^{\text{BO}} = f_c(1 - \sqrt{n}). \tag{4.12}$$

4.4 Auxillary detectors

4.4.1 Inflector Beam Monitoring System

Essential to the Muon g-2 experiment is the Inflector Beam Monitoring System (IBMS). Due to the inflector aperture being extremely tight the incoming beam parameters are highly constrained. This means that a system is necessary to establish the beam's position as it passes through the inflector. The IBMS system is therefore essential to provide direct diagnostic information over the phase-space matching on the beam in the region between the last accelerator components and the inflection into the storage ring. This diagnostic control ensures the optimal number of stored muons per storage ring fill. This system is composed of two grids of scintillating fibre detectors.

The first detector is placed outside the storage magnet yoke before the injection point. The second detector is placed immediately downstream of the inflector. A third detector consisting of a single-plane of cylindrical scintillating fibres is placed downstream of the inflector. The detectors can be seen in Figure 4.6. These detectors provide both radial and vertical positions

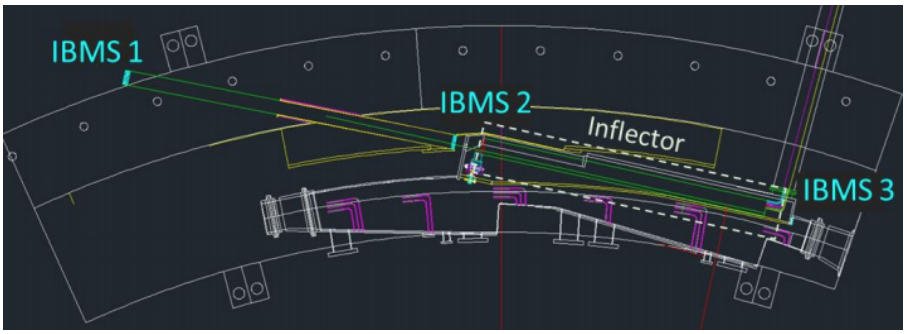

Figure 4.6: The positions of IBMS 1, 2, and 3 shown with respect to the vacuum chamber and inflector [7].

of the beam and are used to alert the accelerator operators when unexpected movements of the beam with respect to the optimal position are occurring. A full description of the IBMS system can be found in Ref. [43].

4.4.2 T0 start time detector

As well as the knowledge of the spatial distribution of the beam being necessary to the experiment, another essential property is the temporal distribution of the incoming beam. A T0 detector is used to measure this by setting a reference time for the beam bunch, which

allows the subsequent upstream detectors to be aligned and synchronised in time. This device consists of a central scintillator that is coupled to two photo-multiplier tubes (PMTs). The first PMT, known as PMT-A, acts primarily as the timing measurement of the beam and has a 1% neutral density filter, resulting in a low photo-electron statistics measurement. The second PMT, known as PMT-B, acts as a reflection of the intensity of the muon fill and has a 10% neutral density filter, resulting in a higher statistics measurement.

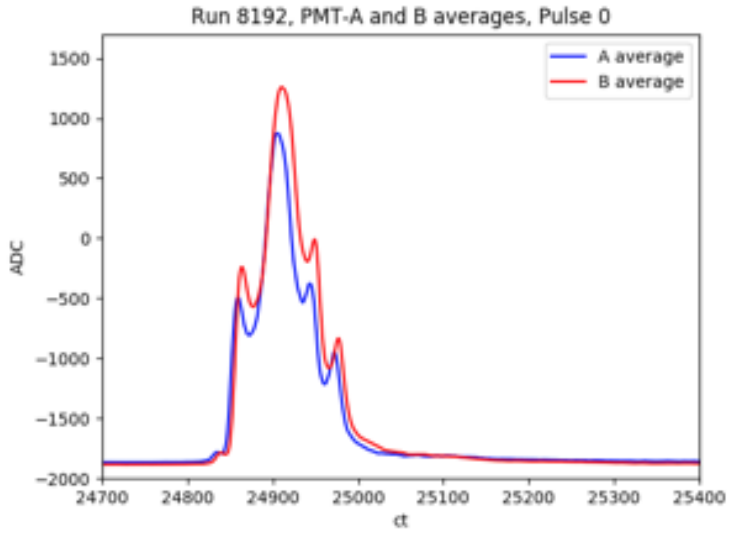

Figure 4.7: An example of the time profiles for the two PMTs in the T0 detector for one of the eight bunches. The x-axis is in clock ticks (ct), where 1 ct = 1.25 ns. These profiles are taken as an average of 100 separate time profiles [42].

4.4.3 Fiber harps

The final auxiliary detectors in the Muon g-2 experiment are the Fiber Harps. These detectors measure the beam profile as a function of time and azimuthal position within the storage ring. They primarily act as a diagnostic tool sensitive to beam effects as these detectors are destructive to the beam. They are only used for occasional dedicated studies when physics data is not being recorded. They consist of two pairs of detectors where one pair measures the horizontal beam properties, and the other pair measures the vertical beam properties. They are placed at 180°and 270°in the storage ring azimuth with respect to the upstream end of the inflector.

4.5 Electrostatic quadrupoles

As seen in Figure 4.1, there are four electrostatic quadrupoles that are designed to provide vertical focusing of the muon beam. These are chosen to be electrostatic rather than magnetic so as not to cause magnetic field gradients that would impact the precision of the measured magnetic field. The quadrupoles do however have defocusing in the horizontal plane and the net horizontal focusing comes from the main magnetic field. The quadrupoles consist of two segments. A short segment of 13° is 1.61 m in length, and a long segment of 26° is 2.62 m in length. Each of these segments consists of four plates and must be operated within a vacuum. The four-fold design is chosen to minimize the radial and vertical oscillations of the beam discussed in Section 4.3 and to improve the stability of the beam orbit. The electrostatic quadrupoles cover 43% of the total circumference of the storage ring.

4.6 Beam collimators and Scraping

To constrain muons to orbits within a region where the magnetic field is most uniform, collimators with a 45 mm radius are placed around the ring. Sometimes, muons will collide with these collimators and lose energy. This causes the muons to spiral inwards and, enter the detectors, and bias the measurement. To reduce such muon losses, the beam is scraped to create a 2 mm buffer region between the beam orbit and the collimators. This is performed by pulsing the quadrupole voltages in an asymmetric way to shift the beam vertically and horizontally to intersect the collimators. This scraping is performed early in the muon fill, so it is completed after 8 μs, and the beam is stable after 30 μs.

4.7 Calorimeter detectors

As the primary analysis of the Muon g-2 experiment is to measure the properties of the decay positrons from the muon beam, it is essential to use calorimeter detectors around the full azimuth of the storage ring. To achieve the high precision goal of the experiment, very stringent requirements for the calorimeter detectors must be met [44].

- The detectors must have an energy resolution of better than 5% at 2 GeV.
- The gain of the calorimeter must recover by 30 μs after the initial injection, thus recovering

from the beam flash.

- During the 30–700 μs measurement period the gain must remain stable.
- During the measurement period, the laser calibration system must be able to correct for residual gain instabilities to better than 4×10^{-4}.
- For positrons with an energy greater than 1.8 GeV, the time resolution should be better than 100 ps.
- To ensure less than a 10 ppb shift to ω_a, the system must maintain a time stability of less than 7 ps throughout any muon fill.
- If there are two electromagnetic showers with impact time separations greater than 5 ns, the system must be able to resolve them with 100% efficiency.

The gain of the calorimeter detector is dependent on the rate of incident hits and the stability of the temperature. It can be broken down into two components. The first component is the short-time double pulse effect (STDP). This effect occurs due to the detector pixels being unable to fire consecutively within a $\mathcal{O}$(ns) window. The second component is known as the in-fill gain effect. It occurs at $\mathcal{O}(\mu s)$ and is due to the high number of particles at the initial injection and the subsequent secondary particles within the detector recovery window. In the ω_a analysis for the calorimeter detector, both of these effects are corrected for.

To ensure the high precision goals of the experiment are met, 24 calorimeters are placed flush with the vacuum chamber wall of the storage ring. The calorimeters are placed on boards extending outwards to allow any magnetic powering and readout components to be placed away from the magnetic field region in order to not cause any perturbations. Each of the calorimeter detectors consists of 54 channels in a six high by nine wide array of PbF_2 crystals resulting in a total of 1296 crystals. Each crystal is wrapped in a black Teflar foil and has dimensions of $2.5 \times 2.5 \times 14.0\,\mathrm{cm}^2$. The design of the calorimeter detectors can be seen in Figure 4.8.

PbF_2 is chosen as the material for the calorimeter detectors due to its high density ($7.77\,\mathrm{g/cm}^3$), which results in a short radiation length of 9.3 mm. This short radiation length allows for ~ 100 energy depositions over the length of the crystal from the incident positrons. The second reason this material is chosen is due to its refractive index of 1.8, which allows it to emit Cherenkov light from incident positrons above an energy of 100 keV [7]. The Teflar foil improves the

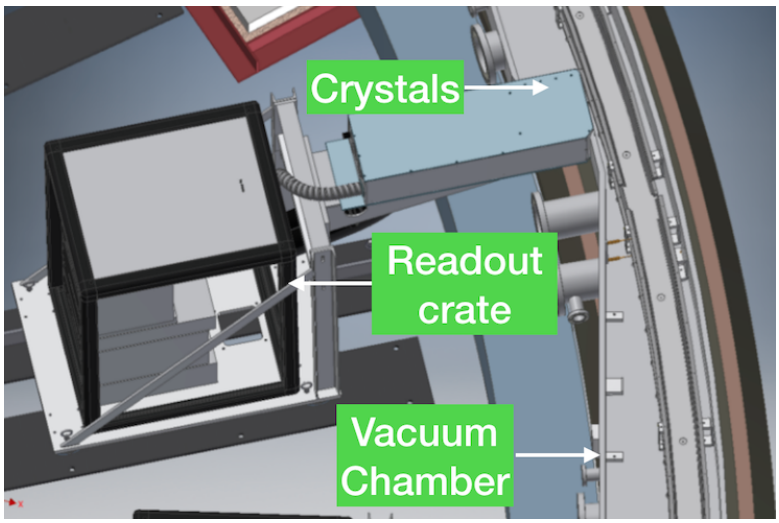

Figure 4.8: Schematic rendering of a calorimeter detector placed on the exterior of the storage ring [45].

spatial and temporal resolution as well as reducing internal reflections by ensuring minimal light interference between the crystals. Each crystal is connected to its own individual large-area silicon photomultiplier (SiPM), which allows the Cherenkov radiation emitted to be read out at high speeds. SiPMs are chosen because they are operable in regions with a high magnetic field; they have a high photo-detection efficiency, have a high degree of stability, and at MHz rates, they have a very linear response [7]. In order to preserve the fast pulse shape, the SiPMs are mounted on printed circuit boards (PCBs) that are devoid of any magnetic materials. This design can be seen in Figure 4.9. With this design, the detector achieves an energy resolution

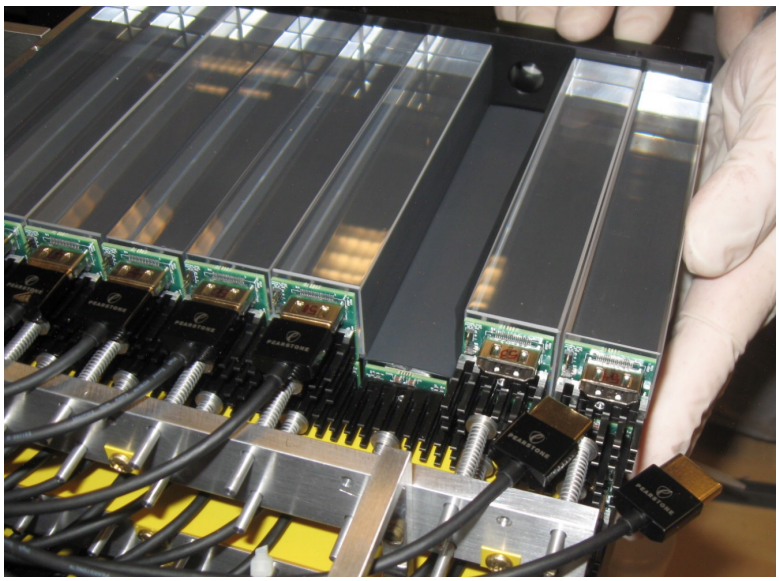

Figure 4.9: Design of the calorimeter detector highlighting the connection between the calorimeter crystal (clear bar) and the mounted SiPM [42].

at 2 GeV of 3.1%, and a timing resolution in a single channel for a 3 GeV positron of $\sim$ 40 ps.

Further details of the calorimeter characterisation are given in [44]. Waveform digitizers are then used to read out the information from the SiPMs at a rate of 800 GB/s and are transferred to a bank of GPUs for online-data processing.

Chapter 5

The straw tracker detectors

In the Muon g-2 experiment, the straw tracker detectors allow the muon beam distribution to be determined by measuring the positron trajectory and extrapolating back to the storage ring. The trackers are also used to determine the momentum distribution of the muon beam and perform a direct measurement of the pitch correction. An important, significant systematic effect in the calorimeter is the "pileup". Positron trajectories reconstructed in the straw tracker detectors can be extrapolated forward to the calorimeter to resolve this pileup. Pileup in the calorimeter occurs when two low-energy energy particles that are very close in time impact the same crystal and, therefore, are registered as a single $E > 1.8\,\mathrm{GeV}$ cluster in the calorimeter. The tracker identifies these as two separate low-momentum tracks and, therefore, can be used to resolve this effect. An independent determination of the magnitude of the pileup effect is an important aspect of the ω_a analysis.

5.1 Tracker geometry

The Muon g-2 tracker system consists of two separate stations placed at 180° and 270° around the storage ring and are referred to as Station 12 and 18, respectively. Each station consists of eight modules placed in a staircase orientation to follow the curvature of the ring as shown in Figure 5.1. Each module consists of two planes rotated at $\pm 7.5\,^{\circ}$ to allow for the tracker to be viewed in two separate orientations referred to as U and V. This can be seen in Figure 5.2.

Each plane consists of two layers of straws separated by an offset of 1 mm, with each layer consisting of 32 straws. Each straw has a fiducial length of $\sim$ 8.5 cm and a radius of $\sim$ 2.5 mm

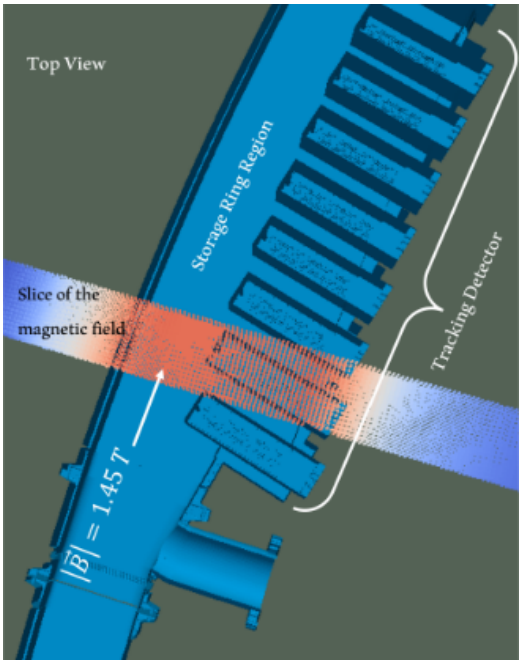

Figure 5.1: Diagram showing the module orientation within a tracker station. The coloured band represents the varying magnetic field, with the detector positioned in both the uniform and fringe regions of the field [46].

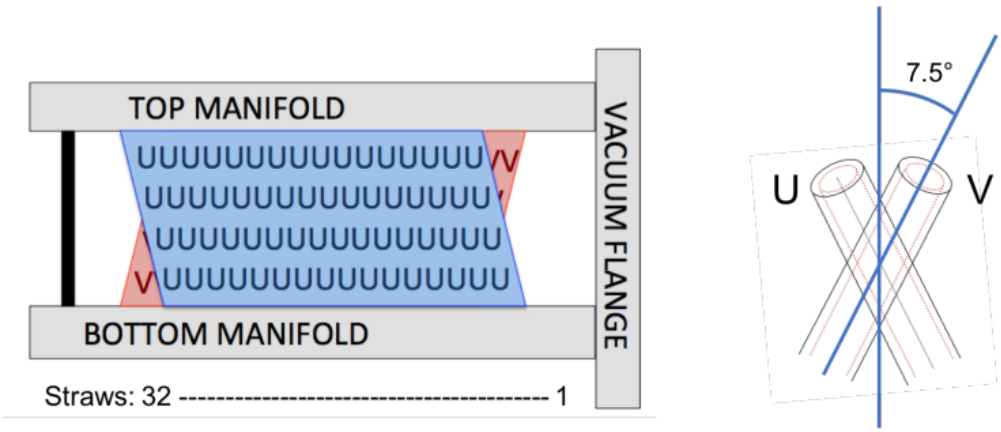

Figure 5.2: Diagram showing the U and V orientations of the planes within a straw tracker station module [42].

constructed from aluminized Mylar and filled with 50:50 Argon:Ethane gas.
The geometry in the software is defined in a 3D Euclidean geometry with six degrees of freedom based on the position and the Euler angles. This is shown in Figure 5.3.

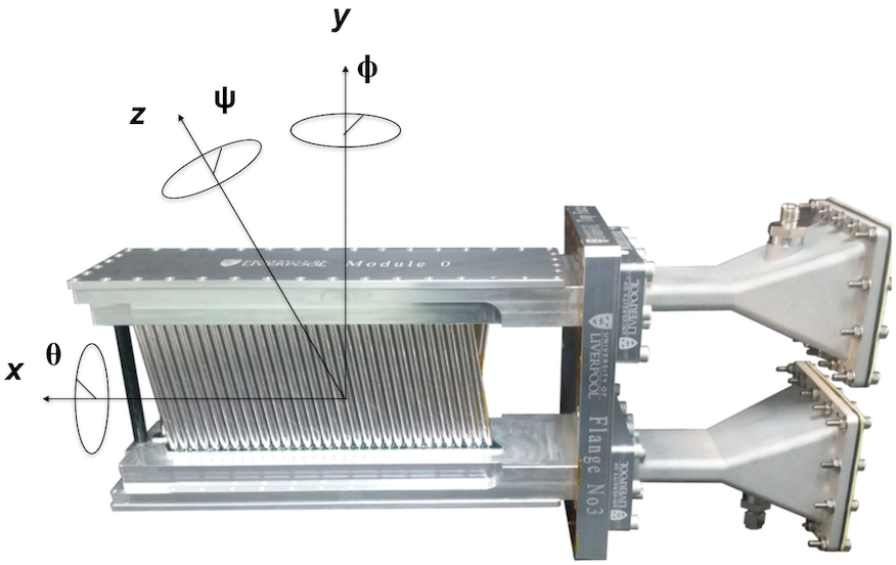

Figure 5.3: The coordinate system for the tracking detector in the software relative to a single tracking detector module [47].

5.2 Digitisation

At the centre of each straw is a 25 μm gold-plated tungsten sense wire on which a current can be induced. This current is caused when fast-moving charged particles, e.g., positrons ionize the gas as they pass through the straw. The liberated electrons are then drawn to the wire and the ions to the straw surfaces. As the electrons approach close to the wire they are subject to a large E-field and accelerated which produces significant further ionisations (avalanche effect) and a large amplification in the signal making it measurable.

The time of this signal relative to when the primary charged particle passed through the straw is defined as the drift time of the particle and is used to determine the position the charged particle traversed the straw. This signal is referred to as a "hit". By combining this information for each straw, the particle trajectory can be reconstructed as a "track". The angular information of the trajectory of the particle within the straws also allows for a determination of the momentum of the particle, and it allows extrapolation back to the point of decay of the muon.

5.2.1 Readout electronics

To allow the signals from the positron trajectories, the clock signals and control signals to the straw tracker detector to be recorded, a hierarchical system of front-end boards and back-end boards is used. An overview of the path of the signals through the read-out system can be seen in Figure 5.4. The hierarchical structure of the read-out system can be seen in Figure 5.5

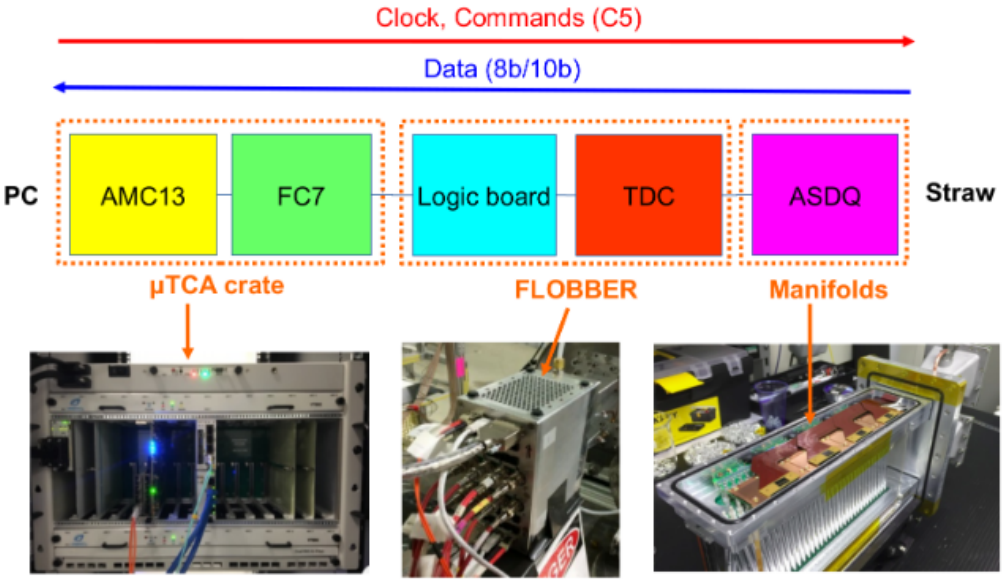

Figure 5.4: The signal path of the clock signals and straw hit data to the PC for the read-out electronics system with the physical location represented [48].

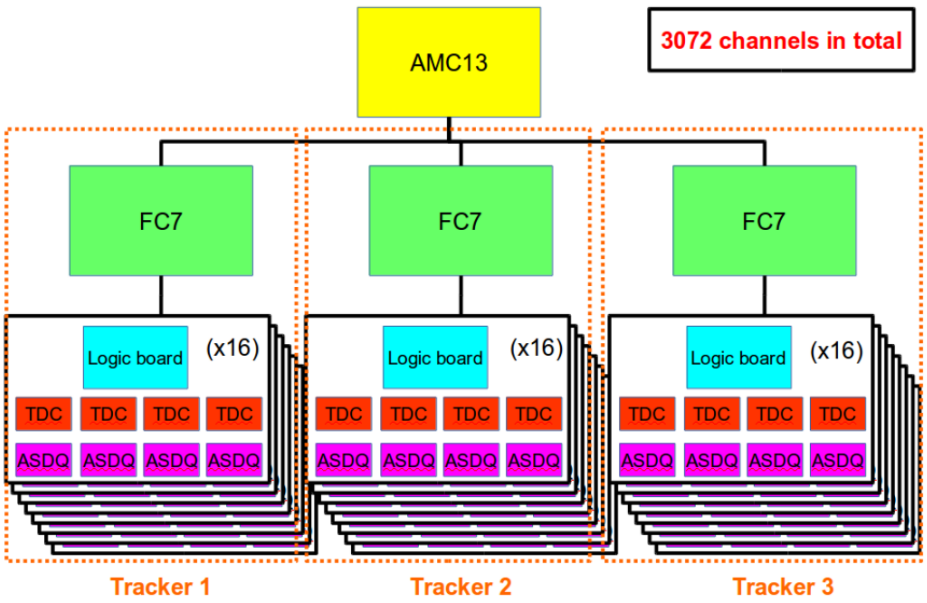

Figure 5.5: The hierarchical structure of the electronics read-out system with the number of each specific board used [48].

Front-end electronics

The front-end system is the first level in the hierarchical system. It refers to the boards that are used to measure the signal from the sense wires in each straw and then record these signals as hits. This sub-system consists of two distinct boards. The first board is the Amplifier Shaper Discriminator with charge (Q) encoding (ASDQ) board, which is the closest to the straws, and the second board is the Time to Digital Converter (TDC) board.

The ASDQs are mounted directly onto the end of the straw sense wires and are used to record when a charged particle has traversed the straw, and it is triggered when the induced signal on the sense wire crosses a set threshold. These signals are known as straw hits. The ASDQ boards also provide the sense wires with High Voltage (HV) power.

The processing of the signal within the ASDQ is split into separate steps that are optimised for efficiency, timing resolution and the ratio of signal-to-noise. In the first step, the signal from the sense-wire is amplified and then shaped to remove short time-scale features such as spikes in the signal. This allows the short signals from all of the primary ionisation events to be integrated into a single pulse. As the drift of the ions is slower than that of the positrons, this gives the signal a characteristic long tail.

Baseline restoration is used in the shaping of the signal to correct for this tail to mitigate overlapping of the ion and the positron signals, thus allowing the primary ionisation event to be read out at much higher rates. A discriminator with a configurable threshold is then used to register when the pulse crosses said threshold. This threshold defines the leading and trailing edges of the recorded pulse and is then output as a digitised signal. Only the transitions at the leading and trailing edges are output in the digitised signal.

This signal is then transported to a custom rack outside the tracker module and storage ring vacuum region known as the Front-end Low-voltage Optical Box to BackEnd Read-out (FLOBBER), which houses the TDC as shown in Figure 5.6.

Each tracker module is mounted with a separate FLOBBER. The TDC is connected to the 40 MHz experiment clock and is used to time stamp each transition at an accuracy of 625 ps. Each transition is output to the data stream as a 'hit-word', which encodes the transition time, the hit channel, and whether the edge of the transition is leading or trailing. The leading-edge hit-words are considered as the hit time in a straw. The TDCs are paired one-to-one with the ASDQ boards with 16 channels, each connected to a single straw. As each straw tracker module contains 128 straws, and each module requires 8 TDC-ASDQ pairs.

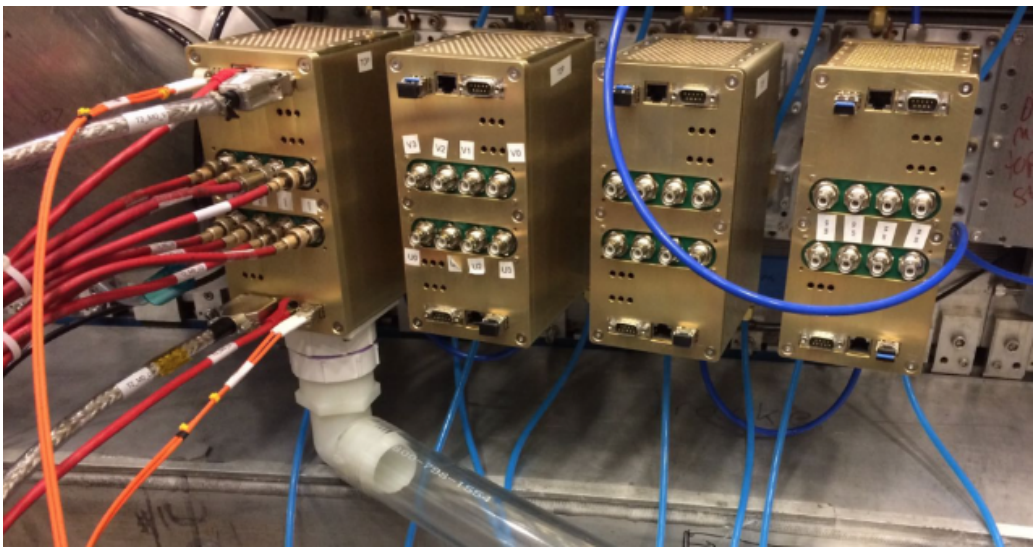

Figure 5.6: Four FLOBBER boxes outside of the vacuum region that house the TDCs, HV boards and Logic Boards.

Back-end electronics

The back-end electronics comprises a system of Logic Boards (LBs), FC7s and a single micro-TCA crate (μ-TCA). For the module, there are two LBs that are each used to interface with four ASDQ-TDC pairs. The LBs have two functions; the first is to provide the TDCs with the clock and control signals, and the second is to collect the data into a single block where it is processed downstream. For each straw tracker station, there is one FC7 advanced mezzanine card (AMC), which is connected to sixteen LBs. The FC7 collects the data from all of the LBs into a single block.

The most downstream component of the back-end electronics is the AMC13, which collects the data from the FC7 boards into a single block and also sends control and clock signals to the FC7s which distribute these signals to the LBs. The FC7 and AMC13 are housed within the *mu*-TCA crate. A more detailed overview of the full Muon g-2 read-out system can be found in [48].

5.2.2 Hit determination

The digitisation of the analog signal on the sense-wire results in a drift-time being assigned which is a proxy for the distance from the sense-wire that the original charged particle passed. However it is not known a priori which side of the sense-wire the particle passed and instead a drift-circle is assigned. The radius of this drift circle is the distance of closest approach (DCA) of the charged particle to the wire. A schematic representation of this drift circle and DCA can

be seen in Figure 5.7.

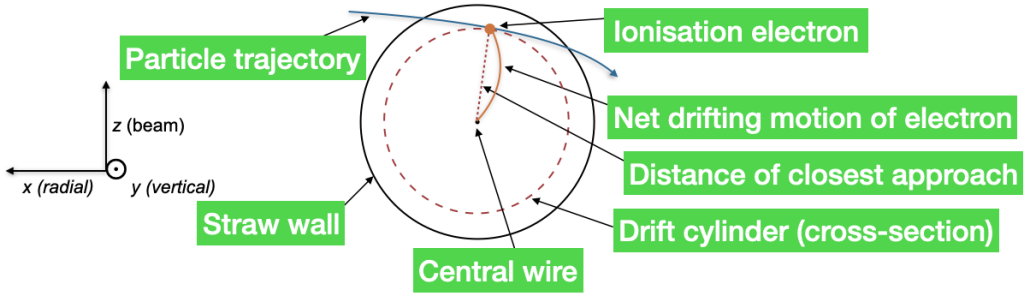

Figure 5.7: Schematic representation of an ionising particles passing through a straw with the the drift circle and DCA highlighted [47].

The conversion between drift-time and DCA comes from an iterative procedure of assigning a time-to-distance calibration (informed by simulation) to the data and minimising the hit χ^2 with respect to the track trajectory. This time-distance relationship is shown in Figure 5.8.

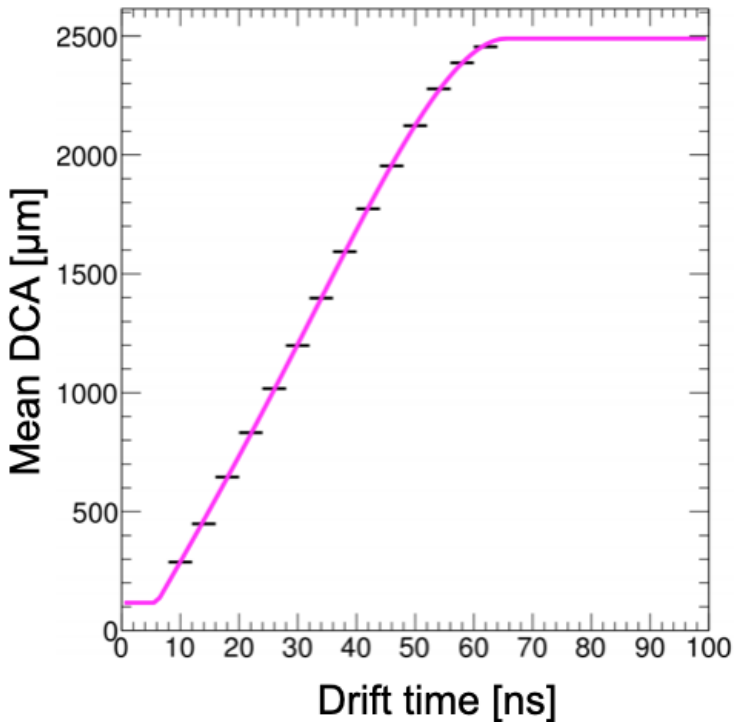

Figure 5.8: The time-distance calibration that converts a measured drift-time to a DCA [49].

5.3 Track reconstruction

For reconstructing the charged particle's trajectory, known as track reconstruction, there are several routines and algorithms. The full tracking reconstruction algorithm can be seen in Figure 5.9.

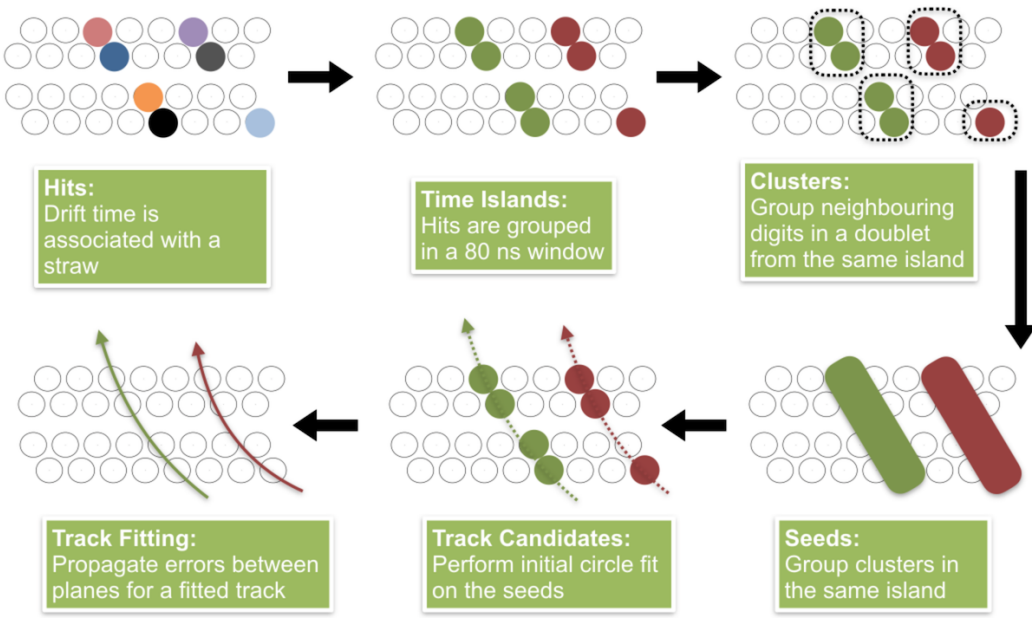

Figure 5.9: Schematic representation of the full track reconstruction routine [46].

Once the hits have been grouped into track candidates, there are several constraints before they are passed on to the track fitting. If multiple candidates contain the same seeds, clusters, or hits, they are removed. If the tracks contain less than six hits or they only contain seeds of one UV orientation, they are also removed. The Geometry and Error propagation (`GEANE`) routine [50] for error propagation within a `GEANT4` [51] framework (for the geometry and physics processes) is used for track fitting. `GEANE` is used to accommodate the large magnetic-field gradients over the straw tracker detectors. The more accurate the reconstruction is, the smaller the residuals between the fitted track and the DCA in each wire are. The design goal for the track reconstruction was to achieve a resolution on the DCA of 240 μm. The developed framework achieved a resolution of 120–150 μm [52].

5.3.1 Left-Right ambiguity

When a track is reconstructed it is important to determine which side of the straw the particle's trajectory was relative to the central sense wire. This allows for a better determination of the angle of incidence of the particle as well as the time it entered the tracking detector, t_0. On track reconstruction, each hit is assigned an LR-index, 'L' being if the hit was on the left side of the sense wire and 'R' if the hit was on the right side of the sense wire. Hits that are registered too close to the centre of the wire can smear the LR distribution. If the LR-index is incorrect for even one hit in the track then the fit will likely fail. Algorithms have been implemented to deal with this ambiguity in the LR assignment [53].

5.3.2 Track extrapolation

Once the tracks are formed and fitted, they can also be extrapolated back to the most likely point of decay of the muon, or they can be extrapolated forwards to energy deposits in the calorimeter crystal, allowing for particle identification, as well as a measure of the efficiency of the straw tracker detectors. The extrapolation algorithm utilizes a Runge-Kutta Nystrom algorithm of the fourth order [54]. This algorithm performs a propagation through the varying magnetic field in the full `GEANT4` simulation to reach a point of tangency where the radial momentum is zero and then applies a small $\mathcal{O}(1\,\mathrm{mm})$ radial correction so that the muon decay point is reliably determined. This can be seen in Figure 5.10. This backward extrapolation

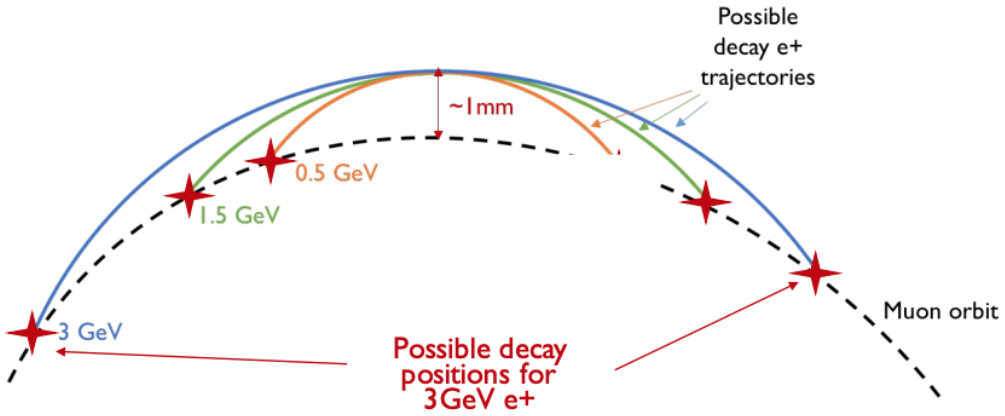

Figure 5.10: Schematic representation of the backward extrapolation of the track to the muon decay point. Due to the higher momentum tracks travelling further to reach radial tangency compared with the lower momentum tracks, a $\mathcal{O}(1\,\mathrm{mm})$ offset is applied.

allows an accurate determination of the beam profile. The extrapolated beam distribution can be seen in Figure 5.11.

5.3.3 Quality requirements

To reduce uncertainties in the measurements with the tracking detector, data quality requirements have to be applied to remove any poorly fitted tracks or tracks that failed to fit. The full list of the conservative requirements that are applied is broken down into three levels: requirements on the candidate level, requirements on the track level, and requirements on the forward extrapolated vertices. Each subsequent level maintains the requirements from the previous levels. These requirements [55, 56] are defined in Table 5.1

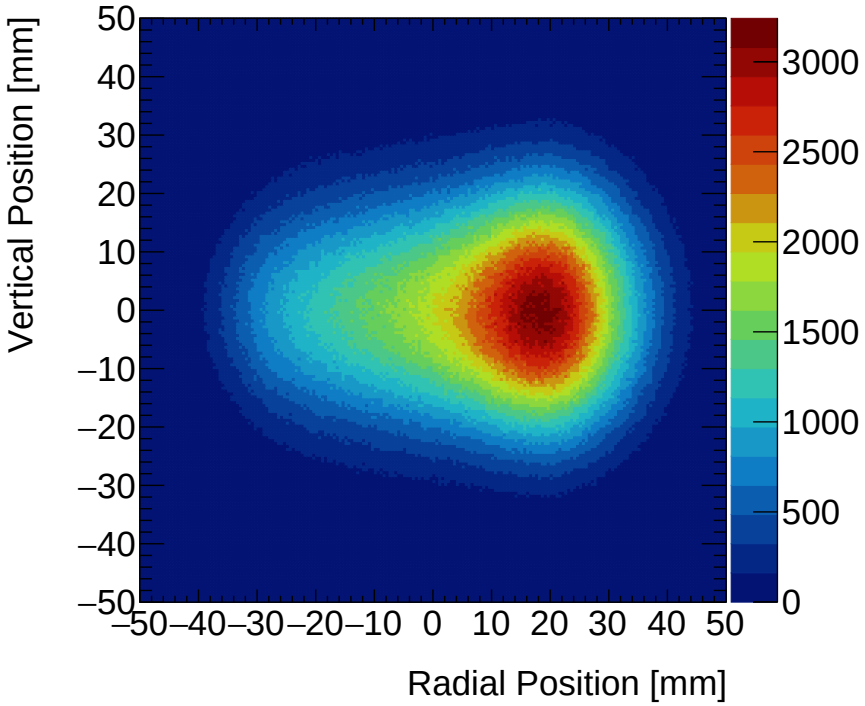

Figure 5.11: The extrapolated beam profile from reconstructed tracks [54].

Candidates
Number of straw hits ≥ 12
Number of $\lvert U - V \rvert$ hits ≤ 4
Fraction of missed layers $< 30\%$
Drift time: $0 < t_d < 70$
Tracks
Track fit p-value $> 5\,\%$
Track residuals $<500\,\mu$m
Track entrance point: $60 < x < 150\,$mm $\quad -40 < y < 40\,$mm
Vertices
No external volumes hit
Vertex vertical and radial uncertainties: $1.0 < \sigma_y < 6.0\,$mm and $1.0 < \sigma_r < 6.0\,$mm

Table 5.1: Data quality requirements for each level of track reconstruction.

5.4 Internal alignment

Essential for high-precision studies using the Muon g-2 straw tracker detectors is the minimization of the uncertainty on the extrapolated beam position. This requires a high-precision alignment of the detectors. The importance of this can be seen in Figure 5.12, which highlights the effect on the extrapolated beam position by differing degrees of internal misalignment.

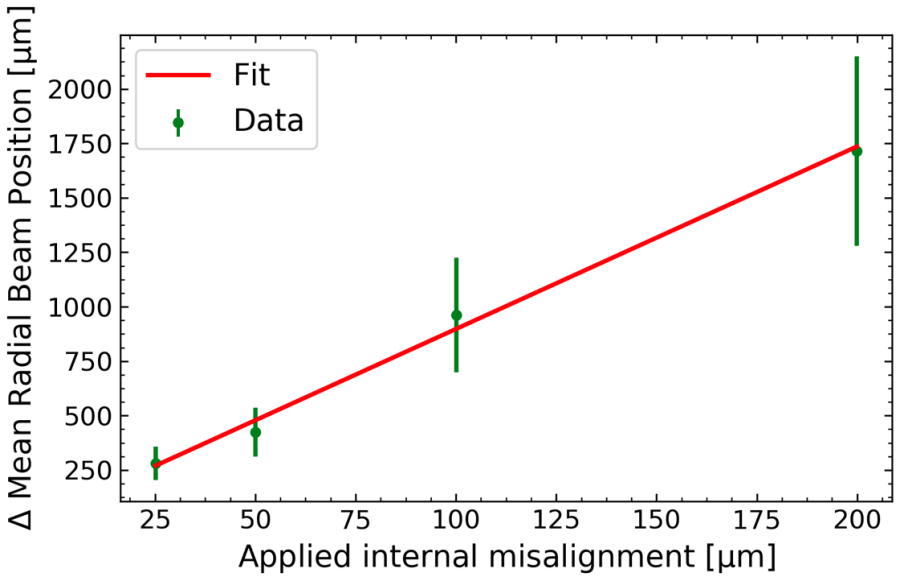

Figure 5.12: The change in the extrapolated radial beam position relative to a randomized internal misalignment for four tracking detector modules at varying degrees of misalignment [47].

A large internal misalignment will produce significant residuals between hit positions and the fitted track. If alignment corrections are applied to the tracking algorithm before the tracks are fitted, then these residuals can be diminished. To perform the internal alignment for the Muon g-2 experiment straw tracker detectors, the `Millepede-II` framework [57], commonly used in particle physics, was used. An in-depth study of the alignment using this framework was performed for the Run-1 dataset in [47].

The `Millepede-II` framework performs a least-squared regression (LGR) based on two groups of parameters. The first group is the global parameters that affect all the tracks, for example, the geometry parameters and established alignment parameters. The second group is local parameters that are specific to each of the fitted tracks. The framework uses both these groups to minimize a linear function based on the sum of the residuals. These residuals can be defined by the difference between a measured hit position and a predicted hit position. This function

can be defined based on a χ^2 minimization as

$$F(\boldsymbol{a},\boldsymbol{b}) = \frac{\partial\chi^2(\boldsymbol{a},\boldsymbol{b})}{\partial(\boldsymbol{a},\boldsymbol{b})} = \sum_{j}^{\text{tracks hits}} \sum_{i} \frac{1}{(\sigma_{i,j})^2} \frac{\left(r_{i,j}\left(\boldsymbol{a_0},\boldsymbol{b_{0,j}}\right) + \frac{\partial r_{i,j}}{\partial a}\delta\boldsymbol{a} + \frac{\partial r_{i,j}}{\partial \boldsymbol{b}_j}\delta\boldsymbol{b}_j\right)^2}{\partial(\boldsymbol{a},\boldsymbol{b})} = 0, \quad (5.1)$$

where a are the global parameters, b_j the local parameters, $r(a, b_j)$ is the defined residual hit, a_0 and $b_{0,j}$ are the initial parameters, $\sigma_{(i,j)}$ is the estimated uncertainty on the measurement, summed over the tracks and the measured hits. The correction factor to the global parameters, δ_a, is then added to the tracking algorithm, and the alignment is then performed iteratively until the results converge. This correction factor is defined by six degrees of freedom based on the rotations and positional translations of the tracking detector in a 3D Euclidean geometry and is defined as

$$\delta\boldsymbol{a} = \begin{pmatrix} \delta x \\ \delta y \\ \delta z \\ \delta\theta \\ \delta\phi \\ \delta\psi \end{pmatrix}, \quad (5.2)$$

where θ, ϕ and ψ are the Euler angles. These degrees of freedom relative to the tracking module are shown in Figure 5.3.

Figure 5.12 shows that a small misalignment can affect the beam position to a large degree. Therefore, the systematic uncertainty on the beam position due to misalignment needs to be evaluated. Constants were derived and checked for each run period and when changes were made to the straw tracker detectors. These constants are stored in a SQL database. Each straw tracker station has eight modules, and each module has a constant for both the radial and vertical positions. To estimate the systematic uncertainty on the beam position from the internal alignment, a random, uniformly distributed offset for each constant within $\pm 10\,\mu$m is applied, and the data is re-tracked with the newly derived constants and the beam positions are re-evaluated.

This was repeated ten times and the variance from these ten evaluations for both the mean and RMS of the beam positions was taken for the systematic uncertainty. The results can be seen in Figures 5.13 and 5.14.

The systematic uncertainties were calculated for two runs in Run-2 (24577 and 25896) and one run in Run-3 (34750), and the final values can be seen in Table 5.2. Runs 24577 and 25896

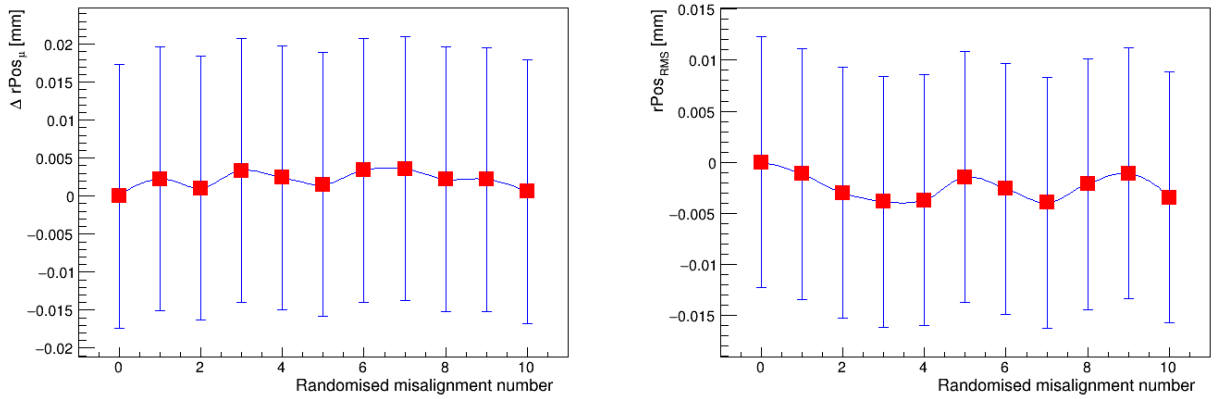

(a) (b)

Figure 5.13: The change in the (a) mean and (b) RMS radial extrapolated beam position as the alignment is changed within its known uncertainty with the associated RMS of each point shown.

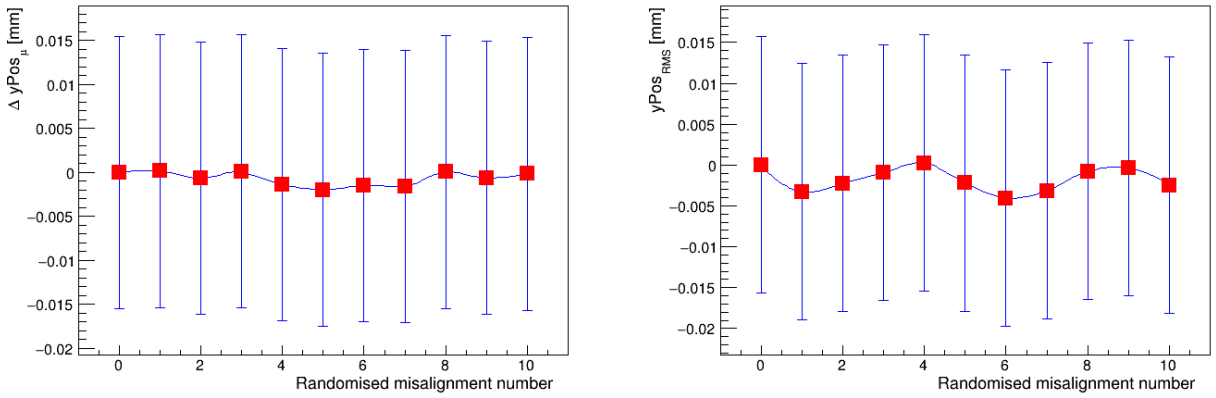

(a) (b)

Figure 5.14: The change in the (a) mean and (b) RMS vertical extrapolated beam position as the alignment is changed within its known uncertainty with the associated RMS of each point shown.

were before and after a tracker module was replaced, respectively, and the alignment constants were re-derived.

Tracker Station	$\Delta\mu$R[μm]	$\Delta\sigma$R[μm]	$\Delta\mu$Y[μm]	$\Delta\sigma$Y[μm]
24577				
Station-12	1.36 ± 0.99	-3.01 ± 1.17	-0.99 ± 0.66	-1.51 ± 1.15
Station-18	-3.83 ± 1.55	1.77 ± 0.78	-2.37 ± 1.02	1.12 ± 1.24
25895				
Station-12	5.13 ± 1.79	-3.83 ± 1.42	-1.13 ± 0.49	-1.16 ± 0.63
Station-18	-0.91 ± 0.76	-1.22 ± 0.79	0.28 ± 0.48	-3.86 ± 1.51
34750				
Station-12	-6.23 ± 2.12	-1.14 ± 0.62	2.05 ± 0.86	-1.17 ± 0.79
Station-18	-6.12 ± 2.15	-3.72 ± 1.13	0.27 ± 0.62	-5.13 ± 1.90

Table 5.2: Shifts in the mean radial ($\Delta\mu$R), vertical ($\Delta\mu$Y) beam position and RMS ($\Delta\sigma$R, $\Delta\sigma$Y) in Run-2 and Run-3 for the two straw tracker stations due to tracker misalignment.

Chapter 6

t0 algorithm improvements

In track reconstruction, the t_0 of the track is defined as the time at which the particle first enters the tracking station. A better resolution of the t_0, improves the resolution on the DCA of the signal in each straw hit. The increase in resolution allows a better track fit and, therefore, allows more tracks to be reconstructed. As the straw tracker data is statistically limited compared to the calorimeter and is necessary for studies of the beam position and an independent ω_a analysis, improving the track reconstruction efficiency is paramount. Each reconstructed track can be broken down into hits, which are then grouped into time-islands as previously shown in Figure 5.9.

From these time islands, hits are then clustered into clusters of two types: singlets and doublets. Singlets are instances in which only one hit is measured per plane, and doublets are instances in which two hits are measured per plane. This can be seen in Figure 6.1. Before the new

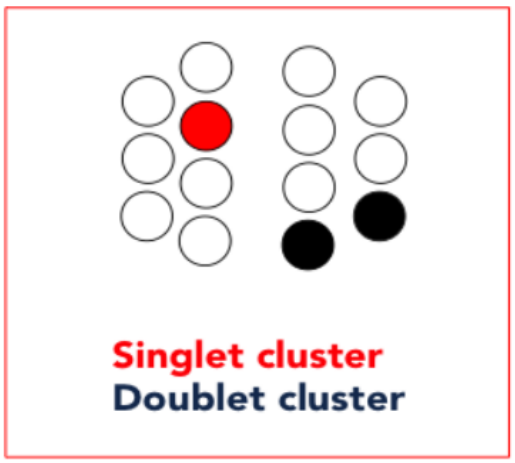

Figure 6.1: Schematic representation of the two spatial cluster types: a singlet (one hit per plane) and doublet (two hits per plane) [46].

algorithm defined in this chapter was developed, the algorithm to calculate the t_0 for the track

was expressed in the form

$$t_0 = \frac{\Sigma t_c}{N} - k_{MT}, \tag{6.1}$$

where Σt_c is the sum of the hit times in the reconstructed track, N is the number of hits per track, and k_{MT} is a constant mean-time offset correction found from the difference between the average difference in time between the tagged calorimeter hits and the track hits corrected for the time of flight. This is a simple approximation that weights all hits in the track equally by their time and does not account for any spatial information.

In this chapter, a new algorithm will be described that allows for a better determination of the track t_0 using the angular information of the hits. The approach will be iterative and will first define the relationship between the LR-ambiguity of doublets in each track and will then define a linear relationship between the tangent angle of each hit in a circle fit to the track and then will derive a further correction in the non-linear region.

6.1 New t_0 algorithm

The spatial information of the doublet clusters shown in Figure 6.1 can be used to define the relationship between the angle of incidence of the track and the drift time. The drift time can be seen in Figure 6.2.

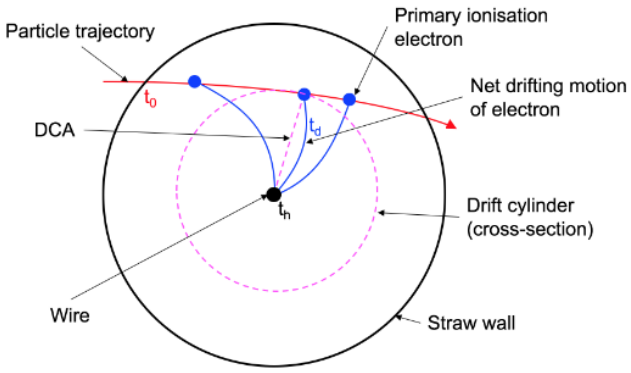

Figure 6.2: Schematic representation of a charged particle trajectory through a straw showing the drift time t_d and the DCA (distance of closest approach).

The angle of incidence with respect to the horizontal plane is given by

$$\theta = \arctan\left(\frac{p_x}{p_z}\right), \tag{6.2}$$

where p_x and p_z represent the components of momentum for the particle in the x and z plane

respectively. This angle can be used to resolve the left-right ambiguity (defined in Section 5.3.1). Each doublet of hits is assigned a combined LR-index e.g. LL is when the first and second hit of the doublet are on the left side of both wires as in the lower two hits in Figure 6.3.

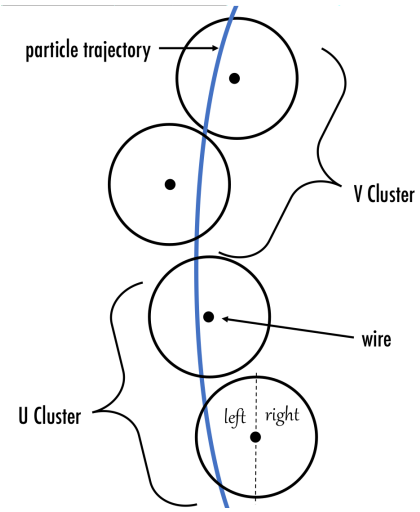

Figure 6.3: Schematic representation of a tracked trajectory showing hits that pass both to the left and right of the wire [46].

In the region $55 < t < 105\,\text{ns}$ there is a linear relationship between θ and the sum of the drift times in the doublet, t_{ds} (see Figure 6.5). The drift time sum can then be evaluated using the linear fit parameters (P_0, P_1) and the angular incidence as

$$t_{dse} = \frac{(\theta - P_1)}{P_0}, \tag{6.3}$$

where t_{dse} represents the new estimate. Using this and the times of the hits, an estimate for the t_0 of the track can be made using:

$$t_0 = \frac{(\Sigma t_{cd} - t_{dse})}{2}. \tag{6.4}$$

where Σt_{cd} is the sum of the hit times in the doublet.

The new algorithm was then compared against the old algorithm using tracks that had passed quality requirements (see Table 5.1) and which were matched to calorimeter clusters. The difference, Δt, between the time measured by the calorimeter and the time measured by the tracker with a time of flight correction was then determined. The results of this algorithm can be seen in Figure 6.6. It was found that the standard deviation in Δt across a single run for the old algorithm is $\sigma = 1.760 \pm 0.005\,\text{ns}$ and for the new algorithm is $\sigma = 0.880 \pm 0.004\,\text{ns}$. With a $\sim 50\mu\text{m/ns}$ drift velocity this reduces the contribution to the DCA resolution from the

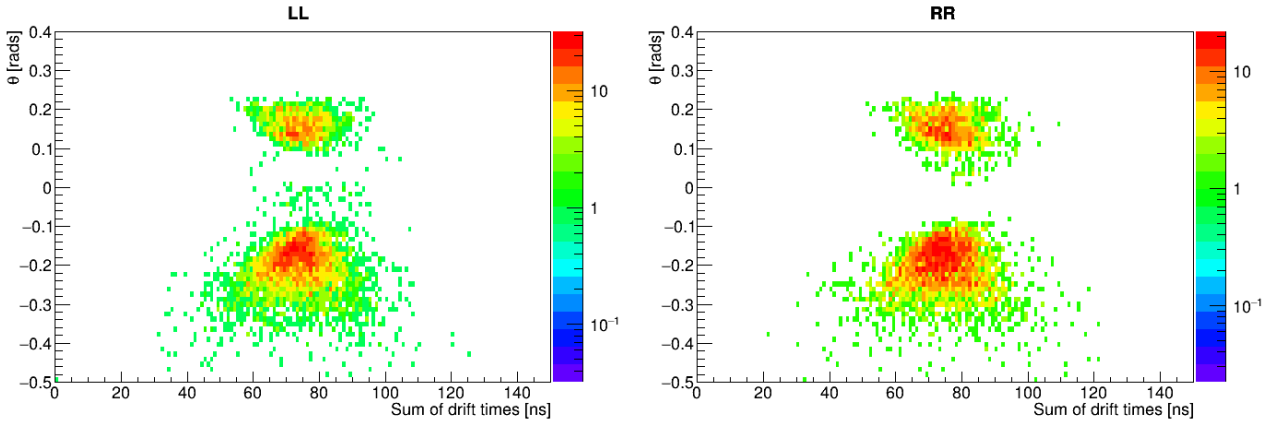

(a)

(b)

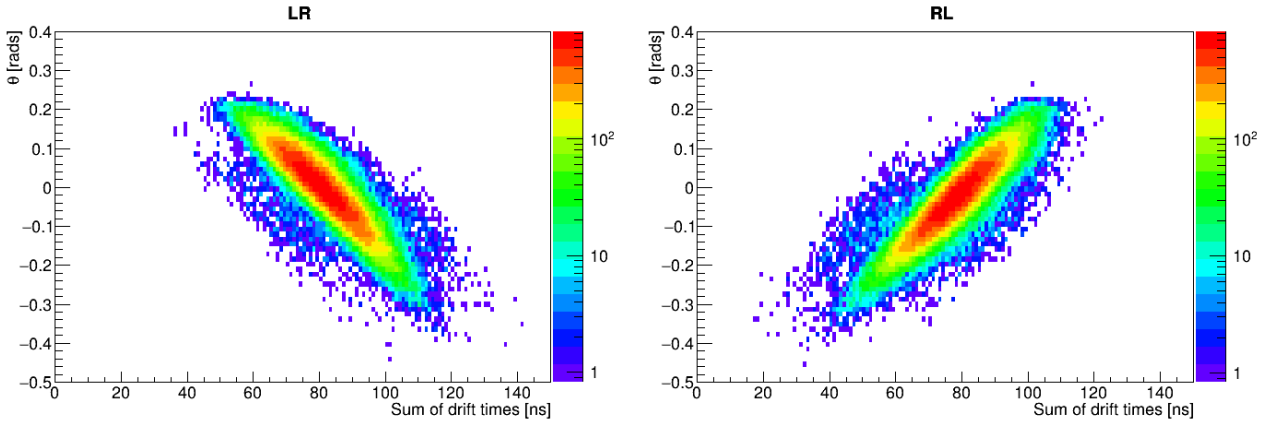

(c) (d)

Figure 6.4: Angle of incidence versus the sum of drift times for each possible LR-index of a hit doublet.

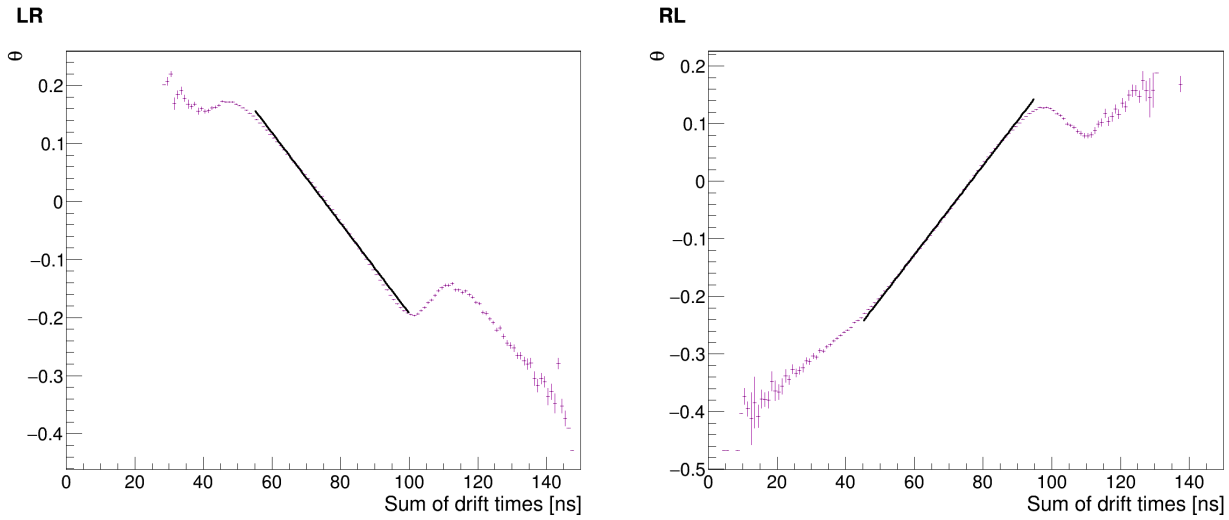

(a) (b)

Figure 6.5: Profile plot of angle of incidence versus sum of drift times for (a) LR and (b) RL cases. The region $55 < t < 105\,\text{ns}$ is reasonably described by a straight line.

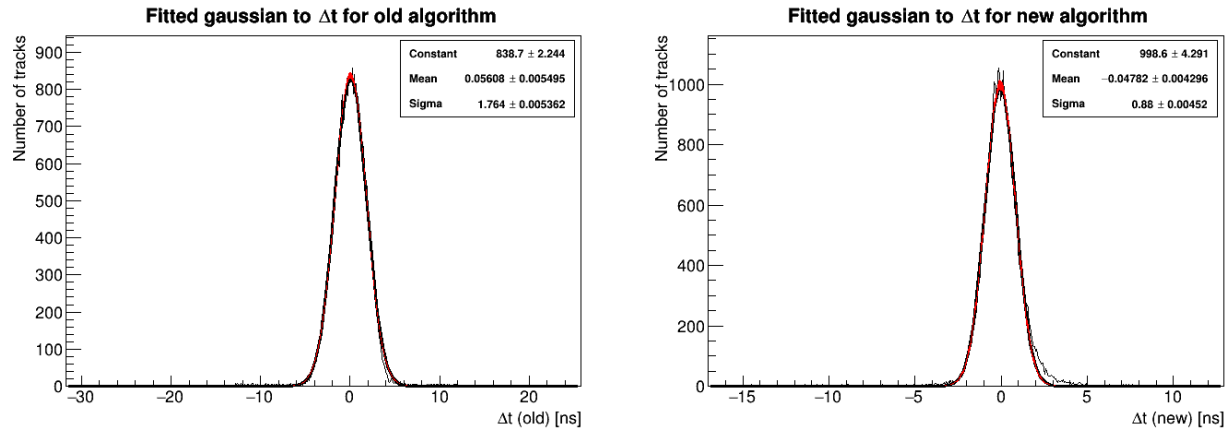

(a) (b)

Figure 6.6: A comparison of the t_0 determined from tracks with ((a): the old algorithm and (b): the new algorithm that uses the angular dependence and LR ambiguity from the fitted track referenced with respect to the time of the extrapolated track in the calorimeter after removing a fixed time-of-flight offset.

t_0 from $88.2\,\mu$m to $44.2\,\mu$m, which is a significant improvement.

This determination of the t_0 relies on knowing the momentum vector of the fitted track. Therefore, it cannot be used prior to the track fit and hence a method to determine θ prior to the full track fit is required. A simple circle-fit, as illustrated in Figure 6.7, has instead been developed to determine θ. With some algebraic manipulation, and by taking the tangent to the circle, it is possible to find the angle of incidence from

$$\theta_c = \arctan\left(-\frac{1}{m_r}\right), \tag{6.5}$$

where m_r is the tangent of the radius from the centre of the circle fit to a point (x, y) on the circle. Using this, we can then perform the calculation as before with this value for θ instead of the one that relies on the momentum from the track fit.

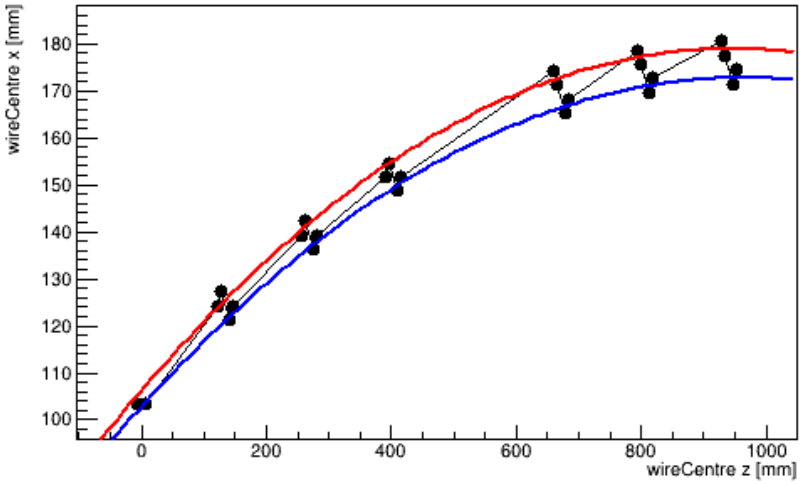

Figure 6.7: Example of a circle-fit to real tracker data where the red line represents the circle fit to the U-plane and, the blue line represents the circle fit to the V-plane, and the black points are the positions of the hits.

An issue arises when the determination of the LR-index assignment fails. From a simulation study [58], it is determined that when $|\theta| < 0.1\,\text{rad}$, the LR-ambiguity is correct 99.8% of the time and $\sim 64\%$ of all doublets have $|\theta| < 0.1\,\text{rad}$. For larger $|\theta|$, the difference between the LL and LR cases, and the difference between the RR and RL cases cannot be established, and therefore, the algorithm reverts back to the old approach but with one additional change.

Due to the shortcomings of the old t_0 algorithm, a new method of improving the t_0 for the cases where $|\theta| > 0.1$ is required. By defining three regions for all LL/LR and RR/RL tracks: high angle ($\theta > 0.1\,\text{rad}$), low angle ($\theta < -0.1\,\text{rad}$) and 'good' ($|\theta| < 0.1\,\text{rad}$). In the 'good' case the t_0 is determined from the fit to the data. In the two extreme angle cases, for both 'left' (LL/LR) and 'right' (RR/RL) tracks, offsets can be deduced from the mean (μ) of the Δt distribution as shown in Figure 6.8.

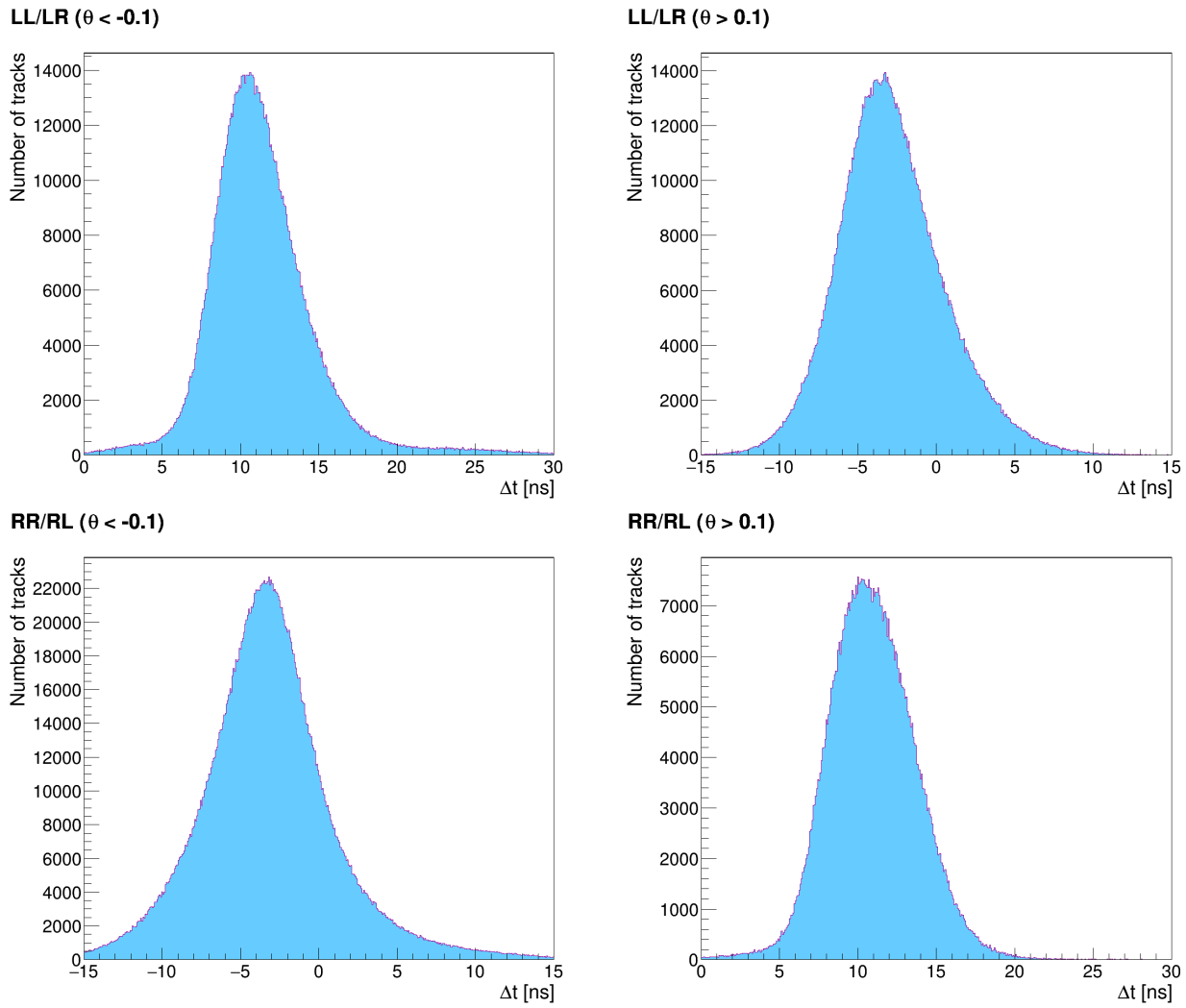

Figure 6.8: Δt distributions used to determine the offsets for the t_0 outside of the ($|\theta| < 0.1\,\text{rad}$) region where (a) LL/LR for ($|\theta| < -0.1\,\text{rad}$), (b) LL/LR for ($|\theta| > 0.1\,\text{rad}$), (c) RR/RL for ($|\theta| < -0.1\,\text{rad}$), (d) RR/RL for ($|\theta| > 0.1\,\text{rad}$).

These values can be used to correct the average t_0 for all tracks and thus improve the old approach irrespective of angular dependence. The offsets are given in Table 6.1.

LR-ambiguity	μ ($\theta > 0.1$)[ns]	μ ($\theta < -0.1$)[ns]
LL/LR	0.5382	14.0314
RR/RL	13.4087	-0.4785

Table 6.1: Mean of Δt distribution for high and low angle regions where the cut on θ fails.

This new algorithm was then compared against the old algorithm. The results can be seen in Figure 6.9, which shows the number of fitted tracks increases by 17% and that the p-values of the track fit is now improved across all tracks.

The straw-tracking detectors are used for the extraction of the spatial profile of the muon beam, including projections of the radial and vertical profiles. The extracted beam profile is

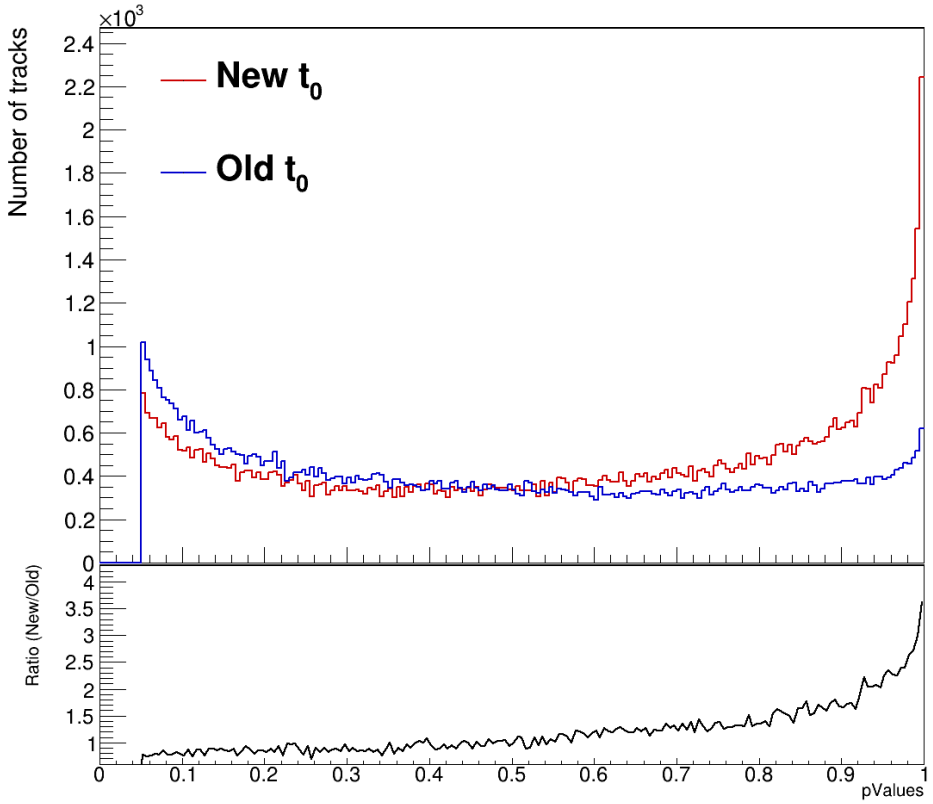

Figure 6.9: The p-value distribution of the fitted tracks for both the new and old t_0 algorithm.

necessary for the determination of the field convolution, the phase acceptance correction, the pitch correction, and tuning simulations. Therefore, a complete determination of the systematic uncertainties to the beam position from each area of the track extrapolation is needed, including the t_0 determination.

6.2 Systematic uncertainty on beam position from the t_0 determination

To estimate the systematic uncertainty on the beam position arising from the determination of the track t_0, an offset to the t_0 in the range ± 2 ns is applied. The data is then re-tracked with the new t_0, and the radial and vertical beam profile is extracted. The number of fitted tracks in a specific run against the offset is shown in Figure 6.10 which as expected peaks at an offset of ~ 0.

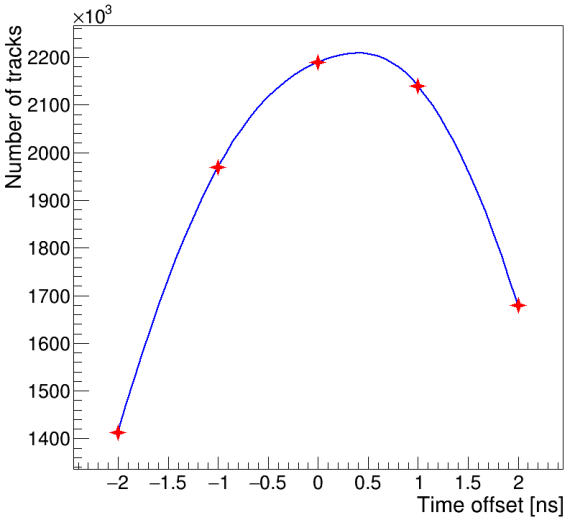

Figure 6.10: Number of extrapolated tracks as the t_0 is changed between ± 2 ns with respect to the nominal t_0.

The change in the mean and RMS of the extrapolated beam position both radially and vertically as the t_0 offset is changed is shown in Figures 6.11 and 6.12 respectively.

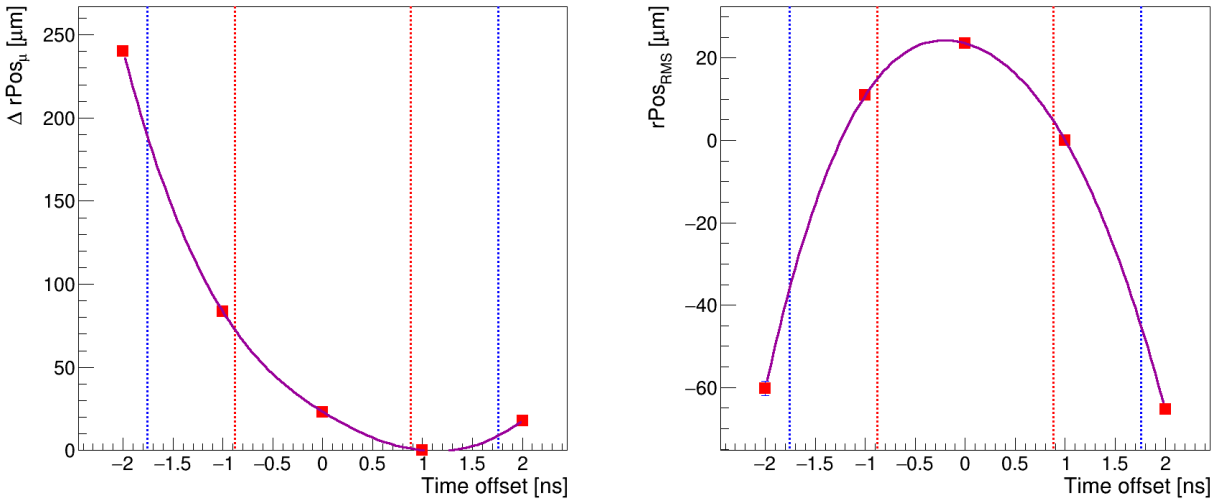

(a) (b)

Figure 6.11: (a): mean (b): RMS radial beam positions as a function of the t_0 offset. The red lines show a deviation of 0.88 ns (RMS of the new t_0 algorithm) and the blue lines show a deviation of 1.76 ns (RMS of the old t_0 algorithm).

The systematic uncertainty in the mean and RMS of the beam positions is taken as the largest deviation from the nominal value for a deviation of ± 0.88 ns i.e. the RMS of the new t_0 algorithm (Figure 6.6). The final systematic uncertainties were calculated for two runs in Run-2 (25896 and 25897) and two runs in Run-3 (34750 and 34751), and the final values can be seen in Table 6.2.

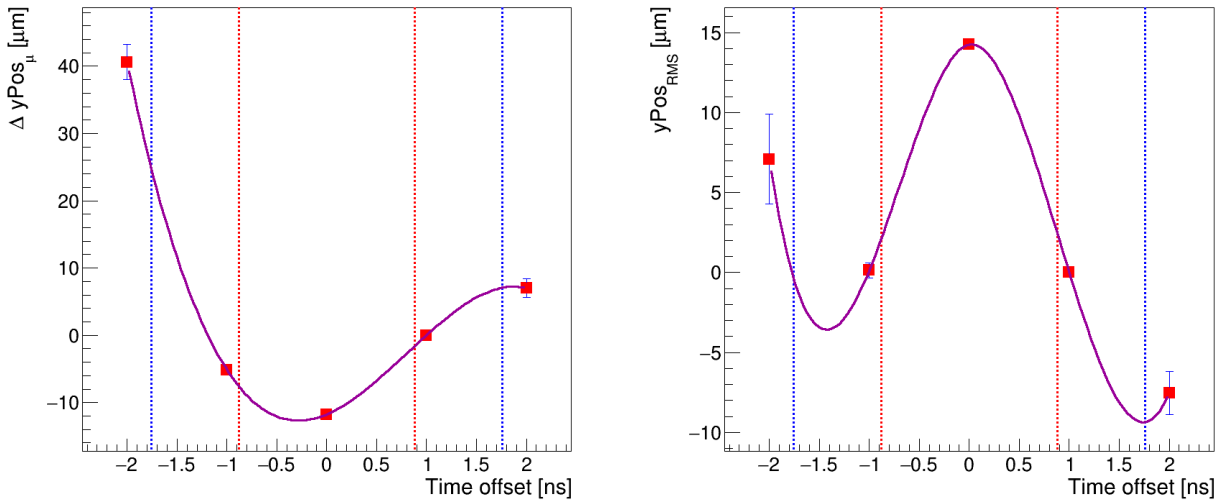

(a) (b)

Figure 6.12: (a): mean and (b): RMS vertical beam positions as a function of the t_0 offset. The red lines show a deviation of 0.88 ns (RMS of the new t_0 algorithm) and the blue lines show a deviation of 1.76 ns (RMS of the old t_0 algorithm).

Tracker Station	$\Delta\mu$R[μm]	$\Delta\sigma$R[μm]	$\Delta\mu$Y[μm]	$\Delta\sigma$Y[μm]
Run-2				
Station-12	−4.14	30.29	−9.75	−13.65
Station-18	24.13	33.85	−0.36	−11.80
Run-3				
Station-12	68.17	18.35	−10.67	2.68
Station-18	75.74	10.77	−2.75	−2.46

Table 6.2: Shifts in the mean radial ($\Delta\mu$R), vertical ($\Delta\mu$Y) position and RMS ($\Delta\sigma$R, $\Delta\sigma$Y) in Run-2 and Run-3 for the two straw tracker stations due to changes in t_0.

The results of this systematic uncertainty determination further highlight the importance of the newly developed t_0 algorithm. Small shifts in the t_0 lead to large shifts in the measured beam position. For example, using the RMS in the old t_0 algorithm of $\Delta t_0 = 1.76\,\text{ns}$ results in shifts in the mean radial position of $\sim 200\,\mu\text{m}$ whereas with the new algorithm they are $\sim 30\,\mu\text{m}$.

The new t_0 algorithm thus improves the track fits (better p-values), reduces the DCA resolution, leads to more tracks being reconstructed and significantly improves the determination of the beam position.

Chapter 7

Determining pileup in the tracking detector

In the Muon g-2 experiment, one of the largest systematic uncertainties in the straw tracking detectors comes from an effect known as "pileup", which dominates at early times in the fill, i.e., $t < 50\,\mu$s. Pileup is when multiple positrons enter the detector close in time such that the detector cannot distinguish them from each other.

In the calorimeter detectors, pileup is when two or more positrons enter close in time (within $\mathcal{O}(10\,\text{ns})$) in the same crystal and are measured as the sum of the independent positron energies. This is difficult to distinguish from a single positron of the same energy. In the straw tracking detectors, the pileup effect is slightly different. The pileup is, by definition, the same, but as the detectors only measure hit signals in the straws, the problem arises in the track reconstruction itself.

If two or more positrons enter the straw tracking detector within a small window of time, the reconstruction algorithm cannot always distinguish the independent trajectories and, therefore, can misassign hits from separate positrons to a single trajectory as shown in Figure 7.1.

This effect not only biases the number of reconstructed tracks but also biases the momentum distribution as the extracted momentum from the trajectory is not the real momentum of a positron. Rather, it is a skewed momentum from multiple positrons. These effects are more pronounced at early times in the fill since the rate of muon decays is highest, and hence, so is the number of hits at this time. This leads to the measured precession frequency being offset from the true frequency. The effect on the track reconstruction efficiency in the presence of pileup can be seen in Figure 7.2.

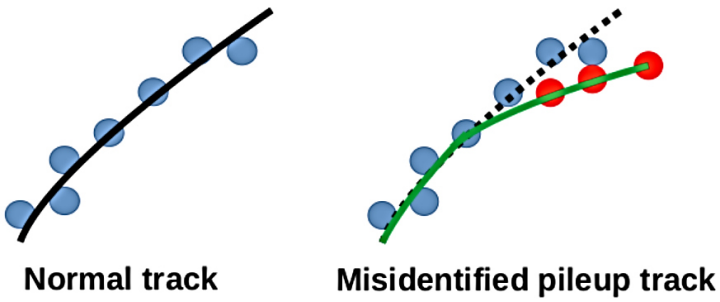

Figure 7.1: A schematic depiction of the pileup effect in track reconstruction.

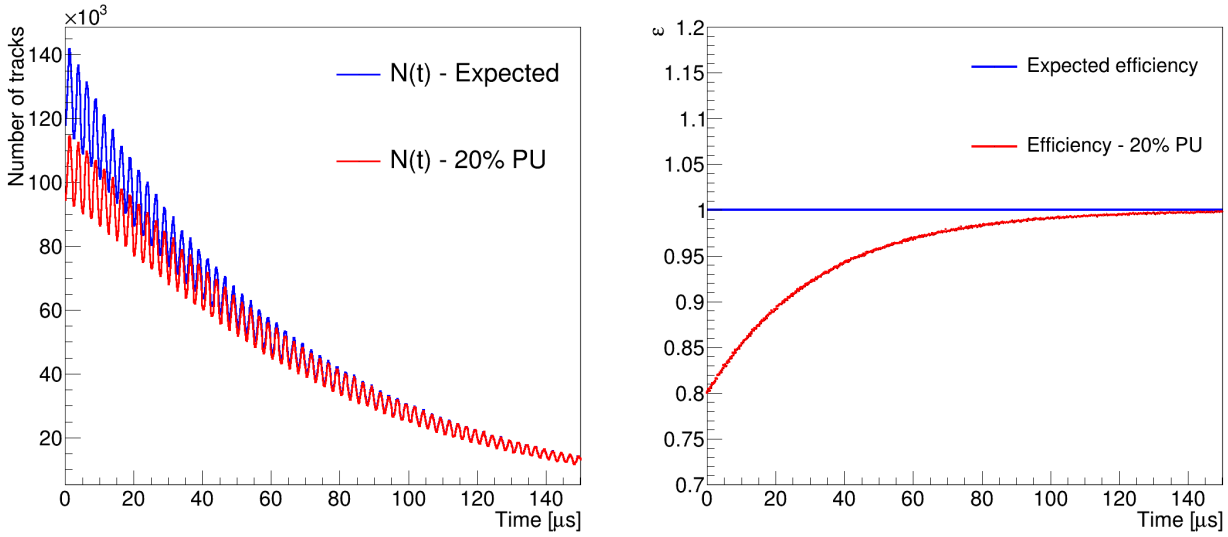

(a) (b)

Figure 7.2: A toy Monte-Carlo representation of the effect of pileup (PU) in (a) The number of tracks reconstructed as a function of time, N(t). (b) The track reconstruction efficiency compared to an ideal scenario where we expect to reconstruct 100% of tracks.

The leading contribution to pileup arises when two positrons arrive close in time and space. Since the time of the two positrons is independent, then the time dependence of this 'double' pileup is determined by the square of the underlying positron hit rate [59]. At a simple level, this will, therefore, modulate the number distribution of the positrons (Equation 3.20) with a contribution:

$$N(t) = N_{\text{pileup}} \cdot e^{-2t/\tau} \cdot \left[1 + A_0 \cdot \cos\left(\omega_a(R) \cdot t + \phi_{\text{pileup}}\right)\right]^2, \tag{7.1}$$

where N_{pileup} and ϕ_{pileup} reflect the magnitude and the phase of the pileup contamination.

In this chapter, two different iterative methods for estimating the rate of pileup in the straw tracking detectors are presented. The first method combines the data on a muon fill level by factors of 2, 3, or 5 and uses this to tune an analytical model that allows for an estimate of the pileup rate. The second uses a model based on a Poisson probability and the method shifts the data in time and combines it with the nominal data at the hit level to reconstruct the pileup spectrum, which can then be used to correct the data. Finally, an evaluation of the systematic uncertainty of the rate of pileup will be presented based on the two methods.

7.1 Combination and analytical model hybrid method

To understand the effect of pileup in the straw tracking detectors, an algorithm was developed to artificially inflate the rate of pileup to test the track reconstruction algorithm [60]. A new step is placed in the reconstruction before the individual hit signals are extracted. The muon fills in the storage ring are buffered and combined by an integer parameter. The selected parameters inflate the pileup by a factor of 1 (nominal data-set), 2, 3, or 5 such that PUN denotes a dataset with pileup enhanced by a factor N. A limit is placed on this step of 90 fills to ensure that each level of inflation has the same number of hits as the nominal reconstruction. The fills in which there are no hits are ignored. This combination effect is illustrated in Figure 7.3.

Using this method, we can see from Figure 7.4 which shows the extracted positron time distribution that the effect is indeed stronger at early times for each level of inflation where the rate of positrons is higher, and then it decays until it reaches equilibrium with the nominal spectrum.

We can also see from the momentum distributions in Figure 7.5 that the momentum is biased and proportional to the level of pileup inflation applied. The largest reduction in track reconstruction efficiency is at higher momentum.

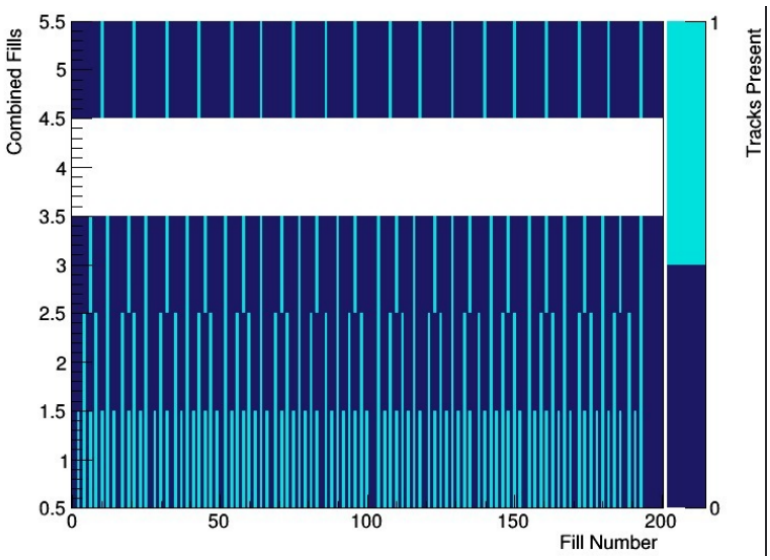

Figure 7.3: The combination of fills in the PUN method for each level of pileup with the y-axis showing the number of fills after the combination with empty fills where no tracks are present being ignored [60].

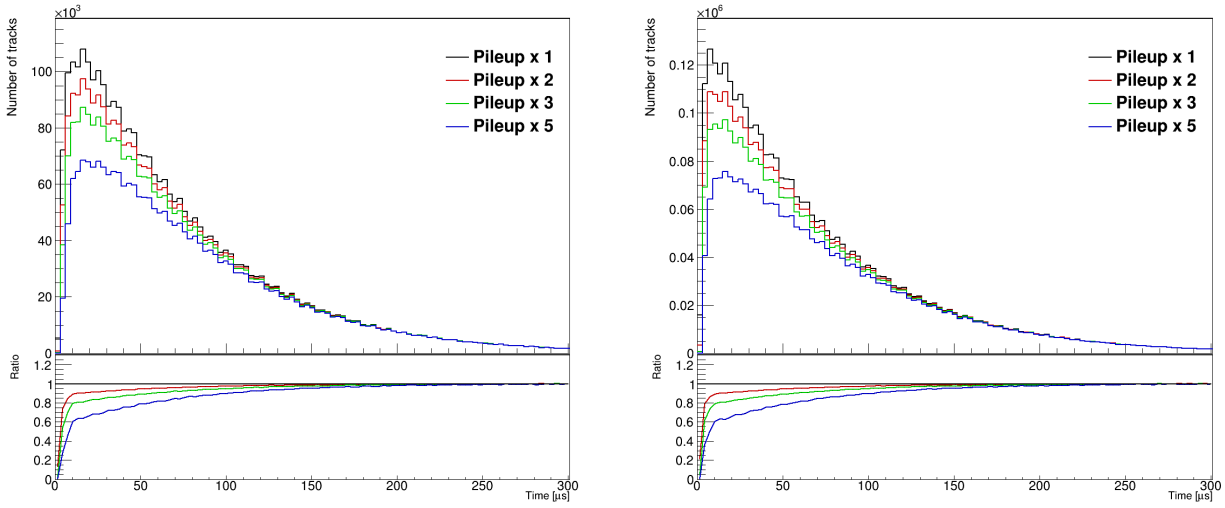

(a) (b)

Figure 7.4: The positron time distribution for each level of inflated pileup in the PUN method. A more significant effect is apparent at earlier times.

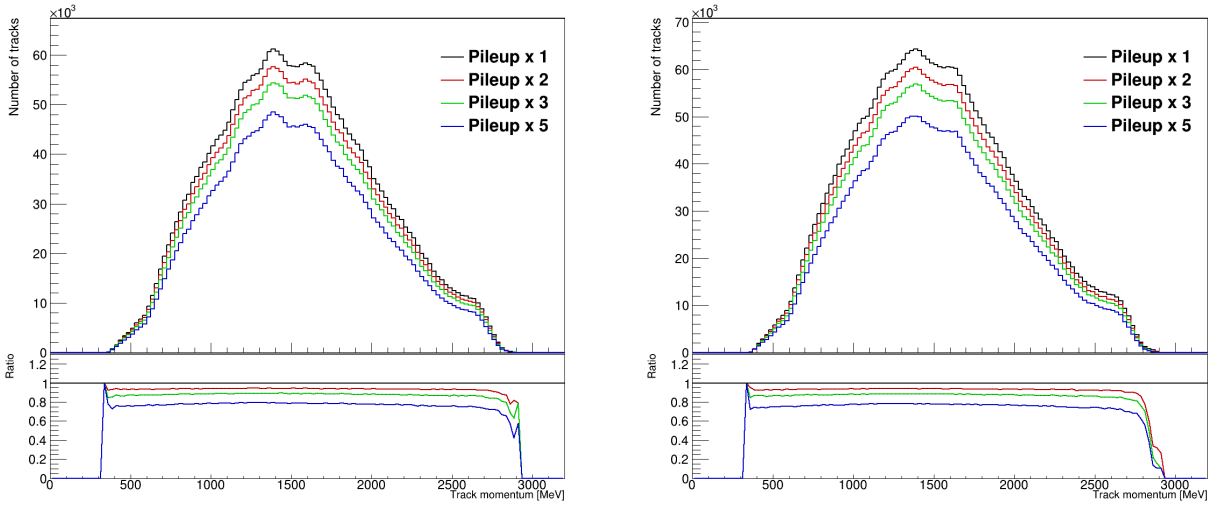

(a) (b)

Figure 7.5: The positron momentum spectrum for each level of inflated pileup showing the momentum is increasingly biased as the level of pileup is increased. The bias is more apparent at higher momenta ($p > 2.7\,GeV$).

To estimate the rate of 'true' pileup from the aforementioned method, an analytical model is developed. The number of detected tracks in the absence of pileup can be taken from

$$D(t) = \varepsilon_{\text{tr}} N(t) \tag{7.2}$$

where $D(t)$ is the detected number of reconstructed tracks, ε_{tr} is the efficiency of the track reconstruction itself and $N(t)$ is the total number of expected tracks. The total expected number of reconstructed tracks in a bin whose width is the cyclotron period (149.2 ns) can be determined from

$$r(t) = \frac{N(t)}{N_{\text{Fill}} \cdot \Delta t_{cyc}}, \tag{7.3}$$

where N_{Fill} is the total number of muon fills in the total dataset, and Δt_{cyc} is the width of the bin. This choice of bin width reduces impact of the fast rotation effect (Section 3.4.1). The total rate of expected 'double' pileup, where two tracks are reconstructed as a single track, is

$$r_d = r^2(t) \cdot t_{DT} \tag{7.4}$$

where t_{DT} is the deadtime, i.e., the duration for which tracks cannot be reconstructed, which is expected to be < 100 ns. This leads to the number of 'double' pileup in the data being

$$N_d(t) = N_{\text{Fill}} \cdot t_{cyc} \cdot r^2(t) \cdot t_{DT} \tag{7.5}$$

and with some rearranging, this leads to

$$N_d(t) = N(t) \cdot r(t) \cdot t_{DT}. \tag{7.6}$$

Similarly, the expected rate of 'triple' pileup is

$$r_t = r^3(t) \cdot t_{DT}^2 \tag{7.7}$$

and subsequently, the total number of 'triple' pileup is expected to be

$$N_t(t) = N(t) \cdot (r(t) \cdot t_{DT})^2. \tag{7.8}$$

At each subsequent order of pileup, a factor of $r(t) \cdot t_{DT}$ is introduced. If we take this only as far as the 'triple' pileup, we can then define ranges for the number of possible tracks that can be reconstructed for each order of pileup. If we have a single track (singlet) then we can reconstruct one or zero tracks i.e. the range in the possible number of tracks reconstructed, n_1, is $0 < n_1 < 1$. For two tracks, the range is $0 < n_2 < 2$ where we can reconstruct no tracks, one track or both tracks, etc. Thus, $D(t)$ corrected for pileup can be defined as

$$D(t) = \varepsilon_1 N_s(t) + 2\varepsilon_2 N_d(t) + 3\varepsilon_3 N_t(t) \tag{7.9}$$

where ε_i are efficiencies (ε_1 is the efficiency for reconstructing a singlet etc.) and $0 < \varepsilon_i < 1$. If we take the total number of tracks to be

$$N(t) = N_s(t) + 2N_d(t) + 3N_t(t) \tag{7.10}$$

and we do some algebraic manipulation then we obtain a term for the number of singlets, N_s, in the form of an arithmetico-geometric series as

$$N_s = N(t) \left(2 - \frac{1}{(1 - (r(t)t_{DT}))^2}\right). \tag{7.11}$$

Finally, we express $D(t)$ in terms of the sum of singlets and pileup as

$$D(t) = N(t) \left[\varepsilon_1 \left(2 - \frac{1}{(1 - (r(t)t_{DT})^2}\right) + 2\varepsilon_2 (r(t)t_{DT}) + 3\varepsilon_3 (r(t)t_{DT})^2\right]. \tag{7.12}$$

For the aforementioned pileup inflation method, we know for the PU2 case, the fills have been

combined, leading to an increase of a factor of two in the rate, which means the total number of detected tracks in this dataset can be determined by

$$D_2(t) = N(t)\left[\varepsilon_1\left(2 - \frac{1}{(1-2r(t)t_{DT})^2}\right) + 4\varepsilon_2(r(t)t_{DT}) + 12\varepsilon_3(r(t)t_{DT})\right]. \tag{7.13}$$

By taking the ratios of each subsequent PUN to the original case e.g. PU2/PU1, we can construct a model to then determine the original distribution with no pileup, PU0. As most of the factors cancel in the ratio, we obtain the form:

$$N_r(t) = \frac{\varepsilon_1 + 2(\varepsilon_2 - \varepsilon_1) f_{\text{pu}} r(t)t_{DT} + 3(\varepsilon_3 - \varepsilon_1)(f_{pu} r(t)t_{DT})^2}{\varepsilon_1 + 2(\varepsilon_2 - \varepsilon_1) r(t)t_{DT} + 3(\varepsilon_3 - \varepsilon_1)(r(t)t_{DT})^2} \tag{7.14}$$

where N_r refers to the ratio between the inflated and nominal distributions and f_{pu} represents the inflated pileup factor i.e. 1, 2, 3, or 5.

By fitting the case with the largest signal (PU5/PU1) iteratively, one can determine $\varepsilon_{1,2,3}$. We then correct the original distribution in our dataset, $D(t)$, by correcting each bin as follows

$$N_{\text{bin}}(t) = \frac{D_{\text{bin}}(t)}{\varepsilon_1 - \varepsilon_2 r(t)t_{DT} - \varepsilon_3(r(t)t_{DT})^2}, \tag{7.15}$$

allowing us to estimate the total without pileup

$$\frac{\int N_{\text{bin}(t)}}{\int D_{\text{bin}(t)}}. \tag{7.16}$$

Using a small subset of data, this analytical model approach was tested, and the results can be seen in Figure 7.6 where the estimated true pileup (PU0) is shown from the ratio compared to the nominal distribution. A cut was made at 30 μs in accordance with the ω_a analysis. From this result, we can deduce that the model is not perfect and is skewed in the fit for the lower levels of inflation, and so, at best, this only gives an approximate estimate of the true rate of pileup in the detector. The total estimated rate of pileup using this method is approximately $(5.29 \pm 0.02)\%$.

7.2 Shifted window algorithm method

The simple method defined in Section 7.1 is not optimal when trying to deduce the rate of pileup in the straw tracking detector data, and a more robust method is required. A new

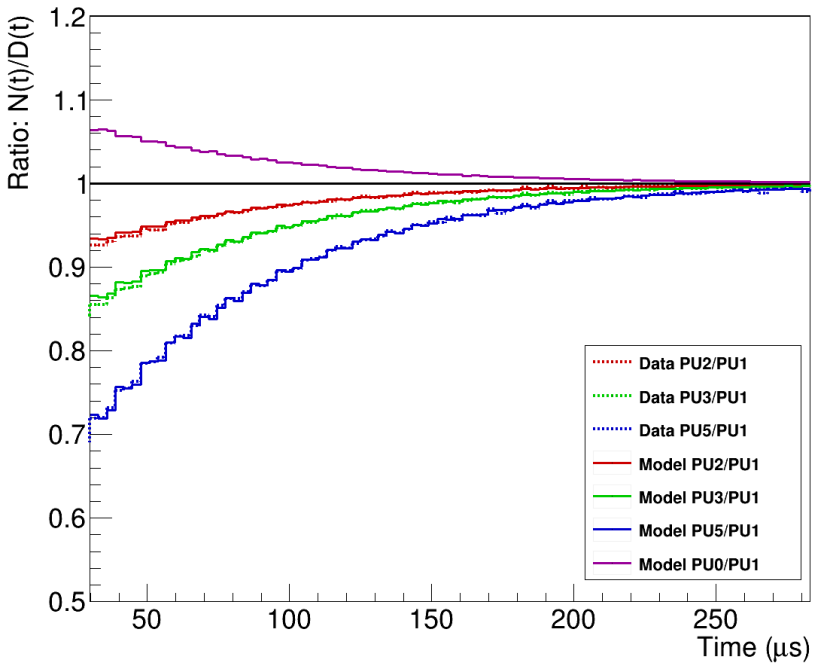

Figure 7.6: The results of the iterative fitting procedure of the analytical model model compared with the PUN method. As the fit quality reduces at the lower order of pileup, i.e., PU2/PU1, the model is not optimal.

algorithm method (PUA) was developed to give a more accurate estimate of the rate of pileup This new method takes place at the time-island level. Time-islands are defined in Chapter 5.

The positron hits are reconstructed up to the time-island level as normal. At this point, a window approach is taken where the original hits in each island are denoted by ρ_1. These hits are then duplicated and shifted back in time by 298 ns (two times the cyclotron period). This shift is chosen due to the pileup positrons being able to fall on either side of the initial positron in time. If they were only shifted by one cyclotron period, then it could lead a later positron to overlap and thus be still indistinguishable, whereas, with this shift in time, this issue does not arise. This shifted set of hits is denoted by ρ_2. Finally, a third set of hits is created, which contains the combination of the nominal and shifted tracks, and this is denoted by ρ_3. Each set of hits is passed once again through the entire track reconstruction algorithm to obtain three distinct sets of tracks.

To build the pileup spectrum from the three sets of reconstructed tracks, it is necessary to derive the form of the pileup corrected spectrum. This derivation follows from [61]. The average number of hits in each time-island can be denoted by α(t) defined by $\alpha(t) = r(t) \cdot \Delta t_{\text{island}}$, where r(t) is the hit rate and Δt_{island} is the time width of each island. Going forward, the time dependence of α(t) will be suppressed for clarity and will be denoted by α.

The hit times of the positrons are Poisson distributed. Taking the probability of having k hits in a time island, given an average number of hits α, as $p(\alpha, k)$, we can define this as a probability

$$p(\alpha, k) = \frac{\alpha^k e^{-\alpha}}{k!}. \tag{7.17}$$

From this, we can write the PDF explicitly for the $k = 0, 1, 2$ cases, giving us

$$p(\alpha, 0) = e^{-\alpha}, \tag{7.18}$$

$$p(\alpha, 1) = \alpha e^{-\alpha}, \tag{7.19}$$

$$p(\alpha, 2) = \frac{1}{2}\alpha^2 e^{-\alpha}. \tag{7.20}$$

If the hit rate is sufficiently low, such that $\alpha \ll 1$, then the exponential terms can be expanded as a power series in terms up to $\mathcal{O}(\alpha^2)$ to get

$$p(\alpha, 0) = 1 - \alpha + \frac{1}{2}\alpha^2, \tag{7.21}$$

$$p(\alpha, 1) = \alpha - \alpha^2, \tag{7.22}$$

$$p(\alpha, 2) = \frac{1}{2}\alpha^2. \tag{7.23}$$

$k = 1$ represents an island with a single hit, which we will denote by the subscript s and $k = 2$ an island with two hits with a subscript d then, Equations 7.21–7.23 can be expressed as a single equation:

$$\rho_{uc} = \left(\alpha - \alpha^2\right)_s + \left(\frac{1}{2}\alpha^2\right)_d, \tag{7.24}$$

where ρ_{uc} is our uncorrected positron time spectrum. As the pileup subtraction aims to have single reconstructed tracks with no pileup requiring no overlapping islands, then it is clear that the final corrected spectrum would be:

$$\rho_c = \alpha_s, \tag{7.25}$$

therefore the difference between the uncorrected (Equation 7.24) and corrected spectra (Equation 7.25) would give us the pileup spectrum itself, $\Delta\rho_{pu}$, defined as

$$\Delta\rho_{pu} = -\left(\alpha^2\right)_s + \left(\frac{1}{2}\alpha^2\right)_d. \tag{7.26}$$

To obtain the first-order empirical pileup spectrum, which will correct the measured spectrum to $\mathcal{O}(\alpha^2)$, the single shifted window is required as used in the algorithm. Though the hit rates are time-dependent due to the exponential decay and temporal and spatial motion of the beam, the chosen shifted window will reduce these rate changes. As the hit rates are independent to each island, the probability can, therefore, be computed by multiplying the probability of k_1 hits in the non-shifted island and k_2 hits in the shifted island as:

$$p(\alpha, k_1, k_2) = p(\alpha, k_1)p(\alpha, k_2). \tag{7.27}$$

Continuing with the previous notation, the combined islands can be denoted by $k_1 + k_2$ hits in the two separate islands. We can, therefore, write the combined island spectrum in the form

$$\rho_{1+2} = \sum_{k1+k2} p(\alpha, k_1)p(\alpha, k_2), \tag{7.28}$$

summed over all k_i's. Similarly, we can obtain the rate for the trigger island as

$$\rho_1 = \sum_{k1} p(\alpha, k_1)p(\alpha, k_2), \tag{7.29}$$

and the shifted islands as

$$\rho_2 = \sum_{k2} p(\alpha, k_1)p(\alpha, k_2). \tag{7.30}$$

Expanding up to terms of $\mathcal{O}(\alpha^2)$ we get:

$$\rho_{1+2} = \alpha_d^2, \tag{7.31}$$

$$\rho_1 = \rho_2 = \alpha_s^2. \tag{7.32}$$

Where $\rho_1 = \rho_2$ comes from the fact that the number of hits within these two islands are the same, they are just shifted in time. The combined island can be seen as 'what happened' in the presence of pileup and the individual islands to be 'what should have happened' such that the difference between the combined rate and the two individual rates should be proportional to the pileup and, therefore can be defined as:

$$\Delta\rho_{pu} = \rho_{1+2} - \rho_2 - \rho_1 = (-2\alpha^2)_s + (\alpha^2)_d. \tag{7.33}$$

From Equation 7.33 we can see that there is now a factor of $(-2\alpha^2)_s$ and $(\alpha^2)_d$ compared to

Equation 7.26 where there is a factor of $(-\alpha^2)_s$ and $(\frac{1}{2}\alpha^2)_d$ therefore multiplying by $\frac{1}{2}$ returns us to the actual correction. Using this expression and the three sets of reconstructed tracks, we can estimate the rate of pileup using:

$$\Delta\rho_{pu}(t) = \frac{\rho_{1+2}(t) - \rho_2(t) - \rho_1(t)}{2}. \tag{7.34}$$

Since we are allowing the second group of hits to fall at an offset δt on either side of the first hit, we are essentially doubling the 'dead-time,' and therefore, this leads to an over-counting. This is an intentional over-counting effect due to it allowing us to increase the statistical precision by sampling more data.

A caveat to this implicit definition is that it assumes that the rate at both times t and $(t + \delta t)$ are equal. However, even if we neglect the dead-time of the reconstruction, we still know that the actual sampling rate is the product of the two separate rates, which we can take to be of the form

$$\rho(t) \cdot \rho(t + \delta t) = \rho\left(t'\right) \cdot \rho\left(t'\right), \tag{7.35}$$

and when we assume that the effective time t' is the same as t, we can obtain an estimate for the rate of pileup. However, a much better approximation can be made by using the form of the absolute rate, $\rho(t)$, to solve Equation 7.35 for t'. From Equation 3.20, we can see that the rate depends on two components. The exponential-decay component where the rate depends on $e^{-t/\tau}$ and the muon spin precession component where the rate depends on $1 + A_0 \cos(\omega_a t + \phi_0)$.

In the case of the first component, there is an exact solution where $t' = t + \delta t/2$. However, with the inclusion of the second component, there is now a direct dependence between t' and t that is bounded by 0 and δt. This means that if the muon spin precession rises more than the exponential falls, there is an offset between the two rates in Equation 7.35, which causes $\rho(t) = \rho(t + \delta t)$ [59]. Thus, the pileup rate will oscillate with ω_a , and it will be delayed by $\delta t/2$, which has to be accounted for when measuring ω_a .

Once the three sets of tracks are obtained, they are used to calculate the rate of pileup described in Equation 7.34 at a bin-by-bin level and placed into a histogram as shown in Figure 7.7. This histogram is then subtracted bin-by-bin from the nominal positron time distribution to obtain a 'pileup-corrected' distribution. As with the PUN method, this can then be denoted by the ratio to the nominal distribution to find our estimated level of pileup.

The estimated level of pileup was found to be $(5.25 \pm 0.02)\%$ which is within 2 standard

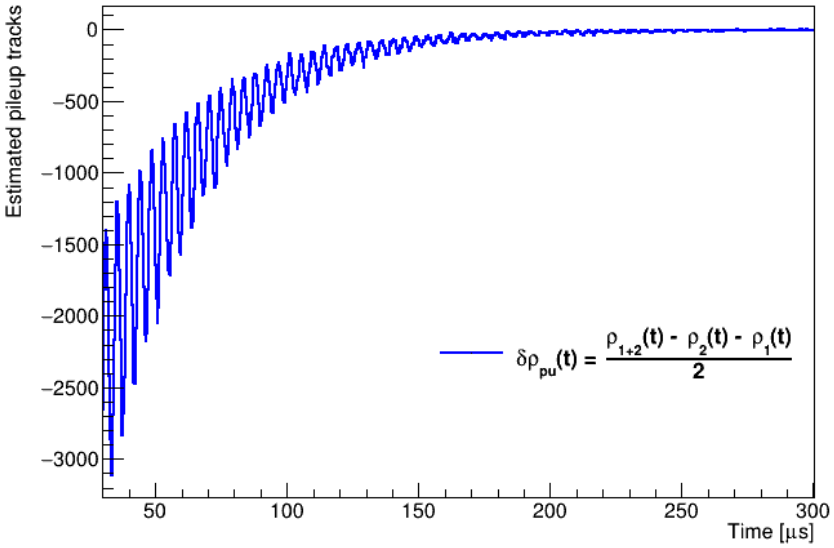

Figure 7.7: An example of the extracted pileup distribution as a function of time, which is then subtracted from the nominal distribution.

deviations of the analytical model. As the analytical model was only a loose approximation, they would not be expected to agree perfectly. The full comparison of the PUA method to the PUN method is shown in Figure 7.8.

7.3 Crosschecks and final evaluation

The final test to ensure the new PUA method works as expected is to form a cross-check hybrid method (PUHybrid). This method works by using the PUN method to combine the fills, and then in the same algorithm, we take the newly buffered time islands, perform the PUA method, and retrack again. As the PUN method is a rough combination of all of the fills, the ratio between each subsequent level of inflation should be the same to ensure the new PUA method is not artificially inflating the pileup.

In the PUHybrid method, PUH2/PUH1 should be the same as PUH3/PUH2. If the correction has been applied correctly from the algorithm, the ratios should be ∼1.0. The results for this crosscheck can be seen in Figure 7.9.

In order to evaluate the systematic uncertainty on the obtained result for the pileup, we can use a combination of both methods to provide a conservative estimate. The analytical model can be trained on both the PU3 and PU5 cases to give a range of the total level of the pileup. This can then be averaged and subtracted from the rate of pileup obtained by the algorithm

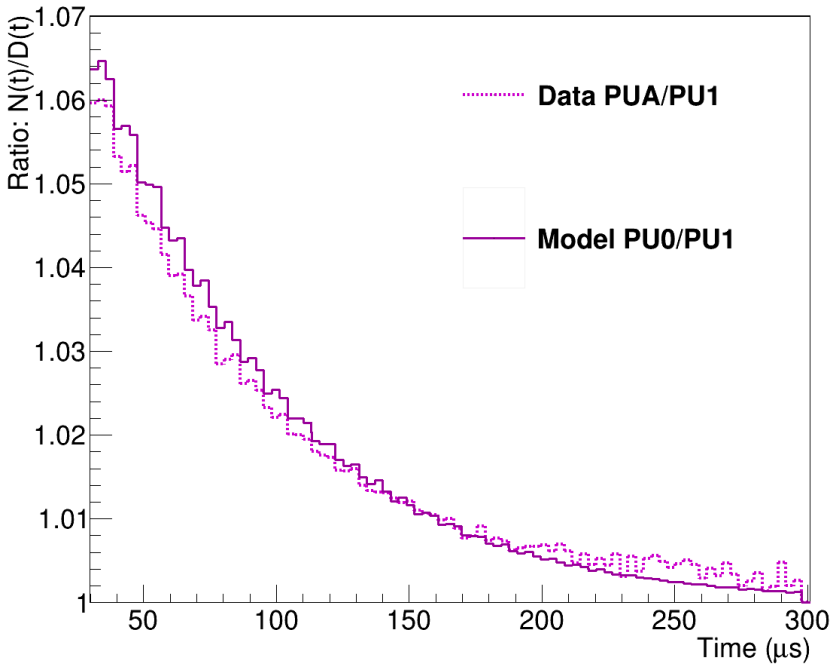

Figure 7.8: A comparison between the pileup estimated from the PUA method compared with the analytical model.

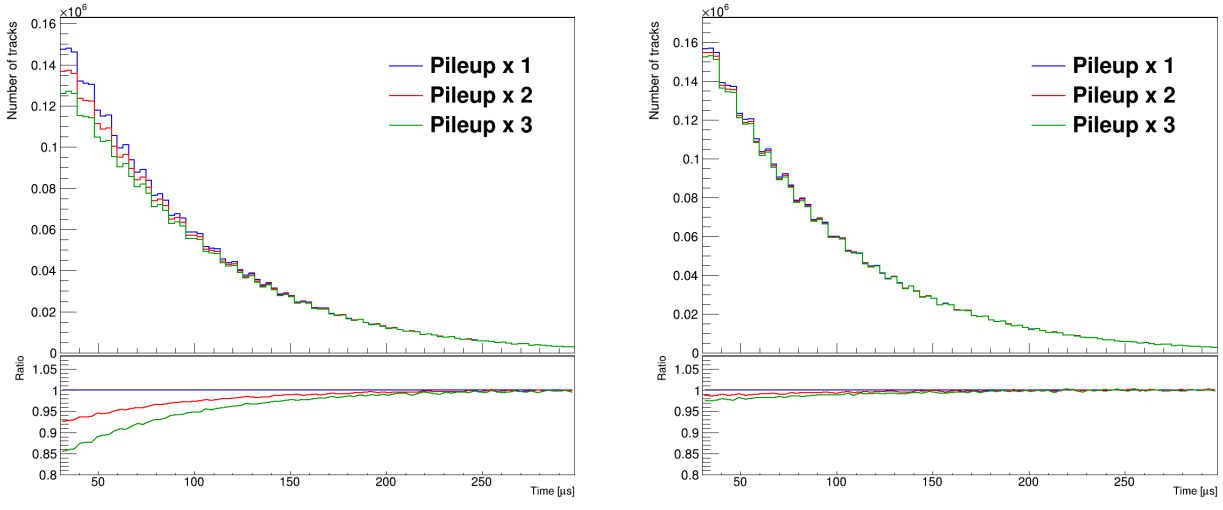

(a) (b)

Figure 7.9: The PUHybrid method shows (a) the nominal PUN spectrum with inflated levels of pileup. (b) The spectrum for each inflated level of pileup corrected by the pileup algorithm. The ratios after the correction is applied are close to 1.0 with some residual deviations at early times.

to give the systematic uncertainty.

The pileup is not necessarily the same in each tracker station, and therefore, this is evaluated for each station separately. Also, as we are tuning on two different sets of data, then the difference in the results between the two fits must be accounted for in the systematic uncertainty. The results for the total systematic uncertainty for the two tracker stations are shown in Table 7.1.

Tracker Station	$\%_{\mathrm{PU}}$(PU(a)	$\%_{\mathrm{PU}}$(PU5)	$\%_{\mathrm{PU}}$(PU3)	$\%_{\mathrm{PU,avg}}$(PUN)	$\Delta\%_{\mathrm{PU}}$(PUA-PUN)
Station-12	5.03 ± 0.02	4.74 ± 0.02	4.83 ± 0.02	4.79	0.24
Station-18	5.47 ± 0.02	5.84 ± 0.02	5.91 ± 0.02	5.88	0.41

Table 7.1: Systematic uncertainty evaluation for the level of pileup in each of the tracker stations. $\%_{\mathrm{PU}}$(PU(a) is the value from the PUA method, $\%_{\mathrm{PU}}$(PU5) and $\%_{\mathrm{PU}}$(PU3) are from the PUN method tuning on the PU5/PU1 and PU3/PU1 cases respectively, $\%_{\mathrm{PU,avg}}$(PUN) is the average and finally $\Delta\%_{\mathrm{PU}}$(PUA-PUN) is the difference between the PUA method and the average of the PUN methods.

The final results for the rate of pileup in each tracker station accounting for both the statistical and systematic uncertainties are shown in Table 7.2 in which they can be seen to agree between stations within the systematic uncertainty.

Tracker Station	$\%_{\mathrm{PU}}$(PU(a)	$\sigma_{\mathrm{PU,syst}}(\%)$	$\sigma_{\mathrm{PU,stat}}(\%)$
Station-12	5.03	0.24	0.02
Station-18	5.47	0.41	0.02

Table 7.2: Evaluated rate of pileup for each tracker station with the associated systematic and statistical uncertainties.

The straw tracking detectors are used to provide precise measurements of the stored muon beam for the evaluation of the phase acceptance and pitch corrections to the ω_a measurement as mentioned in Section 3.4. It is essential to understand how the pileup in the data affects the measured beam position. To calculate the systematic effect this has on the radial and vertical beam position, the pileup corrected data can be compared with the nominal data, and the change in the extrapolated beam position can be calculated for each station. This comparison is shown in Figures 7.10.

The systematic uncertainty was calculated using ten runs from Run-2 (25896–25905) and ten runs from Run-3 (34750–34759). A time cut was placed on the data at 30μs to match the ω_a measurement from the calorimeters.

The full systematic uncertainties can be seen in Table 7.3. The systematic effect on the extrapolated beam position is small ($< 10\,\mu$m). However, it has a non-negligible effect on the straw

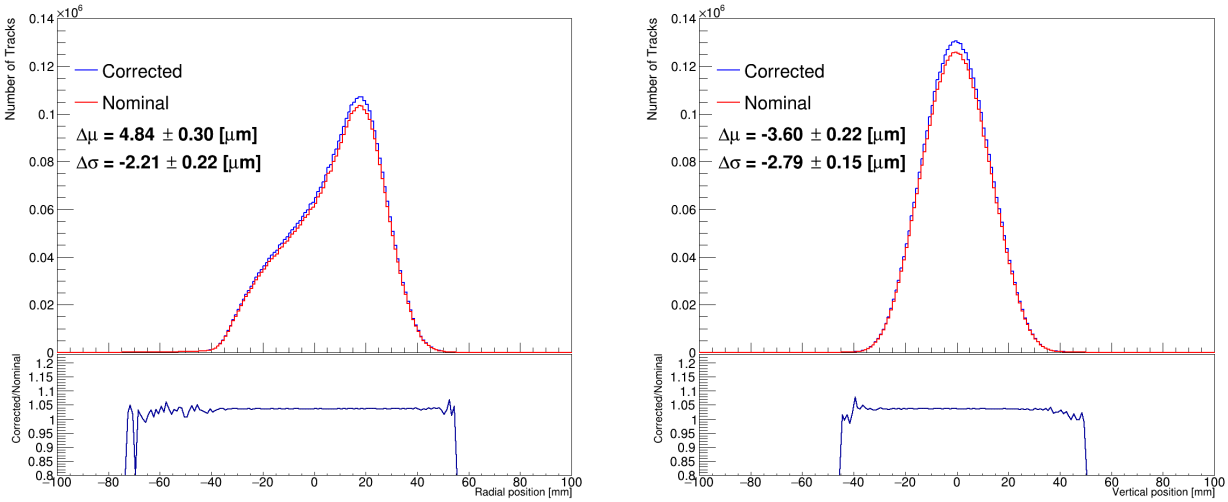

(a) (b)

Figure 7.10: Comparison of nominal and pileup corrected beam-extrapolation for (a) radial position and (b) vertical position

tracker based precession frequency analysis which is discussed in Section 9.2.

Tracker Station	$\Delta\mu$R[μm]	$\Delta\sigma$R[μm]	$\Delta\mu$Y[μm]	$\Delta\sigma$Y[μm]
Run-2				
Station-12	4.84 ± 0.30	-2.21 ± 0.22	-3.60 ± 0.22	-2.79 ± 0.15
Station-18	5.84 ± 0.32	-3.19 ± 0.22	-2.53 ± 0.23	-0.84 ± 0.16
Run-3				
Station-12	3.55 ± 0.29	-0.50 ± 0.20	-1.72 ± 0.23	-1.52 ± 0.16
Station-18	5.76 ± 0.30	-2.54 ± 0.21	-1.31 ± 0.23	0.17 ± 0.16

Table 7.3: Shifts in the mean radial ($\Delta\mu$R), vertical ($\Delta\mu$Y) position and RMS ($\Delta\sigma$R, $\Delta\sigma$Y) in Run-2 and Run-3 for the two straw tracker stations due to pileup.

Chapter 8

Track-based anomalous spin precession frequency measurement

The work detailed in this thesis presents a measurement of the anomalous muon spin precession frequency using the straw tracking detectors for the data taken in Run-2 and Run-3. At the time of this thesis, the calorimeter measurements have now been fully combined and unblinded in both software and hardware, meaning the hardware unblinding is now known for this analysis. However, the analysis presented in this thesis remains blinded in software. This chapter will present the procedure and measurement of the anomalous spin precession frequency. Chapter 9 will discuss the systematic uncertainties relevant to this measurement.

8.1 Datasets

For the Run-1 dataset that was taken in 2018, the sub-datasets were decided based on different kicker and electrostatic quadrupole conditions. However, in Run-2 and most of Run-3, these conditions remained relatively consistent across the running period. It was discovered in the Run-1 dataset that there were damaged quadrupole resistors, which increased the muon losses and the beam motion. For these reasons, it was decided that the Run-1 dataset would not be used for this analysis. During Run-2, there were significant fluctuations in the hall temperature, which caused changes to the magnetic field across the run period. The hall temperature was stabilised between Run-2 and Run-3, and the conditions remained stable throughout most of Run-3 until near the end of the run period, when hardware improvements were introduced to increase the kicker voltage which placed the beam much closer to a central orbit than was

Dataset	Number of Tracks	% of Run-2+3a+3b
2B	2.6×10^7	2.6
2C	11.3×10^7	11.1
2D	9.8×10^7	9.6
2E	4.2×10^7	4.1
2F	4.0×10^7	3.9
2G	0.8×10^7	0.8
2H	1.2×10^7	1.1
3B	5.3×10^7	5.2
3C	1.7×10^7	1.7
3D	11.1×10^7	10.9
3E	4.8×10^7	4.7
3F	2.1×10^7	2.1
3G	5.4×10^7	5.3
3I	5.2×10^7	5.1
3J	3.8×10^7	3.7
3K	2.3×10^7	2.3
3L	1.7×10^7	1.7
3M	5.4×10^7	5.3
3N	10.8×10^7	10.6
3O	8.2×10^7	8.1

Table 8.1: Number of reconstructed tracks (with $p > 1.8\,\text{GeV}$ and $t > 30\,\mu\text{s}$) used for the ω_a analysis for each sub-dataset.

the case previously. Due to these reasons, the data will be analysed in three distinct groups: Run-2, Run-3a, and Run-3b. Run-2 was split into seven sub-datasets that were defined by the offline team for the data production. These ran from Run-2B through to Run-2H, which were segmented by cycles of the storage magnet and trolley runs. Run-3a, defining the period before the kicker upgrade, contained eleven sub-datasets that ran from Run-3B through to Run-3M (with the exclusion of Run-3H). Finally, the last dataset defining the period after the kicker upgrade contained just two sub-datasets, Run-3N and Run-3O.

8.2 Preparing the analysis histograms

For the analysis outlined in this thesis, tracks that passed the quality requirements defined in Section 5 were selected. To mitigate the effect of any fast-rotation effects the time bin chosen for the analysis was that of the cyclotron period (149.2 ns).

For this analysis, a so-called threshold method (T-method) is used to extract the frequency. As shown in Section 3.2 for the straw tracker data, the statistical precision of the blinded frequency

R is minimised when the quantity NA^2 is at its maximum at a momentum of 1800 MeV: only tracks above this momentum are used in the analysis.

As well as a selection of optimal requirements on the quality of the tracks and momentum, an optimal start time for the ω_a fit must be selected. There are multiple things to consider when selecting this start time. As the muons decay exponentially with time, the statistical precision is reduced the later in the fill the fit is started. However, as shown in previous chapters, there are effects that have significant systematic uncertainties and are dominant at early times, e.g., muon losses, pileup, and beam dynamics effects. Therefore, the selection has to balance the statistical and systematic uncertainties. As with the calorimeter analysis, and to ensure the start time for the ω_a fit is aligned with one of the cyclotron-period bins, the start time was set to 30.2876 μs.

8.3 The fitting procedure

In this section, the procedure for the fit to the data will be presented in steps and the associated systematic uncertainties will be presented for the final fit.

8.3.1 The five-parameter fit

The first stage of the fitting procedure was to fit the data to a five-parameter model given by the expected modulation to the number of tracks as a function of time due to the simple harmonic motion of the beam with an exponential dependence on the muon lifetime. Although this fit is missing a lot of the crucial information required and the quality of the fit is expected to be poor, this step is necessary to elucidate and inform the later steps of the procedure. This function takes the form

$$N(t) = N_0 e^{-t/\tau} \left[1 + A\cos\left(R\,t + \phi\right)\right], \tag{8.1}$$

where N_0 is the normalisation factor, τ is the time-dilated lifetime, A is the asymmetry and ϕ is the phase and R is the blinded spin precession frequency. The fitting procedure uses the ROOT fit method combining both the `MINUIT` and `MINOS` methods [63] to calculate a χ^2 minimisation with the data to determine the optimal parameters for the initial model.

The quality of the fit as expected has a reduced χ^2 of 27.84, and the fit pulls (residuals between the fit function and the data in a given time bin) deviate significantly from the expected mean

of 0.0 and $\sigma = 1.0$ as shown in Figure 8.1 which has non-Gaussian residuals and is skewed.

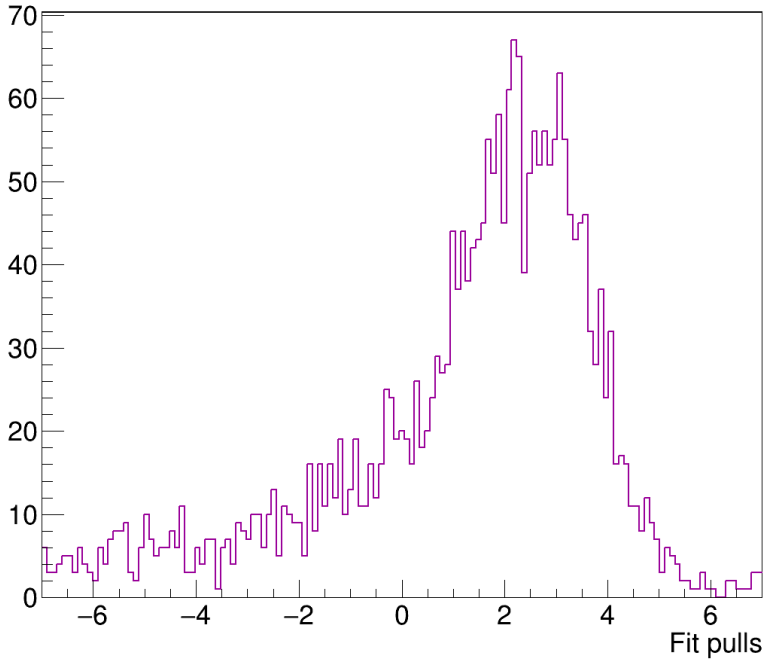

Figure 8.1: The pulls from the five-parameter fit to the data.

The quality of the fit can then be further probed by performing a fast-Fourier transform (FFT) from the time domain to the frequency domain as shown in Figure 8.2. If the fit describes the data well, the FFT should be flat with no prominent peaks. As we can see from the FFT, there is a substantial peak at 0 MHz as well as other substantial peaks at various frequencies. These frequencies match with known frequencies of various beam dynamics effects as mentioned in Section 4.3. The major contributing frequencies are listed in Table 8.2. The frequencies marked specifically in the FFT range with the associated beat frequencies are listed in Table 8.3.

Muon beam frequencies				
Name	Symbol	Expression	Frequency [MHz]	Period [ns]
$g-2$	f_a	$a_\mu Be/2\pi mc$	0.229	4365
cyclotron	f_c	$v/\pi R_0$	6.702	149.2
horizontal betatron	f_{xBO}	$\sqrt{1-n}f_c$	6.330	158.0
vertical betatron	f_{yBO}	$\sqrt{n}f_c$	2.203	453.8
coherent betatron	f_{1CBO}	$f_c - f_{\mathrm{xBO}}$	0.373	2684
vertical waist	f_{VW}	$f_c - 2f_{\mathrm{yBO}}$	2.295	436.6

Table 8.2: The beam frequencies and the respective period for the Run-2 dataset. f_a is the expected signal frequency. The rest of the frequencies are due to the spatial and temporal motion of the beam.

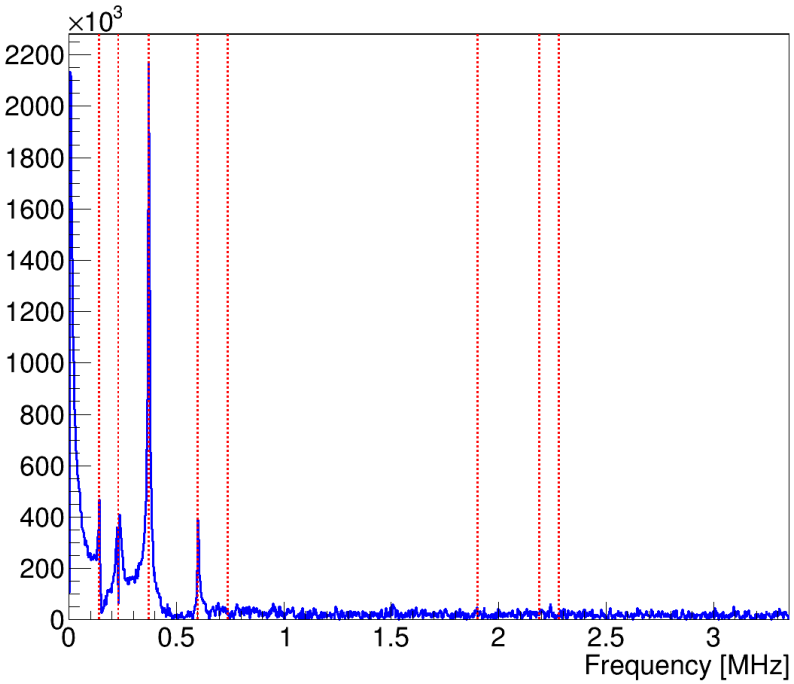

Figure 8.2: The FFT of the residuals of the five-parameter fit to the data.

Muon beam and beat frequencies	
Symbol	Frequency [MHz]
$f_{1\mathrm{CBO}} - f_a$	0.144
f_a	0.229
$f_{1\mathrm{CBO}}$	0.373
$f_{1\mathrm{CBO}} + f_a$	0.602
$f_{2\mathrm{CBO}}$	0.746
f_{VW}-$f_{1\mathrm{CBO}}$	1.922
f_{yBO}	2.203
f_{VW}	2.295

Table 8.3: The major frequencies and respective beat frequencies shown in the FFT of the residuals from the fit to the data.

8.4 Randomisation of the data

The analysis presented in this thesis uses a randomisation approach to correct for beam motion effects prior to fitting. This randomisation process samples and applies random offsets to the data to filter out two distinct effects. The first effect is the so-called vertical waist (VW) effect with a period of 436.6 ns. This describes the width of the vertical harmonic motion of the beam as it cycles the azimuth of the storage ring. Randomising out this effect also removes other vertical beam motion effects, namely, the residual beat frequency between both the VW frequency itself and the CBO frequency, as well as the frequency of the vertical betatron motion. The second effect is the imparted oscillations in the beam motion due to the fast-rotation. This oscillation is referred to as 'fast' due to the fact its period is 149.2 ns and the period of the frequency is 4.37 μs. The methodology and application of this randomisation procedure will be described in the following section.

8.4.1 Vertical waist

Due to the relatively low statistics of the data from the straw tracker detector, it is difficult to get stable fits with a function with too many free parameters. The effect of the vertical waist can be suppressed such that it does not have to be included in the final fit by applying a random offset δt_{VW} to each positron time. With the range of δt_{VW} defined by the vertical waist period i.e.

$$\delta t_{\mathrm{VW}} \in [-T_{\mathrm{Vw}}/2, T_{\mathrm{Vw}}/2]\,. \tag{8.2}$$

Due to this effect being a 'fast' oscillation similar to the fast-rotation, the inclusion of the randomisation procedure only has a small effect on the precision of the ω_a determination. The statistical uncertainty on ω_a is only increased by 1-2% [64]. Randomising, at the vertical waist period, also suppresses the beat frequency between the VW and the CBO [65], as well as the effect of the vertical betatron motion of the beam [66]. This means that both of these effects are also no longer required to be accounted for in the fit function.

8.4.2 Fast-rotation

As with the vertical waist, the effects from the fast-rotation should ideally also be included in the fit function. However the binning at the cyclotron period significantly reduces its effect and a similar randomisation to above can essentially eliminate its impact. Even the calorimeter

analysis with far higher statistics has had to employ this mitigation strategy to achieve stable fits. As in the vertical waist case, the positron hit times are randomly offset but in this case in a range defined by the cyclotron period:

$$\delta t_{\mathrm{FR}} \in [-T_{\mathrm{c}}/2, T_{\mathrm{c}}/2]\,. \tag{8.3}$$

This randomisation also reduces the effect of the so-called R-wave. As the beam traverses the azimuth of the storage ring, it induces a fast-rotation signal in each of the 24 calorimeters, which, for each adjacent calorimeter, has a $\sim 2\pi/24$ phase difference. This effect, therefore, induces an azimuthal bias in the extracted frequency, R, as shown in Figure 8.3 where it is also shown that the randomisation significantly reduces the amplitude of the bias.

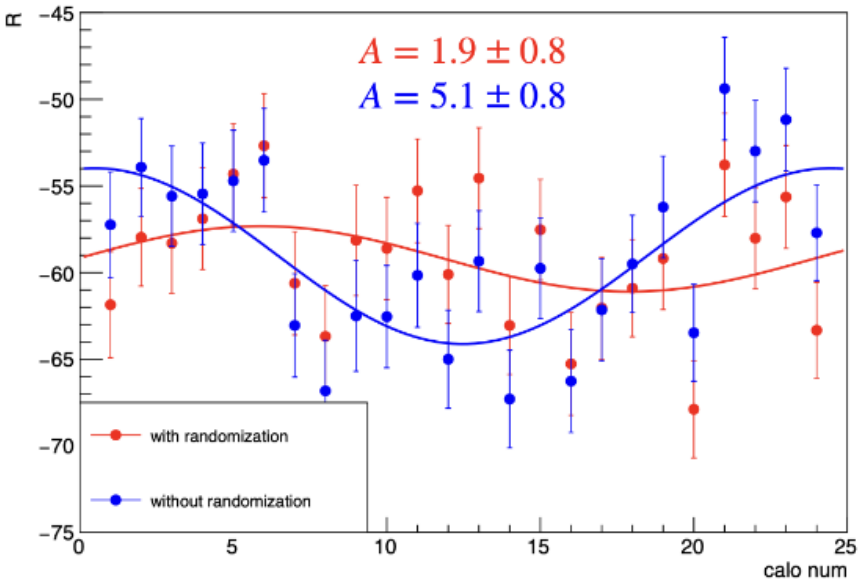

Figure 8.3: The extracted value of R (in ppm), per-calorimeter, in Run-2C. Points with and without the randomisation at the cyclotron period are shown. The randomisation reduces the amplitude of the sinusoidal oscillation by a factor of ~ 2.5 [37].

The application of the randomisation procedure for both the vertical waist and fast-rotation removes the respective signals. However, the value of R extracted from the fits will, of course, depend on the seed used for the randomisation. Although each seed will produce a reasonable value for R, the procedure must be repeated over many random seeds, and the final value for R is then taken as the average value. For the analysis presented in this thesis, the chosen number of seeds is 100.

8.5 Beam dynamics corrections

As mentioned in Section 4.3 there are systematic effects introduced from the motion of the beam. Although in the previous section, it can be seen that via randomisation, the vertical beam motion and fast-rotation effects can be removed prior to fitting; however, as shown in Figure 8.2, the most substantial peak except for the one at 0 MHz is at the CBO frequency. Due to this, without the inclusion of the horizontal CBO effects being accounted for within the model, the fit will be poor and unlikely to converge, as well as masking other possible contributions.

8.5.1 The nine-parameter fit

The first step in understanding the impact of the CBO on the analysis is to form a nine-parameter fit. Since the CBO decoheres over time, we can model, to first order, the CBO with an exponential envelop of the form

$$N_{CBO}(t) = 1 + A_{1CBO,N} e^{-t/\gamma\tau_{CBO}} \cos\left(\omega_{CBO} t + \phi_{1CBO,N}\right) \tag{8.4}$$

where the newly added terms for the asymmetry, lifetime, frequency and phase associated with the CBO are taken as free parameters in the fit function. This then simply modifies the five-parameter fit as follows:

$$N(t) = N_0 N_{CBO} e^{-t/\gamma\tau} \left[1 + A\cos\left(R\,t + \phi\right)\right]. \tag{8.5}$$

By once again checking the FFT of this new fit, we can see the impact of including the CBO within the fit function, if only in a naive sense. The FFT for this fit can be seen in Figure 8.4. As shown in Figure 8.4, the peak centred around the CBO frequency at 0.373 MHz has been removed; however, some peaks still remain. The reduced χ^2 for this fit is 18.52 which is an improvement from the five-parameter fit, but it is still poor.

8.5.2 Full CBO correction

As shown in the previous section, even with a naive, basic model, we can remove the peak at the CBO frequency very well. From this, we will then extend our model to include the

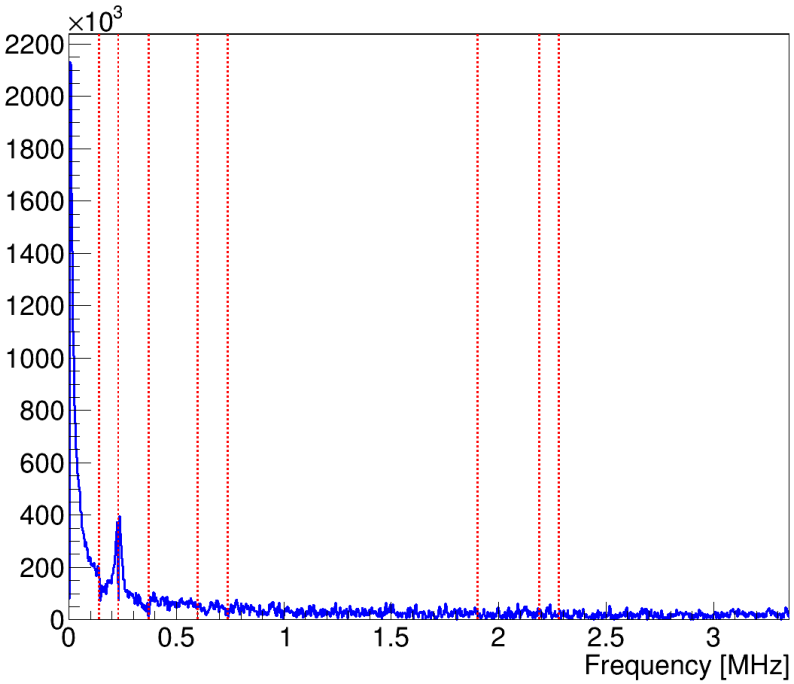

Figure 8.4: The residual FFT of the nine-parameter fit to the data showing the reduction in the CBO peak.

contributions from the second harmonic of the CBO. For the full model, we get the fit function

$$N(t) = N_0 \cdot N_{1CBO} \cdot N_{2CBO}(e^{-t/\tau}\left[1 + (A \cdot A_{CBO})\cos\left(Rt + \phi + \phi_{CBO}\right)\right], \tag{8.6}$$

where we now have four separate contributions. N_{1CBO} is the same as defined in the nine-parameter fit; however we now have the inclusion of N_{2CBO}, which is a term that modulates the normalisation term N_0 in the fit function at twice the CBO frequency

$$N_{2CBO}(t) = 1 + A_{2CBO}e^{-2t/\tau_{CBO}}\cos\left(2\omega_{CBO}t + \phi_{2CBO}\right), \tag{8.7}$$

where we have the addition of two new fit parameters A_{2CBO} and ϕ_{2CBO} and the lifetime is now halved. This term is included to correct for acceptance effects arising from the radial width of the beam. As the oscillation term of the radial width is squared, this facilitates the need for an exponential decaying at half the lifetime and an oscillation term of twice the base CBO frequency.

We also must include a modulation to the asymmetry and phase, A_{CBO} and ϕ_{CBO} respectively,

which are defined as

$$\begin{aligned} A_{CBO}(t) &= 1 + A_{1CBO,A} e^{-t/\tau_{CBO}} \cos\left(\omega_{CBO} t + \phi_{1CBO,A}\right), \\ \phi_{CBO}(t) &= 1 + A_{1CBO,\phi} e^{-t/\tau_{CBO}} \cos\left(\omega_{CBO} t + \phi_{1CBO,\phi}\right) \end{aligned} \tag{8.8}$$

which once again depend on the lifetime and frequency of the first-order CBO but with two new fit parameters for the asymmetry and phase of both contributions. The FFT for the fit with the inclusion of the full CBO parameterisation can be seen in Figure 8.5. The incorporation of

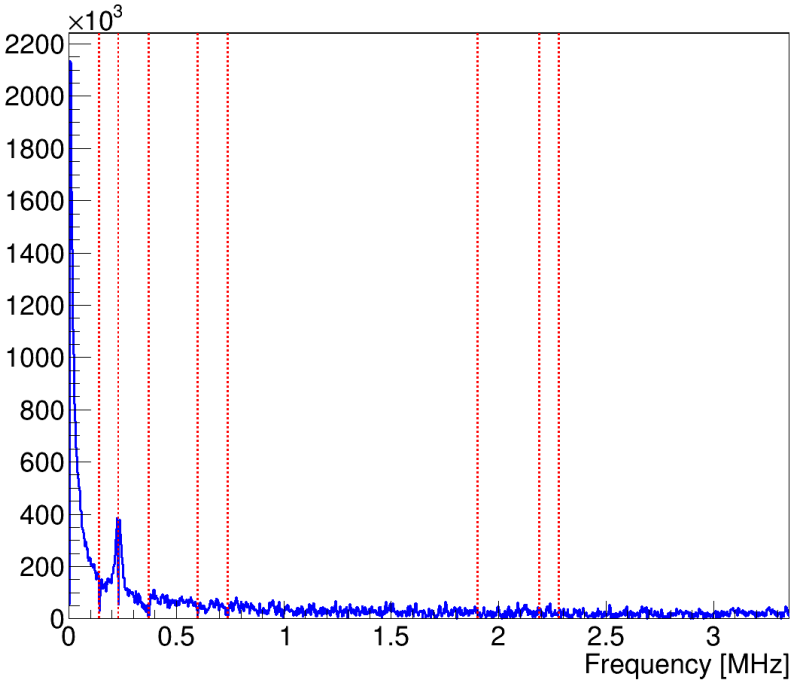

Figure 8.5: The FFT of the fit residuals with the full CBO parameterisation to the data.

the full CBO correction improves the reduced χ^2 from 18.52 to 18.28.

8.6 Slow systematic effects

At this point in the analysis, it is clear that the remaining dominant peak in the FFT of the fit residuals is the large peak at 0 MHz. These effects are known as slow effects and are most prominent at early times. Without accounting for these systematic effects it is not possible to achieve a good fit to the data. The known slow effects are from muon losses and the time-dependent efficiency of the straw tracker. In the following section, both of these contributions will be discussed.

8.6.1 Straw tracker efficiency

In the straw tracker data, the reconstruction efficiency of the positrons is much worse at early times and then decoheres with time until it stabilises late in the fill. This efficiency was determined by matching calorimeter deposits with straw tracker hits and evaluating the efficiency with which a track was matched with the cluster.

This effect is caused by a build up of space-charge after the intense beam flash at the point of injection, reducing the efficiency and it takes time for this charge to dissipate before the straw trackers perform at optimal efficiency again. The effect is much more dominant in the straw tracker Station 12 than it is in Station-18 due to Station-12 being closer to the point of injection. As the ω_a measurement is dependent on the number of reconstructed positrons, this time-dependent effect can significantly bias the measurement if it is not corrected for.

To try to resolve this effect, the first attempt was to fit the efficiency data. The model chosen was a single exponential envelope, as the detector will recover with some lifetime throughout the fill:

$$N_{\text{eff}}(t) = 1 - \varepsilon e^{-t/\tau_\varepsilon}, \tag{8.9}$$

where ε is the amplitude of the efficiency and τ_ε is the lifetime, or the time taken to recover after the beam flash. The fit to this data is shown in Figure 8.6

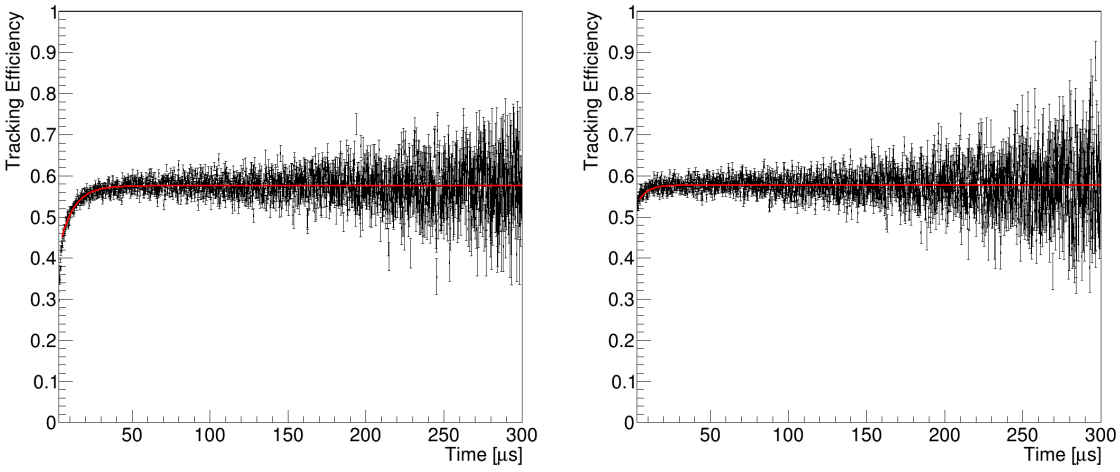

(a) (b)

Figure 8.6: Fits to the tracking efficiency data where tracks have been matched to calorimeter energy clusters for (a) Station-12 and (b) Station-18. The uncertainties are large at later time due to the reduced number of tracks and the chosen bin width.

As the efficiency data that was fitted contained only the tracks that could be matched to the calorimeter data, this means that the fitted parameters obtained would not translate directly

to the full track-based ω_a analysis. However, the parameters can be used as initial starting parameters for the full fit function and then can be allowed to float to accommodate the full tracking dataset. Incorporating this efficiency reduces the peak at 0 MHz substantially in the FFT and the reduced χ^2 is decreased from 18.23 to 1.17.

However, as the tracker efficiency is understood to be from an early time space-charge effect, it is dependent on not just the time in fill but also the momentum of the detected positron and the momentum dependence of ε was subsequently determined with the muon lifetime, and CBO lifetime fixed in the fit. The efficiency as a function of momentum is shown in Figure 8.7

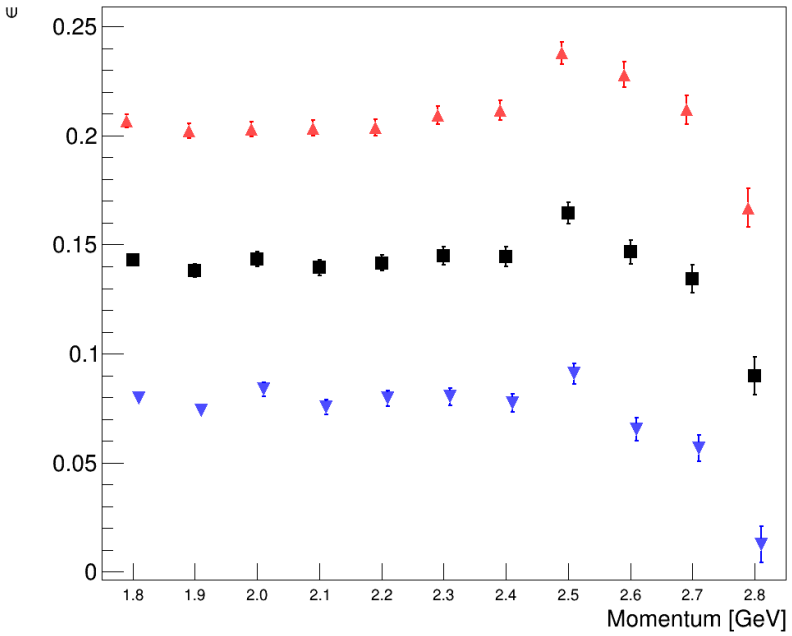

Figure 8.7: The value of the efficiency amplitude, ε, as a function of momentum. The red points show the fit in Station-12, the blue points show the fit in Station-18, and the black points are the average of the two stations.

As can be seen in Figure 8.7, the efficiency parameters are stable at lower momentum but vary significantly for momenta larger than 2.4 GeV. This is likely due to lost muons in the data, which will be discussed in Section 3.4.3. Due to this instability, a cut is applied on the data at 2.4 GeV such that subsequent fits only used tracker data in the momentum range: $1.8 < p < 2.4$ GeV.

Incorporating this momentum-dependent tracking efficiency improves the reduced χ^2 of the ω_a fit from 1.17 to 1.08 and one can see from Figure 8.8(b) that the 0 MHz peak in the FFT is reduced.

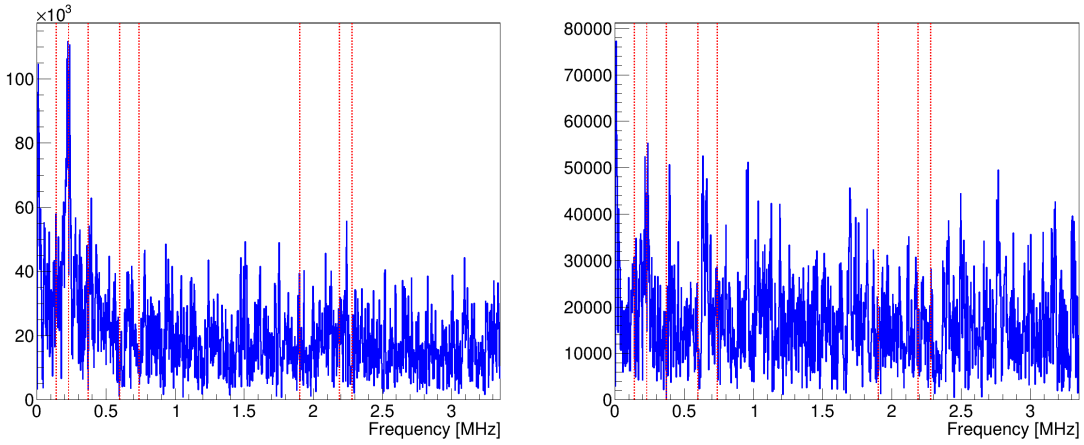

(a) (b)

Figure 8.8: Fast Fourier transforms (FFTs) of the residuals between the fitted function and the data for (a) when the tracking efficiency has no momentum dependence and (b) when it is has a momentum dependence. A clear reduction is seen in the 'slow' frequencies at 0 MHz as well as a reduction in the residual g−2 frequency.

8.6.2 Lost muons

As mentioned in Section 3.4.3, when muons collide with material within the storage ring, they lose energy and, therefore, spiral into the detectors. This effect is seen both in the calorimeters and the straw trackers and is more prominent at early times. This adds a low frequency in the FFT since the muon population is being depleted faster than the muon lifetime due to these losses. The momentum distribution of tracks for 5 time intervals is shown in Figure 8.9 where the lost muons are clearly visible as a peak at $p \sim 2700\,\text{MeV}$ for times less than $30\,\mu\text{s}$.

Based on the tracking data alone there is no way to determine whether a track is a muon or a positron and so the estimate of the lost-muon rate is taken by using the triple coincidence method from the calorimeter data (see Section 3.4.3). The time distribution of lost muons, normalised to N_0, identified by this method for Runs 2 and 3 is shown in Figure 8.10.

The lost muons are then incorporated into the fit function using the triple coincidence spectrums in Figure 8.10. As it is unknown what the efficiency of measuring a lost muon is then a correction factor, K_{loss}, is defined to account for this and is defined as

$$K_{\text{loss}} = \frac{1}{\varepsilon_\mu N_0}, \tag{8.10}$$

where ε_μ is the efficiency of detecting a lost muon. The full form of the muon loss contribution

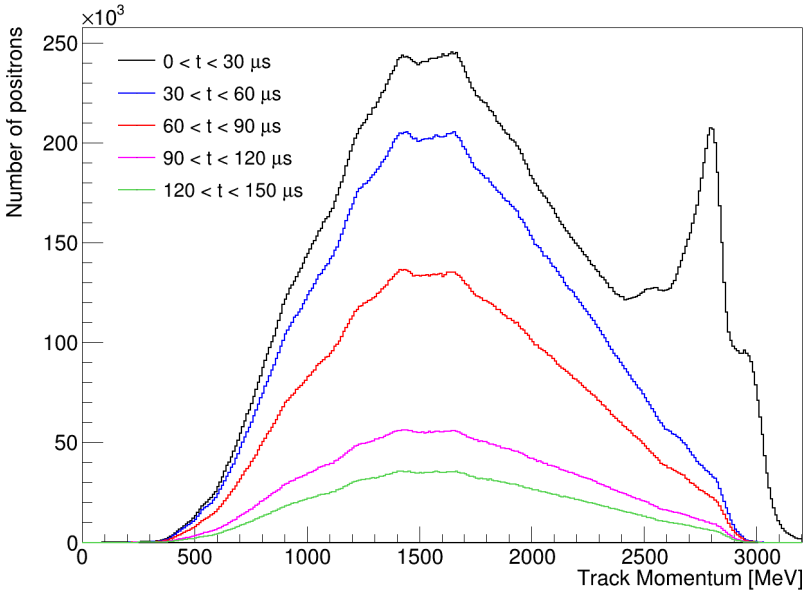

Figure 8.9: Momentum distribution of reconstructed tracks in 5 time intervals. At early times a peak from lost muons is visible at high momentum.

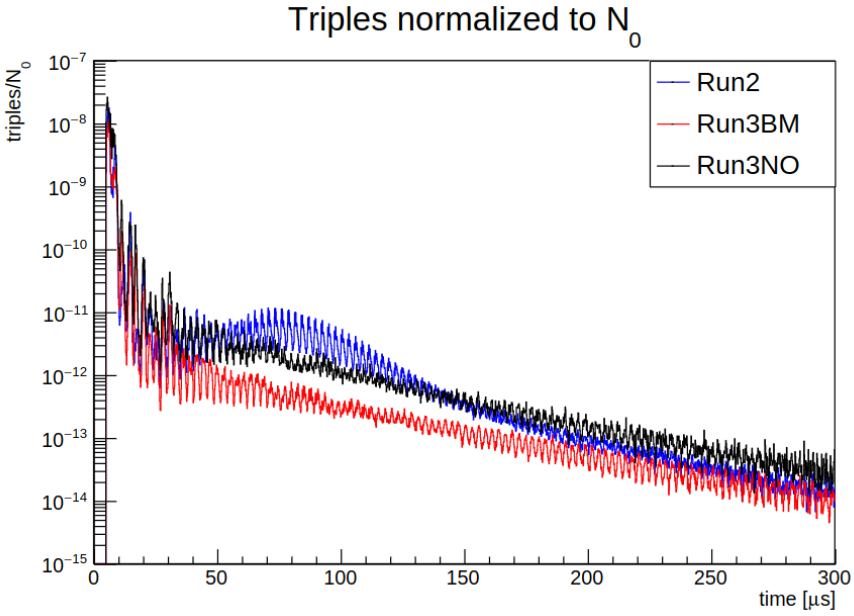

Figure 8.10: Time distribution for lost muons with a triple coincidence (present in three adjacent calorimeters) for Run-2 and Run-3.

is defined by

$$\Lambda(t) = 1 - K_{\text{loss}} \int_0^t L_T(t')e^{-t/\tau}(t'), \tag{8.11}$$

where L_T is the triple coincidence spectrum shown in Figure 8.10 and τ is the muon lifetime [69]. $N_0(t)$ is thus modified by a multiplicative $\Lambda(t)$ factor in the ω_a fits. Since the muon losses reduce $N_0(t)$ K_{loss} must be positive. A negative K_{loss} would imply that muons are being gained over time, which is impossible.

However in the calorimeter ω_a analysis, convergent fits could not always be obtained with a positive K_{loss} value [37]. Since negative values are unphysical, K_{loss}, was set to zero for Run-3a and Run-3b and 0.0011 for Run-2 and these are the values also used in the tracker ω_a analysis.

8.7 Final fit results

The final fits incorporating all the effects of the previous sections: muon lifetime, CBO, 2×CBO, tracking efficiency and muon losses have reduced χ^2 values of 1.10, 1.07 and 1.04 in Run-2, Run-3a and Run-3b respectively. A representative fitted 'wiggle' time distribution plot for a single respective random seed for Run-3a and the pulls between the fitted function and the data can be seen in Figure 8.11. The FFTs of the residuals between the data and the fit are shown in

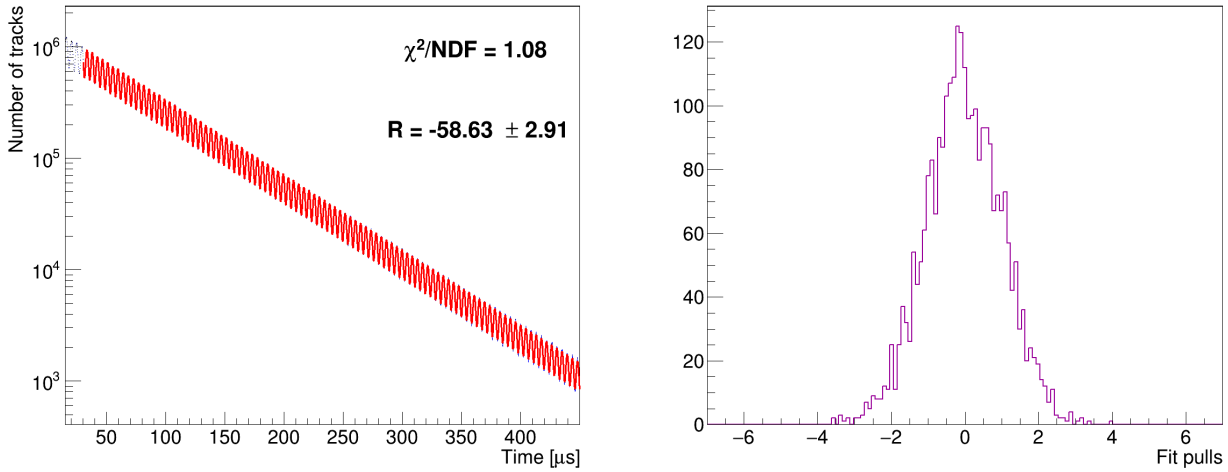

(a) (b)

Figure 8.11: A representative fit to Run-3a data for a single respective random seed where (a) shows the fit to the data and the extracted value of R and (b) shows the pulls between the fitted function and the data which are Gaussian and centred at 0.

Figure 8.12 and it is clear that the majority of the discussed effects have now been removed, as shown by the removal of the peaks at the corresponding frequencies.

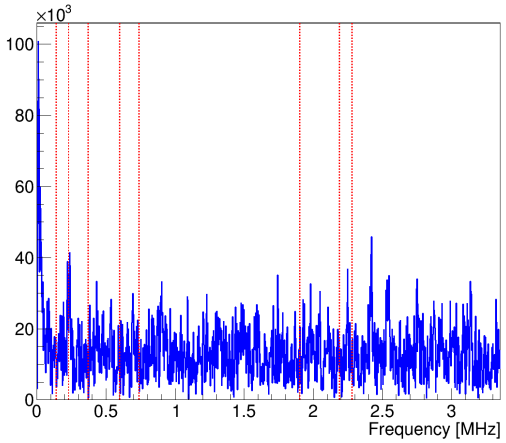

(a) Run-2

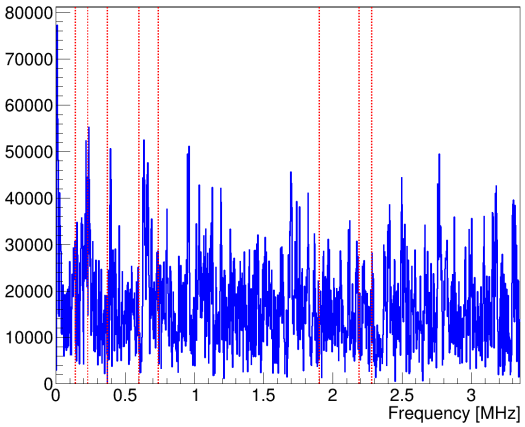

(b) Run-3a

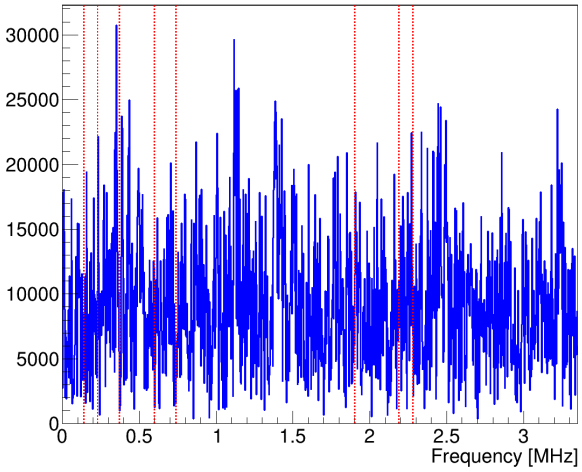

(c) Run-3b

Figure 8.12: Fast Fourier transforms (FFTs) of the residuals between the fitted function and the data for each dataset.

Fit Parameter	Definition
N_0	Number of positrons at t=0
τ	Boosted muon lifetime
A	Precession frequency asymmetry
R^*	Blinded precession frequency
ϕ	Precession frequency phase
$A_{1CBO,N}$	CBO decoherence amplitude
τ_{CBO}	CBO decoherence lifetime
ω_{CBO}	CBO decoherence frequency
$\phi_{1CBO,N}$	CBO decoherence phase
$A_{1CBO,\phi}$	A modulation from CBO phase
$\phi_{1CBO,\phi}$	ϕ modulation from CBO phase
$A_{1CBO,A}$	A modulation from CBO asymmetry
$\phi_{1CBO,A}$	ϕ modulation from CBO phase
$A_{2CBO,N}$	Amplitude from $2 \times$ CBO
$\phi_{2CBO,N}$	Phase from $2 \times$ CBO
ε	Residual reconstruction efficiency
τ_ε	Residual reconstruction efficiency lifetime
K_{loss}	Muon loss normalisation

Table 8.4: Table of fit parameters used for the Run-2/3 analysis, including descriptions of their meaning.

However, there are still residual effects at low frequencies particularly in Run-2 and Run-3a. This is due to the less than perfect modelling of the lost-muons that is not quite compensated by the momentum cut and the use of the calorimeter triple-coincidence functions. More studies will need to be performed to develop an improved method of determining the lost muon effect in the tracker data. Studies which are best performed with the full g-2 dataset that has more than 4 times the data of the Run-2/3 data analysed in this thesis. This full dataset has only recently become available.

Table 8.4 shows the naming convention for the fit parameters used in the final fitting procedure, and the final results can be seen in Table 8.5.

The final statistical uncertainty on the extracted precession frequency for each dataset can be seen in Table 8.6. The combined statistical uncertainty for the entire Run-2, Run-3 datasets is 2.16 ppm assuming a Gaussian distribution of the errors and also that the separate datasets are not correlated.

The correlation matrix of the fitted parameters for the largest dataset, Run-3a, can be seen in Figure 8.13. The correlation matrix shows that the precession frequency is largely uncorrelated with most of the fit parameters. The largest correlation is due to a correlation with the time-dependent phase, as discussed in Section 3.4.3. The next largest correlated parameters are the

Fit Parameter	Run-2	Run-3a	Run-3b
χ^2/NDF^*	1.10	1.07	1.04
N_0	$7.99 \times 10^5 \pm 6.38 \times 10^2$	$1.23 \times 10^6 \pm 2.80 \times 10^2$	$4.37 \times 10^5 \pm 1.97 \times 10^2$
τ	64.32 ± 0.01	64.37 ± 0.01	64.35 ± 0.01
A	0.2775 ± 0.0001	0.2938 ± 0.0001	0.2780 ± 0.0000
R^*[ppm]	-61.12 ± 3.85	-59.22 ± 3.10	-52.59 ± 4.86
ϕ	2.145 ± 0.001	2.143 ± 0.000	2.153 ± 0.001
$A_{1CBO,N}$	0.0161 ± 0.0003	0.0150 ± 0.0002	0.0071 ± 0.0004
τ_{CBO}	303.1 ± 16.1	284.9 ± 12.8	215.9 ± 31.5
ω_{CBO}	2.341 ± 0.000	2.330 ± 0.000	2.331 ± 0.001
$\phi_{1CBO,N}$	0.1048 ± 0.0157	6.162 ± 0.014	0.0653 ± 0.0533
$A_{1CBO,\phi}$	0.0024 ± 0.0006	0.0016 ± 0.0005	0.0028 ± 0.0010
$\phi_{1CBO,\phi}$	1.488 ± 0.271	0.527 ± 0.305	-5.314 ± 0.343
$A_{1CBO,A}$	0.0028 ± 0.0006	0.0022 ± 0.0004	0.0019 ± 0.0010
$\phi_{1CBO,A}$	0.0987 ± 0.2231	5.958 ± 0.221	-6.141 ± 0.497
$A_{2CBO,N}$	0.0002 ± 0.0001	0.0002 ± 0.0001	0.0005 ± 0.0003
$\phi_{2CBO,N}$	-2.961 ± 0.657	-3.4 ± 0.6	11.64 ± 0.47
ε	0.0258 ± 0.0008	0.0363 ± 0.0047	0.0452 ± 0.0057
τ_ε	50.09 ± 3.39	18.16 ± 1.33	21.06 ± 1.85
K_{loss}	0.0011 ± 0.00	0	0

Table 8.5: Final fit results for each dataset. The parameters marked * are taken from the average of 100 random seeds. The other parameters are taken from a single seed.

Fit Parameter	Run-2	Run-3a	Run-3b
$\sigma_{\mathrm{R,stat}}$[ppm]	3.85	3.10	4.86

Table 8.6: Statistical uncertainty on the extracted precession frequency for each dataset in Run-2 and Run-3.

CBO parameters, which is expected as the CBO effect lasts late into the muon fill and causes a significant modulation of the positron rate. The rest of the parameters have a small correlation with R.

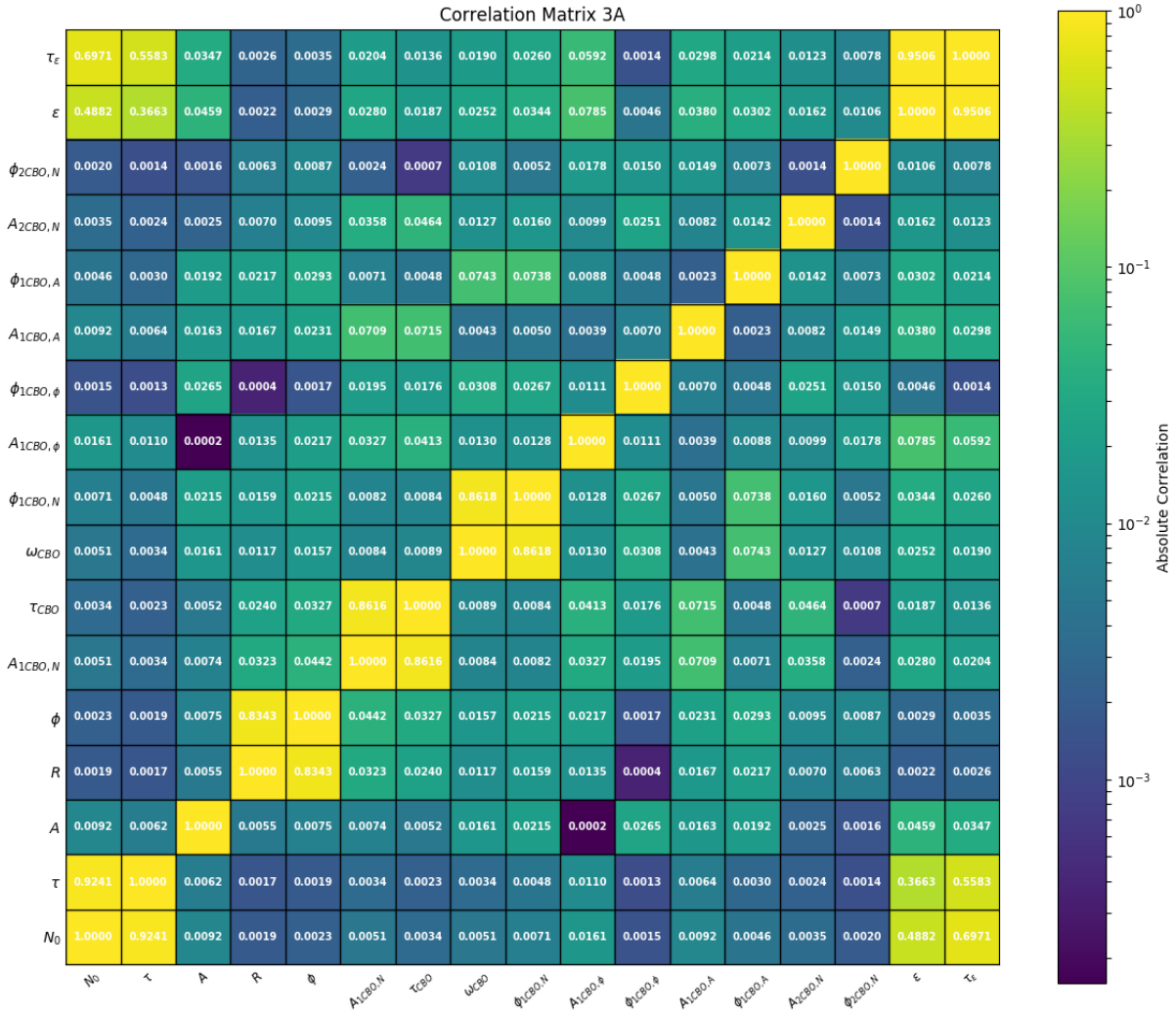

Figure 8.13: Correlation matrix of the extracted fit parameters for the largest dataset, Run-3a. The values displayed are the absolute correlation.

In the next chapter the systematic uncertainties and particularly the impact of the effects arising early in the fill: muon losses, pileup and tracker efficiency will be evaluated.

Chapter 9

Evaluation of the systematic effects in the tracker ω_a analysis

This chapter discusses and evaluates the sources of systematic uncertainties in the Run-2/3 measurement of ω_a using the straw tracking detectors. The systematic uncertainties are estimated for the straw tracker pileup, lost muons, the efficiency of the straw trackers, and the modelling of the CBO decay envelope.

The total systematic uncertainty is smaller than the statistical uncertainty, but there are significant effects that need to be better understood and mitigated before the full g-2 dataset is analysed. The ongoing work to achieve this is also briefly described.

9.1 Randomisation

As mentioned in Section 8.4, the effects of the vertical waist and fast rotation are removed from the fit by randomising the time binning. This is done for a choice of 100 random seeds resulting in 100 R values. The systematic uncertainty from this procedure is taken from the error on the mean of a Gaussian fit to the 100 R values. An example for Run-3a is shown in Figure 9.1 and the values are listed in Table 9.1.

Value	Run-2	Run-3a	Run-3b	Combined
ΔR[ppm]	0.09	0.09	0.19	0.06

Table 9.1: Uncertainties in the extracted precession frequency, R, due to the randomisation procedure.

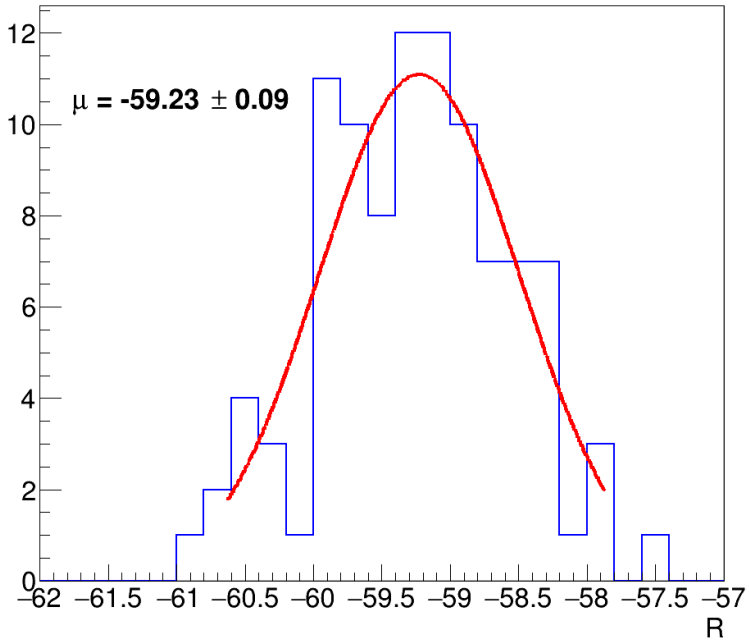

Figure 9.1: Distribution (for the Run-3a dataset) of the extracted frequency, R, from the randomisation procedure that removes the vertical waist and fast-rotation.

9.2 Pileup in the tracker

As described in Section 7.2, the pileup in the straw tracker data was determined to be $5.25 \pm 0.33\%$ (a 0.063 fractional uncertainty) where the uncertainty accounts for the difference between the predictions of the two algorithms. In addition, for each of the two algorithms, the determination of the algorithm parameters has an uncertainty arising from the statistics of the data in the fit determining these parameters. The model dependency is far more significant, but the impact of both on the R-fit is evaluated by adding a "pileup multiplier", K_{PU}, of the form

$$\Delta\rho_{pu}(t) = \frac{K_{PU}(\rho_3(t) - \rho_2(t) - \rho_1(t))}{2}, \tag{9.1}$$

where, K_{PU} is varied between 1.00 ± 0.07 and R is re-evaluated. The change in R in Run-3a for this variation can be seen in Figure 9.2 and the systematic uncertainty from the tracker pileup in Table 9.2.

-	Run-2	Run-3a	Run-3b	Combined
ΔR [ppm]	0.17	0.17	0.17	0.17

Table 9.2: Systematic uncertainty from the tracker pileup.

The effect of the pileup is much larger in Station-12 than Station-18 (see Figure 8.6). The

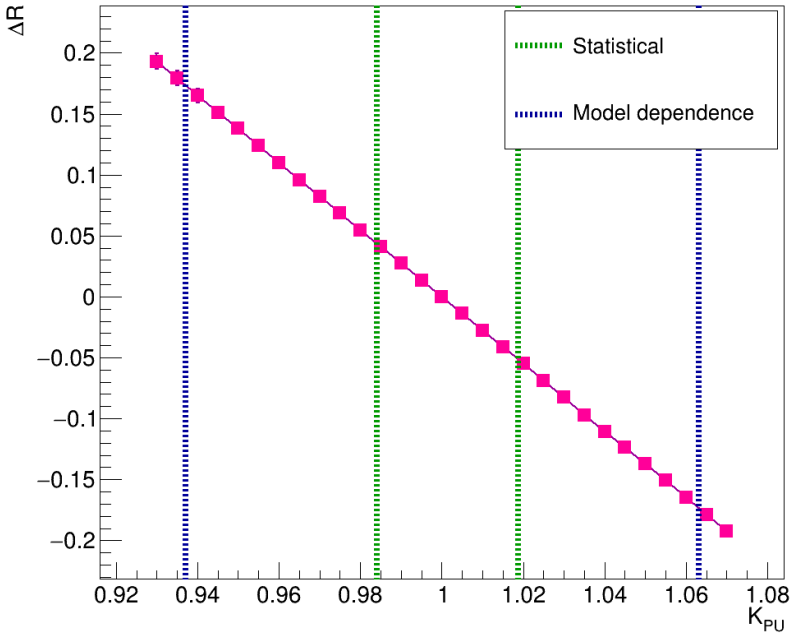

Figure 9.2: Change in R in ppm versus the pileup multiplier for Run-3a. The change in R from the algorithm dependence and the statistics determining the parameters of either algorithm are shown.

systematic uncertainty from Station-12 is used as the overall systematic uncertainty. ± 0.02 of the uncertainty arises from the statistics determining the algorithm parameters but is negligible compared to the systematic uncertainty arising from the algorithm choice. Since the uncertainty from the choice of algorithm is common across all datasets, it is assumed to be 100% correlated across the three datasets in determining the combined uncertainty.

9.3 Straw tracker efficiency

The correction for the reduction in straw tracker efficiency at early times is a time-dependent exponential with an amplitude with a momentum dependence (see Section 8.6.1)

$$f_A(t) = 1 - \varepsilon(p)e^{-t/\tau_\varepsilon}., \tag{9.2}$$

where τ and ε are determined from fitting calorimeter-matched tracking data and the fit covariance matrix is used to generate pairs of τ and ε values. This fit and its variance from sampling the fit covariance matrix are shown in Figure 9.3 for Station-12 where the effect is largest and thus sets the most conservative systematic uncertainty.

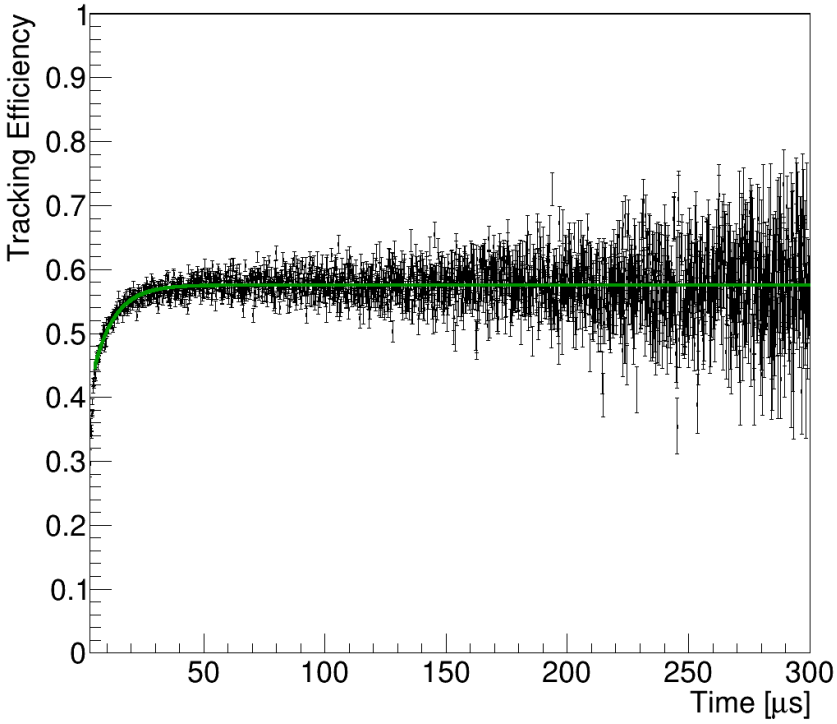

Figure 9.3: The fit to the calorimeter-matched tracking data determining τ and ε and the range of efficiencies used to determine the systematic uncertainty for Station-12 data.

The generated values of τ and ε from sampling the covariance matrix were then fixed in the R-fit to each dataset and the extracted values of R were fitted with a Gaussian and the systematic uncertainty is taken as the standard deviation of this Gaussian as shown in Figure 9.4.

The uncertainties are shown in Table 9.3. The range in τ and ε values for each dataset are driven by the statistics of the fit to the efficiency data and thus the uncertainties are considered not to be correlated between the datasets.

	Run-2	Run-3a	Run-3b	Combined
ΔR[ppm]	0.05	0.04	0.04	0.03

Table 9.3: Shifts in the extracted precession frequency, R, from the variation in tracking efficiency for each dataset and the combined value across all datasets.

9.4 CBO modelling

The effect of the CBO lasts for $\sim 250\,\mu$s into the fit period and thus has a significant impact on R. The default CBO amplitude is simply a decaying exponential of the form: $Ae^{-t/\tau}$ (see Equation 8.5). However, in the calorimeter analysis, owing to its higher statistics, it was

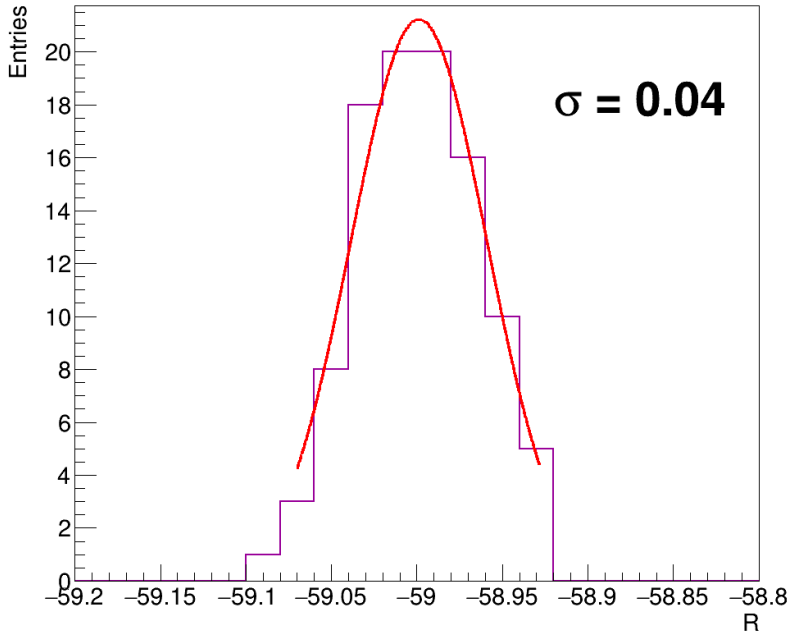

Figure 9.4: Distribution of the extracted frequency, R, from the efficiency covariance matrix sampling for the Run-3a dataset for Station-12.

possible to show that two other alternate forms provided a reasonable description of the data and these two forms have been used in this analysis to estimate the systematic uncertainty due to CBO modelling. The first model, Model-A, is the same as the nominal model with an additional constant offset in the amplitude i.e.

$$f_{\mathrm{A,CBO}}(t) = Ae^{-t/\tau_{\mathrm{CBO}}} + C \tag{9.3}$$

whereas the second, Model-B, is a steeply falling quadratic function i.e.

$$f_{\mathrm{A,CBO}}(t) = A\frac{1}{1+\alpha t^2} + C \tag{9.4}$$

which has a new parameter α, and again, a constant offset.

The result of the fits using these functional forms to the Run-3a data is shown in Figure 9.5.

The shift in R from the two alternative forms for the CBO amplitude are shown in Table 9.4 and range from 0.2–0.8 ppm. The largest shift in R across both models is taken as the systematic for a given dataset and they are combined across datasets assuming the uncertainties are correlated since the fits that determine the exact form of the CBO envelopes for each data are driven by the statistics of the dataset.

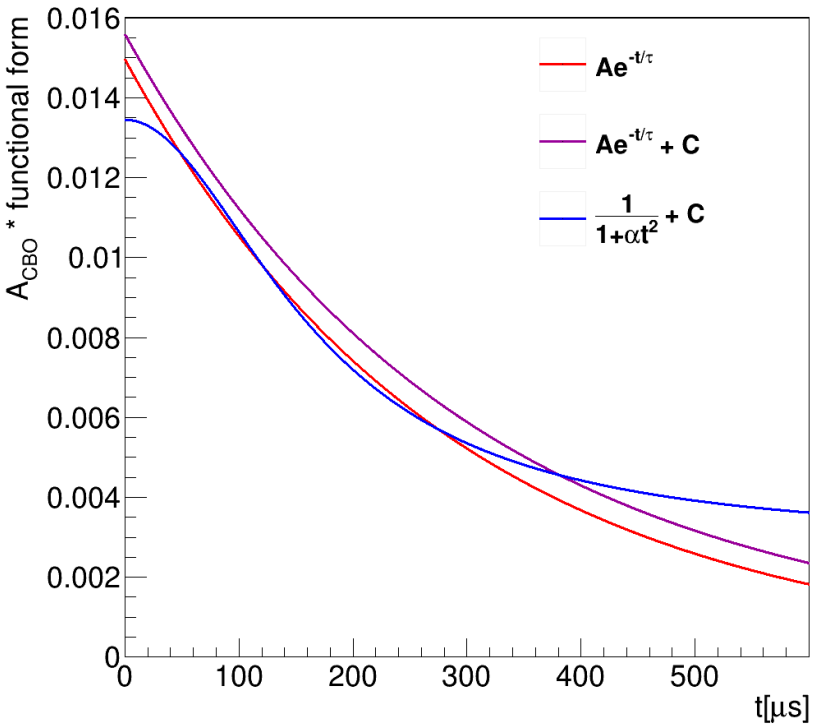

Figure 9.5: The CBO amplitude from the nominal model and two alternative models from a fit to the Run-3a data.

Envelope	-	Run-2	Run-3a	Run-3b	Combined
Model A, B	ΔR[ppm]	$0.42, 0.20$	$0.20, 0.54$	$0.83, 0.26$	
Systematic	ΔR[ppm]	0.42	0.54	0.83	0.31

Table 9.4: Shifts in the extracted precession frequency, R, for each CBO envelope and dataset.

9.5 Lost muon modelling

As described in Section 8.7, there remain small residual unaccounted for effects leading to an imperfect description of the data at low frequencies in the FFT and at early times in the ω_a fit. This is believed to be a mismodeling in the lost muons where for example non-physical values of the K_{loss} parameter (Equation 8.10) are obtained in the calorimeter fits to the Run-3 data. This is further supported by an analysis of the tracker data when the start-time of the fit is offset by multiples of the cyclotron frequency from the chosen start-time of 30.2876 μs. The chosen form for the fit is the nine-parameter fit as described in Section 8.5.1 with a non-momentum dependent tracking efficiency. The change in the fitted value of R as the start-time of the fit is increased (and hence the statistics decrease) are shown in Figure 9.6 for both the Run-2 and Run-3 datasets. The green and purple bands show the allowed 1 σ and 2 σ deviations based on the fact that subsequent fits beyond 30.2876 μs are correlated with those at earlier time since they contain a subset of the same data and thus the allowed deviation increases with start-time. The blue line shows the uncorrelated 1 σ uncertainty of each fit.

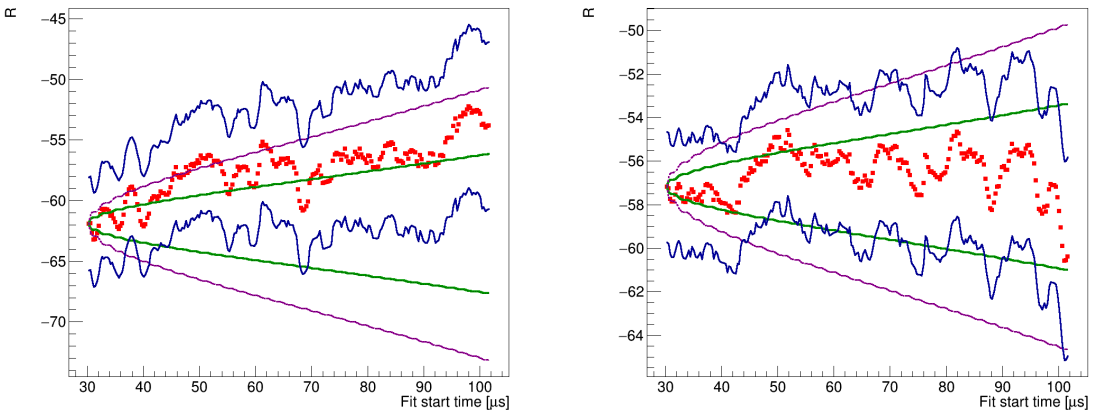

Figure 9.6: The fitted value of R for the (a) Run-2 and (b) Run-3 datasets as the start-time of the fit is increased. The blue line represents the 1 σ uncertainty on each point, and the green and purple lines represent the accepted 1 σ and 2 σ variations from the initial value.

As can be seen from Figure 9.6, the Run-3 data is described well with more than 68% of the points within the expected 1 σ deviation. For Run-2 the deviations are larger, particularly for fits starting in the $40 < t < 100\,\mu$s region. This is due to an enhancement in the lost-muon rate for a subset of the Run-2 data. Figure 9.7 shows the lost-muon spectrum identified from the triple-coincidences (see Section 3.4.3) in the calorimeter where there is a significant enhancement in the rate in the $40 < t < 100\,\mu$s region for a subset of the Run-2 data. This lost muon enhancement has been tracked to a $\mathcal{O}(1\,\text{mm})$ radial shift in the average beam position

which was present for a subset of the Run-2 data. The effect is more acute in the tracking data compared to the calorimeter data since there are only two trackers and owing to its azimuthal location Station-12 is more sensitive to muon-losses.

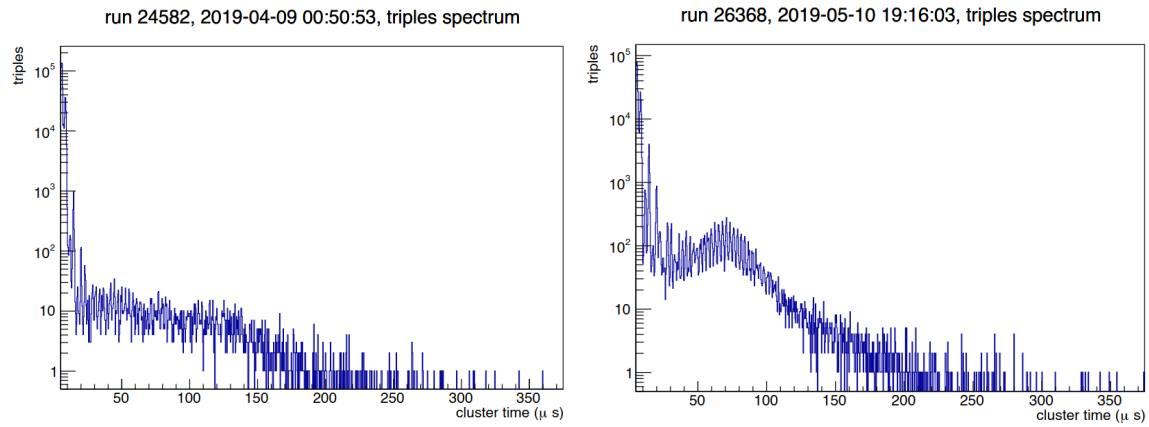

(a) (b)

Figure 9.7: The triple-coincidence, lost-muon, spectrum in two different runs in Run-2 highlighting the appearance of a 'muon bump' that biases the ω_a analysis.

The larger prevalence of lost muons in Station-12 and that they are not perfectly modelled, leads to poorer fits in Station-12 versus Station-18. This is highlighted in the high statistics Run-3 data where it is possible to do the start-time scans separately for each station. In Figure 9.8 it's clear that the majority of points in Station-12 lie outside the 1σ deviation with a small number extending beyond $2\,\sigma$. The data in Station-18 is better described, albeit not perfectly. This mismodeling is largely constrained to the $t < 100\,\mu$s region. This is demonstrated when we vary the stop-time of the fit where instabilities are present, as expected at earlier times, but which stabilise when the later-time data is included.

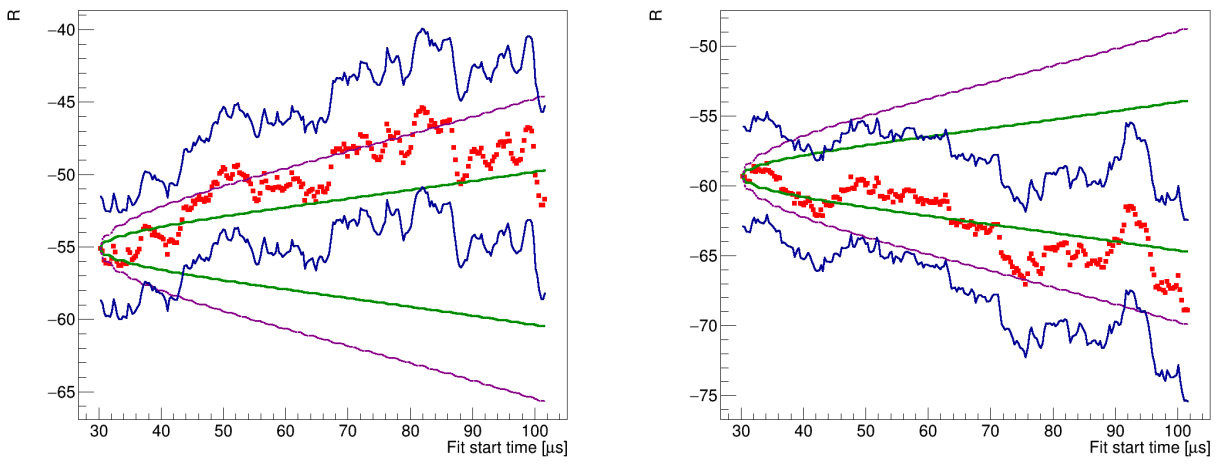

Figure 9.8: The fitted value of R in Run-3 for the (a) Station-12 and (b) Station-18 tracker data as the start-time of the fit is increased.

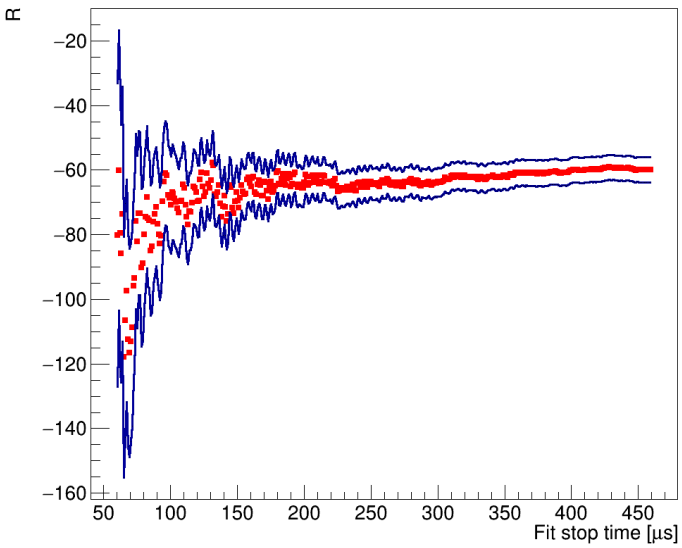

Figure 9.9: The fitted value of R in Run-2 when the stop-time of the fit is changed from 50 μs to 450 μs.

A systematic uncertainty is assigned to the Run-2 dataset for the effect of the enhanced muon losses in the $40 < t < 100\,\mu$s region, which aren't explicitly modelled, although on average the muon-loss rate is. The most conservative estimate can be obtained using Equation 3.4.3 that defines the shift in ω_a arising from lost muons whose phase is different from the average, as is the case here since the muons losses are enhanced in a subset of the time window. The shift is momentum-dependent but we take the shift from the lowest momentum value, which gives the largest shift, to be conservative. This results in a systematic uncertainty of 0.15 ppm for the Run-2 dataset.

9.6 Final systematic uncertainty

The systematic uncertainties evaluated in this chapter are listed in Table 9.5.

Uncertainty	Run-2	Run-3a	Run-3b	Combined
Statistical	3.85	3.10	4.86	2.16
Randomisation	0.09	0.09	0.19	0.06
Pileup	0.17	0.17	0.17	0.17
Efficiency	0.05	0.04	0.04	0.03
CBO envelope	0.42	0.54	0.83	0.31
Lost muon	0.15			0.05
Total systematic	0.49	0.57	0.87	0.36

Table 9.5: Overview of the uncertainties for the ω_a analysis.

The systematic uncertainties have been combined under the assumption that they are uncorrelated. In reality, there is some correlation, for example, the tracker pileup and tracker efficiency are both effects that dominate at early times and are both independently determined from fits to similar data. In the subsequent Run-4/5/6 higher statistics data-samples it should be possible to do a more sophisticated evaluation of the correlations.

The total systematic uncertainty of 0.36 ppm is significantly below the statistical uncertainty of 2.16 ppm. Additionally, a large fraction of the systematic uncertainty is statistics-driven since the model uncertainties are determined from fits to data whose uncertainties depend on the statistics of the fitted sample. The exception is presently the determination of the tracker pileup where further work is required to determine the most appropriate model which again will be more tractable using the larger Run-4/5/6 datasets.

With the addition of the Run-4/5/6 data, the statistical uncertainty in the tracker ω_a analysis is expected to be 1.05 ppm and the total uncertainty on ω_a will still be dominated by the statistical uncertainty. Recently work has begun to substantially improve the fraction of the tracks that are successfully reconstructed by scaling the uncertainty on the drift time calculation as a function of the time since the start of the fill [70]. As highlighted in the next Chapter it is then hoped that a tracked-based determination of ω_a should be able to match the precision of the BNL or Run-1 analyses using calorimeter data.

9.7 Outlook

To match the precision of the BNL (or Run-1 analyses) that used calorimeter data requires a precision of 0.54 ppm. Or conversely to demonstrate an agreement with the BNL calorimeter-based determination of a_μ at better than 5% confidence-level requires a precision of 1.2 ppm. This will be possible with the addition of the Run-4/5/6 datasets and improvements in the fraction of tracks that are successfully reconstructed.

Figure 9.10 shows the total number of positrons, before data quality and analysis requirements, recorded by the Fermilab Muon g-2 experiment as a multiple of the BNL raw dataset size (8.6×10^9 e^+) for Run-1 to Run-6, showing that approximately a fourfold increase in statistics is expected when the full dataset is analysed compared to the analyses to date.

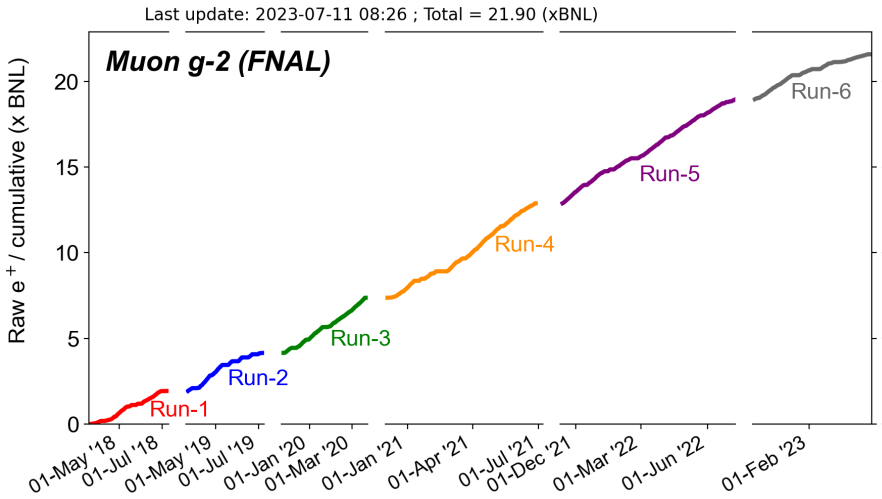

Figure 9.10: Total number of positrons, before data quality and analysis requirements, recorded by the Fermilab Muon g-2 experiment as a multiple of the BNL raw dataset size.

Recent improvements [71] in the straw tracker reconstruction algorithms, particularly at early times in the fill have resulted in a factor of 2.86 more reconstructed tracks than was the case with the software used to reconstruct the Run-2/3 data used in this thesis. Together the increase in statistics provided by the Run-4/5/6 data and the tracking improvements will allow a statistical precision of 0.6 ppm to be achieved. It is hoped that ultimately a factor of four improvement in tracking efficiency can be achieved which should enable the precision of the BNL determination to be matched. This is shown in Figure 9.11.

The Muon g-2 experiment has now finished data taking and the analysis of the Run-4/5/6 data is underway. The experiment has already surpassed the systematic uncertainty goal defined in the TDR in the publication of the Run-2/3 data and further improvements in the systematic uncertainty are expected. The statistics goal for the experiment was achieved on February

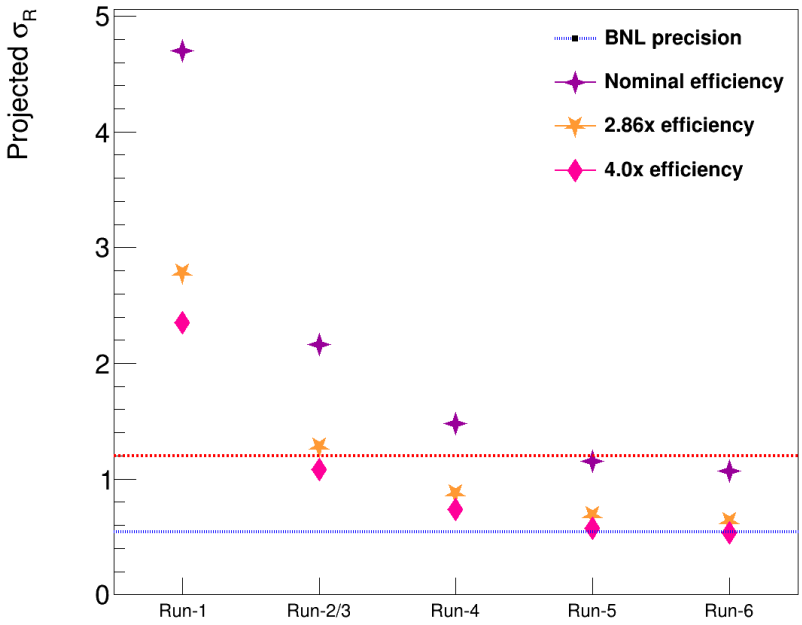

Figure 9.11: A prediction of the final statistical uncertainty of the straw tracker independent ω_a analysis as more datasets are added to the analysis, based on the Run-2/3 result from this thesis. The blue line is the BNL precision and the red-line 2.3 times that i.e. the precision required to confirm the BNL result at more than a 5% confidence level.

27, 2023, reaching 21 times the statistics of the BNL experiment and the TDR goal of a statistical uncertainty of 100 ppb is thus also expected to be surpassed. The significance of the final Fermilab Muon g-2 publication with an expected uncertainty of less than 140 ppb in the context of new physics interpretations now largely rests with the theoretical community. However, there is an important experimental measurement that can be made to independently predict the SM value that to date has not been exploited.

This is the `MUonE` [72] experiment that will measure the running coupling of the fine structure constant via electron-muon elastic scattering which will allow a direct determination of the hadronic vacuum polarisation contribution to a_μ. This will be crucial in elucidating the current tensions in the SM prediction of a_μ between the dispersive data-driven method, the lattice QCD method and the latest `CMD-III` results.

Chapter 10

Conclusions

This thesis describes a detailed study of the data taken by the Fermilab Muon g-2 straw tracking detectors. Two new methodologies have been developed: the first is a method to better determine the track arrival time (t_0) and the second is a method to quantify the level of pileup in the tracking detectors. The new t_0 algorithm, which incorporates angular information, improves the resolution on the determination of the t_0 by a factor of two and results in 19% more tracks being successfully reconstructed compared with the previous method.

The data from the trackers is used to determine the beam profile that weights the magnetic field in the determination of a_μ and in determining several of the systematic uncertainties in the calorimeter-based ω_a analysis e.g. that due to the radial position and vertical oscillation of the beam. A detailed study of the impact of the internal alignment of the tracker, the t_0 and pileup on the determination of the beam position was undertaken and propagated to determine an uncertainty in the ω_a determination. These uncertainties were used in the recent 2023 publication [14] in the calculation of the magnetic field correction.

This thesis also presented the first (blinded) determination of ω_a using just tracks from the straw tracking detectors as opposed to calorimeter energy deposits. This analysis has sources of systematic uncertainty that are different from the much higher-statistics calorimeter analysis and will ultimately allow an important cross check of the calorimeter analysis. This analysis was undertaken using the Run-2/3 dataset which represents approximately 25% of the final Muon g-2 dataset. A total uncertainty of 2.19 ppm on ω_a was obtained which is dominated by the statistical uncertainty of 2.16 ppm.

References

[1] G. W. Bennett *et al.*, "Final report of the E821 muon anomalous magnetic moment measurement at BNL", Phys. Rev. D 73 7 (2006).

[2] B. Abi *et al.*, "Measurement of the positive muon anomalous magnetic moment to 0.46 ppm", Phys. Rev. Lett. 126 14 (2021).

[3] T. Aoyama *et al.*, "The anomalous magnetic moment of the muon in the Standard Model", Phys. Rept., 887 1 (2020).

[4] P.A.M. Dirac, "The quantum theory of the electron i", Proceedings of the Royal Society A, 117(778) 610 (1928).

[5] P.A.M. Dirac, "The quantum theory of the electron ii", Proceedings of the Royal Society, 118(779) 351 (1928).

[6] J. Schwinger, "Quantum electrodynamics. iii. the electromagnetic properties of the electronradiative corrections to scattering", Phys. Rev. 76 790 (1949).

[7] J. Grange *et al.* [Muon g−2 Collaboration], "Muon g−2 technical design report", Muon g−2 FNAL, Batavia, IL, 2015, arXiv: 1501.06858 (2015).

[8] M.E. Peskin, and D.V. Schroeder, "An introduction to quantum field theory", Westview, (1995).

[9] P. Kusch and H. M. Foley, "The Magnetic Moment of the Electron", Phys. Rev. 74 250 (1948).

[10] R.L. Garwin *et al.*, "Accurate Determination of the μ^+ Magnetic Moment", Phys. Rev. 118 271 (1960).

[11] G. Charpak *et al.*, "A new measurement of the anomalous magnetic moment of the muon", Phys. Lett. 1.1 16 (1962).

[12] J. Bailey *et al.*, "Precision measurement of the anomalous magnetic moment of the muon", Phys. Lett. B 28.4 287 (1968).

[13] J. Bailey *et al.*, "Final report on the CERN muon storage ring including the anomalous magnetic moment and the electric dipole moment of the muon, and a direct test of relativistic time dilation", Nuc. Phys. B 150 1 (1979).

[14] D.P. Aguillard *et al.*, (The Muon g-2 Collaboration), "Measurement of the Positive Muon Anomalous Magnetic Moment to 0.20 ppm", Phys. Rev. Lett. 131 161 (2023).

[15] T. Aoyama *et al.*, "Complete Tenth-Order QED Contribution to the Muon g−2", Phys. Rev. Lett 109 11 (2012).

[16] C. Gnendiger, D. Stoeckinger, and H. Stoeckinger-Kim. "The electroweak contributions to $(g-2)\mu$ after the Higgs boson mass measurement", Phys. Rev. D 88 05 (2013).

[17] C. Bouchiat and L. Michel, "The π-π meson scattering resonance and the anomalous magnetic moment of the μ meson", J. Phys. Radium 22 121 (1961).

[18] F. Ambrosino *et al.* (KLOE), "Measurement of $\sigma\left(e^+e^- \to \pi^+\pi^-\gamma(\gamma)\right)$ and the dipion contribution to the muon anomaly with the KLOE detector", Phys. Lett B 670 285 (2009).

[19] B. Aubert *et al.* [BaBar Collaboration], "Precise Measurement of the $e^+e^- \to \pi^+\pi^-(\gamma)$ Cross Section with the Initial State Radiation Method at BABAR", Phys. Rev. Lett 103 231 (2009).

[20] Sz. Borsanyi, *et al.*, "Leading hadronic contribution to the muon magnetic moment from lattice QCD", Nature, 593 51 (2021).

[21] G. Colangelo, M. Davier, A. X. El-Khadra, *et al.* "Prospects for precise predictions of a_μ in the standard model", arXiv:2203.15810 (2022).

[22] J. Prades, E. de Rafael, and A. Vainshtein, "The Hadronic Light-by-Light Scattering Contribution to the Muon and Electron Anomalous Magnetic Moments", Adv. Ser. Direct. High Energy Phys. 20 303 (2009).

[23] A. Gérardin, H. B. Meyer and A. Nyffeler, "Lattice calculation of the pion transition form factor $\pi^0 \to \gamma^*\gamma^*$", Phys. Rev. D 94 074 (2016).

[24] T. Aoyama, T. Kinoshita, and M. Nio, "Revised and improved value of the qed tenth-order electron anomalous magnetic moment", Phys. Rev. D 97 03 (2018).

[25] P. Athron, C. Balázs, D. H. J. Jacob, W. Kotlarski, D. Stöckinger, and H. Stöckinger-Kim, "New physics explanations of a_μ in light of the FNAL muon g 2 measurement", JHEP, 09 (2021).

[26] J. Abdallah *et al.*, "Study of tau-pair production in photon-photon collisions at LEP and limits on the anomalous electromagnetic moments of the tau lepton", Eur. Phys. J. C 35 (2004).

[27] S. Eidelman and M. Passera, "Theory of the τ Lepton Anomalous Magnetic Moment", Mod Phys Lett A 22 (2007).

[28] P. Athron, C. Balázs, D. H. J. Jacob *et al.*, "New physics explanations of a_μ in light of the FNAL muon g - 2 measurement", J. High Energ. Phys. 2021 80 (2021).

[29] J. Jackson, "Classical Electrodynamics", Wiley Indiana, (2011).

[30] X. Fan *et al.*, "Measurement of the Electron Magnetic Moment", Phys. Rev. Lett. 130 7 (2023).

[31] P.J. Mohr, B.N. Taylor, and D.B. Newell, "CODATA Recommended Values of the Fundamental Physical Constants: 2010", Rev. Mod. Phys. 84 1527 (2012).

[32] W. Liu *et al.*, "High precision measurements of the ground state hyperfine structure interval of muonium and of the muon magnetic moment", Phys. Rev. Lett. 82 711 (1999).

[33] G.W. Bennett *et al*, "Statistical equations and methods applied to the precision muon (g−2) experiment at BNL", Nucl. Instr. Meth. A 579 1096 (2007).

[34] T. Albahri *et al.*, "Magnetic-field measurement and analysis for the Muon g-2 experiment at Fermilab", Phys. Rev. A 103 4 (2021).

[35] J. George, "The new Muon g2 experiment at Fermilab", Muon g−2 internal note, DocDB 12212 (2018).

[36] T. Albahri *et al.*, "Beam dynamics corrections to the Run-1 measurement of the muon anomalous magnetic moment at Fermilab", Phys. Rev. Accel. Beams, 24 4 (2021).

[37] H. Binney, "Precession frequency analysis for Run-2 and Run-3 of the Muon $g-2$ experiment", PhD thesis, University of Washington, Seattle, WA (2022).

[38] C. Claessens *et al.*, "The Minimally Intrusive Scintillating Fiber Detector (MiniSciFi)", Muon g−2 internal note, DocDB 26632-v1 (2022).

[39] S. Foster, "Measurement of the muon anomalous precession frequency in Runs 2 & 3 of the Muon g−2 experiment at Fermilab", PhD thesis, Boston University, Boston, MA, (2023).

[40] BNL AGS E-821 Collaboration, "BNL E-821 technical design report", Muon g−2 internal note, DocDB 125-v1 (1995).

[41] D. Stratakis *et al.*, "Accelerator performance analysis of the Fermilab Muon Campus", Phys. Rev. Accel. Beams 20 11 (2017).

[42] N. B. Kinnaird, "Muon spin precession frequency extraction and decay positron track fitting in Run 1 of the Fermilab Muon g−2 experiment", PhD thesis, Boston University, Boston, MA, (2020).

[43] B. MacCoy, "IBMS Manual", Muon g−2 internal note, DocDB 59221 (2020).

[44] K.S. Khaw *et al.*, "Performance of the Muon g 2 calorimeter and readout systems measured with test beam data", Nucl. Instr. Meth. A 945 162 (2019).

[45] J. Hempstead, "Overview of the g2 experiment", Muon g−2 internal note, DocDB 18289 (2019).

[46] T. Walton, "Muon g−2 track finding reconstruction", Muon g−2 internal note, DocDB 19303-v1 (2019).

[47] G. Lukicov, "Alignment of the straw tracking detectors for the Fermilab Muon g−2 experiment and a new search for a muon electric dipole moment", PhD thesis, University College London, London, UK, (2020).

[48] T.S. Stuttard, "The development, testing and characterisation of a straw tracking detector and readout system for the Fermilab muon g−2 experiment", PhD thesis, University College London, London, UK, (2018).

[49] G. Hesketh, "R vs. t calibration", Muon g−2 internal note, DocDB 12227 (2018).

[50] V. Innocente, M. Maire and E. Nagy, "GEANE: Average Tracking and Error Propagation Package", CERN Program Library W5013-E (1991).

[51] S. Agostinelli *et al.*, "GEANT4 - a simulation toolkit", Nucl. Instr. Meth. A 506 250 (2003).

[52] N. Kinnaird, "Geane Track Fitting", Muon g−2 internal note, DocDB 8102 (2017).

[53] N. Kinnaird, "Left/Right - What we do/have at the moment", Muon g−2 internal note, DocDB 12017 (2018).

[54] S. Charity, "Beam profile measurements using the straw tracking detectors at the Fermilab muon g–2 experiment, and a study of their sensitivity to a muon electric dipole moment", PhD thesis. University of Liverpool, Liverpool, UK (2018).

[55] J. Mott, "Track Quality Cuts", Muon g−2 internal note, DocDB 16282 (2019).

[56] J. Mott, "Track Quality Cuts: Second Edition", Muon g−2 internal note, DocDB 16420 (2019).

[57] V. Blobel, "Linear least squares fits with a large number of parameters", `http://www.desy.de/blobel/Mptwo.pdf` (2007).

[58] J. Price, "Left right doublets", Muon g−2 internal note, DocDB 6947-v3 (2017).

[59] D. Sweigart, "A Measurement of the Anomalous Precession Frequency of the Positive Muon", PhD thesis, Cornell University, Ithaca, NY (2020).

[60] J. Price, "Tracker pileup", Muon g−2 internal note, DocDB 23131-v1 (2020).

[61] S. Foster, "Empirical pileup correction method", Muon g−2 internal note, DocDB 25130 (2021).

[62] R. Brun *et al.*, "root-project/root: v6.18/02. Version v6-18-02" (2019).

[63] F. James, "MINUIT Function Minimization and Error Analysis: Reference Manual Version 94.1", CERN-D-506 (1994).

[64] N. Kinnaird, "E989 Note 214: Handling the VW in the Ratio Method", Muon g−2 internal note, DocDB 19466 (2019).

[65] H. Binney, "UW ω_a update: 1.9 MHz oscillation fitting", Muon g−2 internal note, DocDB 26115 (2021).

[66] O. Kim, "Randomization kernel optimization", Muon g−2 internal note, DocDB 28169 (2022).

[67] R. Carey, "CERN-Style Fast Rotation Analysis: Run 2 and 3 Results", Muon g−2 internal note, DocDB 28144 (2022).

[68] A. Edmonds, "Attempting to Fit ω_a without randomizing FR", Muon g−2 internal note, DocDB 27241 (2022).

[69] J. Crnkovic. et al, "Lost Muon Study for the Muon g−2 Experiment at Fermilab", Proceedings, 8th International Particle Accelerator Conference (IPAC 2017): Copenhagen, Denmark, 2017, WEPIK119.

[70] L. Bailey, "Tracking with maximum efficiency and new quality cuts", Muon g−2 internal note, DocDB 28555-v1 (2023).

[71] L. Bailey, "tracking improvements and impact on the EDM", Muon g−2 internal note, DocDB 29320-v1 (2023).

[72] G. Abbiendi *et al.*, "Measuring the leading hadronic contribution to the muon g−2 via μe scattering", Eur. Phys. J. C 77 3 (2017).